Microstructure and Properties of Semi-Solid Al Alloy 7075 after Heat Treatment

Narissara Mahathaninwong

A Thesis Submitted in Partial Fulfillment of the Requirements for the Degree of

Doctor of Engineering in Materials Engineering

Prince of Songkla University

2012

Thesis Title Microstructure and Properties of Semi-Solid Al Alloy 7075 after Heat Treatment

Author Mrs.Narissara Mahathaninwong

Major Program Materials Engineering

Major Advisor:	**Examining committee:**
.....	.....Chairperson
(Assoc. Prof. Dr.Sirikul Wisutmethangoon)	(Assoc. Prof. Dr.Chaowalit Limmaneevichitr)
	.....
Co-Advisor:	(Assoc. Prof. Dr.Sirikul Wisutmethangoon)
.....	.....
(Asst. Prof. Dr.Thawatchai Plookphol)	(Asst. Prof. Dr.Thawatchai Plookphol)
.....	.....
(Assoc. Prof. Dr.Jessada Wannasin)	(Asst. Prof. Dr.Prapas Muangjunburee)
.....	
(Prof. Dr.Susan E. Babcock)	

The Graduate School, Prince of Songkla University, has approved this thesis as Partial Fulfillment of the Requirements for the Degree of Doctor of Engineering in Materials Engineering

.....

(Prof. Dr.Amornrat Phongdara)

Dean of Graduate School

ชื่อวิทยานิพนธ์ โครงสร้างจุลภาคและสมบัติของอะลูมิเนียมผสม 7075 ที่ขึ้นรูปด้วยเทคโนโลยีโลหะกึ่งของแข็งหลังจากผ่านกระบวนการทางความร้อน
ผู้เขียน นางนริศรา มหาธนินวงศ์
สาขาวิชา วิศวกรรมวัสดุ
ปีการศึกษา 2554

บทคัดย่อ

ในงานวิจัยนี้ศึกษาอิทธิพลของอุณหภูมิและระยะเวลาในขั้นตอนการอบละลายและการบ่มต่อโครงสร้างจุลภาคและสมบัติทางกลของอะลูมิเนียมผสม 7075 ที่ขึ้นรูปด้วยเทคโนโลยีโลหะกึ่งของแข็ง ซึ่งพบว่าอุณหภูมิและระยะเวลาในการอบละลายที่เหมาะสมของอะลูมิเนียมผสม 7075 ที่ขึ้นรูปด้วยเทคโนโลยีโลหะกึ่งของแข็งที่มีโครงสร้างจุลภาคแบบไม่เป็นกิ่งไม้ คือ 450 °C ระยะเวลา 4 ชั่วโมง ส่วนในขั้นตอนการบ่มทำการศึกษาที่อุณหภูมิ 120 °C 145 °C 165 °C และ 185 °C ณ ระยะเวลาต่างๆ พบว่าสภาวะการบ่มที่อุณหภูมิ 120 °C ระยะเวลา 72 ชั่วโมงให้ค่าความแข็งสูงสุดที่ 90 HRB และให้ค่าความแข็งแรงการดึงสูงสุดที่ 486 MPa โดยมีเปอร์เซ็นต์การยืดเท่ากับ 2% ความแข็งแรงที่สภาวะดังกล่าวเป็นผลมาจากการพรีซิพิเทตกึ่งเสถียรเฟส η' ขนาดละเอียดและความหนาแน่นสูงกว่าที่อุณหภูมิการบ่มอื่นๆ ดังนั้นเฟส η' เป็นเฟสหลักที่ทำให้อะลูมิเนียมผสม 7075 ที่ขึ้นรูปด้วยเทคโนโลยีโลหะกึ่งของแข็ง มีความแข็งแรงหลังการบ่มแข็งเทียบเท่ากับอะลูมิเนียมผสม 7075 ที่ขึ้นรูปด้วยกระบวนการ thixoforming ทั้งนี้การบ่มที่อุณหภูมิสูงขึ้นพรีซิเทตเฟสเสถียร η จะเริ่มก่อตัวทำให้ความแข็งแรงของอะลูมิเนียมผสม 7075 ที่ขึ้นรูปด้วยเทคโนโลยีโลหะกึ่งของแข็งลดลง จากการหาค่าพลังงานกระตุ้นปรากฏของกระบวนการพรีซิพิเทตของอะลูมิเนียมผสม 7075 ที่ขึ้นรูปด้วยเทคโนโลยีโลหะกึ่งของแข็ง เท่ากับ 95,827 J/mol

จากการศึกษาสมบัติการแตกหักเนื่องจากการคืบของอะลูมิเนียมผสม 7075-T6 ที่ขึ้นรูปด้วยเทคโนโลยีโลหะกึ่งของแข็งด้วยเทคนิค GISS และผ่านกระบวนการทางความร้อนแบบ T6 ที่อุณหภูมิอบละลาย 450°C ระยะเวลา 4 ชั่วโมง และผ่านการบ่มที่อุณหภูมิ 120°C ระยะเวลา 72 ชั่วโมง โดยทำการเปรียบเทียบกับอะลูมีเนียมผสม 7075-T651 ในทางการค้า พบว่าอะลูมิเนียมทั้งสองชนิดมีค่ากำลังความเค้น (n) ที่เท่ากันเท่ากับ 6.3 ซึ่งเป็นข้อมูลส่วนหนึ่งที่บอกได้ว่าดิสโลเคชันเป็นกลไกหลักในการควบคุมการคืบของอะลูมิเนียมทั้งสองชนิด นอกจากนี้ยังพบว่าอะลูมิเนียมผสม 7075-T6 ที่ขึ้นรูปด้วยเทคโนโลยีโลหะกึ่งของแข็งมีอัตราการคืบต่ำสุดต่ำกว่าและระยะเวลาการแตกหักเนื่องจากการคืบยาวนานกว่าอะลูมิเนียมผสม 7075-T651 ในทางการค้า โดยที่

ระยะเวลาการแตกหักเนื่องจากคืบของอะลูมิเนียมผสม 7075-T6 ที่ขึ้นรูปด้วยเทคโนโลยีโลหะกึ่งของแข็งยาวนานกว่าอย่างชัดเจนที่ช่วงความเค้น 120-140 MPa เนื่องจากมีความแน่นของพรีซิพิเทตที่สูงกว่าและอัตราการเติบโตของพรีซิพิเทตที่ช้ากว่าอะลูมิเนียมผสม 7075-T651 ในทางการค้า อย่างไรก็ตามการเกิดช่องว่างเนื่องจากการคืบ(creep cavities) เป็นกลไกหลักในการควบคุมการแตกหักเนื่องจากการคืบของอะลูมิเนียมผสม 7075-T6 ที่ขึ้นรูปด้วยเทคโนโลยีโลหะกึ่งของแข็ง ขณะที่การแตกหักเนื่องจากการคืบของอะลูมิเนียมผสม 7075-T651 ในทางการค้าถูกควบคุมร่วมกันของการเติบโตของพรีซิพิเทตอย่างรวดเร็วและการเกิดช่องว่างเนื่องจากการคืบ ทั้งนี้การสูญเสียการยึดเหนี่ยว(decohesion)ของอนุภาคอินเตอร์เมทัลลิกเฟส Al-Fe-Cu กับเนื้อเมทริกซ์ เชื่อว่าจะถูกเร่งให้เกิดที่ความเค้นสูง 180MPa ให้เกิดช่องว่างขนาดใหญ่และเป็นบริเวณกว้าง และในที่สุดทำให้ของอะลูมีเนียมผสม 7075-T6 ที่ขึ้นรูปในสถานะกึ่งของแข็งจะแตกหักเนื่องจากการคืบเร็วขึ้นและใกล้เคียงกับอะลูมีเนียมผสม 7075-T651 ในทางการค้า

Thesis Title	Microstructure and Properties of Semi-Solid Al Alloy 7075 after Heat Treatment
Author	Mrs. Narissara Mahathninwong
Major Program	Materials Engineering
Academic Year	2011

ABSTRACT

Effects of solution heat treatment and age hardening on the microstructures and mechanical properties of rheocasting 7075 Al alloy produced by a novel technique, Gas Induced Semi-Solid (GISS) technique, were studied. This work reveals that the optimum solution heat treatment condition for the non-dendritic structured 7075 aluminium alloy was 450 $^{\circ}$C for 4 h. Age hardening was performed at temperatures of 120 $^{\circ}$C, 145 $^{\circ}$C, 165 $^{\circ}$C, and 185 $^{\circ}$C under various time durations. The peak aging condition was the artificial aging at 120 $^{\circ}$C for 72 h, at which a highest tensile strength of 486 MPa with 2% elongation was recorded. This higher strength was caused by higher number density and finer precipitate size of η' phase than other aging temperatures. The main hardening phase was identified to be the η' phase while early nucleation of η phase in the higher aging temperature specimens resulted in lower strengths of the alloy. The activation energy for the precipitate hardening process of the alloy derived in this research was 95,827 J/mol

Creep rupture behavior of semi-solid cast 7075-T6 Al alloy produced by Gas Induced Semi-Solid (GISS) process was investigated in comparison with commercial 7075-T651 Al alloy. The semi-solid cast 7075-T6 Al alloy displayed lower minimum creep rate and longer creep rupture time than the commercial 7075-T651 Al alloy. On the basis that their n values were 6.3, dislocation creep was seemingly the predominant mechanism controlling the creep deformation of both alloys. Creep rupture time of the semi-solid cast 7075-T6 Al alloy is distinctly longer than that of the commercial 7075-T651 Al alloy at stress regimes of 120-140 MPa due to the lower precipitate coarsening and higher precipitate density. Creep cavities predominately controlled creep rupture of the semi-solid cast 7075-T6 Al alloy despite the appearance of precipitate coarsening. The commercial 7075-T651 Al alloy creep rupture behavior

was controlled by the combination of rapid precipitate coarsening and creep cavities. However, de-cohesion between insoluble particles and the matrix is evidently accelerated with increasing stress to 180 MPa, leading to cavity propagation and resulting in the convergence of creep rupture time in the semi-solid cast 7075-T6 Al alloy to that of the commercial 7075-T651 Al alloy.

ACKNOWLEDGEMENT

First of all, the author would like to express her sincere gratitude to her main advisors, Assoc. Prof. Dr. Sirikul Wisutmethangoon, and her three co-advisors of Asst. Prof. Dr. Thawatchai Plookphol, Asst. Prof. Dr. Jessada Wannasin, and Prof. Dr. Susan E. Babcock, and also extend thank to Asst. Prof. Dr. Prapas Muangjunburee for his help and guidance.

High tribute shall be paid to the external committee, Assoc. Prof. Dr. Chaowalit Limmaneevichitr.

In addition, the authors wish to acknowledge the Prince of Songkla University for the 50% Ph.D. scholarship financial support, as well as supports from the Thailand Research Fund through the Royal Golden Jubilee Ph.D. Program (Grant No.PHD/0031/2552), and the Office of National Research Council of Thailand through the Development of High-Quality and Low-Cost Below Knee Prosthesis Project, including the PSU Graduate School. On the other hand, the author would like to thank the all laboratory facility supports from the PSU Department of Mining and Materials Engineering, the Department of Industrial Engineering, and Department of Materials science and Engineering, College of Engineering, University of Wisconsin-Madison, WI, USA. The assistance with the manuscript preparation from Mr. Wiwat Sutiwipakorn is also acknowledged.

The author would like to express her thank to all her colleagues from the Heat Treatment and Particle Materials (HTPM) group, Innovative Materials Technology (IMT) group, Joining & Welding group of Department of Mining and Materials Engineering, Prince of Songkla University.

Finally, the author would like to thank all supports and encouragements from her parents (Mr. Udon Sumangkay and Mrs. Jaree Sumangkay), as well as her husband (Mr. Suratit Mahathaninwong) and her son (Master. Aob Mahathaninwong), including her younger sister and brother (Mrs. Aunchalee, Mr. Ayut, and Miss Kanokrat Sumangkay).

Narissara Mahathaninwong

CONTENT

CONTENT (CONTINUE)

LIST OF TABLES

LIST OF FIGURES

LIST OF FIGURES (CONTINUE)

LIST OF FIGURES (CONTINUE)

Page

LIST OF FIGURES (CONTINUE)

LIST OF FIGURES (CONTINUE)

CHAPTER 1

INTRODUCTION

1.1 Background and Rational

7075 Aluminium alloy was developed over 70 years ago. However, many researches still have been performed on it in the past decade [1]-[11]. High strength and light weight properties of the alloy are attractive properties leading to its prevalent usage in transport applications corresponding to constantly increasing global warming concerns. In addition, 7075 Al alloy is being put into lightweight components of lower limb prostheses [12].

7075 Aluminium alloy was commonly formed by wrought manufacturing process which resulted in high strength. However, the cost of this production route is very high compared to the alternative casting route. Nevertheless, disadvantages of conventional casting are found in the material structure with existence of casting defects such as pores and shrinkage cavities, including lower strength [1], [13]. An alternative Semi-Solid Metal (SSM) process was developed in early 1971 [14]. Reduction in casting temperature and solidification shrinkage is its main advantage [15]. This SSM process has since been developed into thixocasting and rheocasting processes.

Rheocasting process has increasingly gained attentions from many researchers because of less investment and lower raw material cost compared to thixocasting process. Hence, rheocasting process will be the alternative process to obtain higher strength alloys than cast alloy requirements. Various techniques for semisolid slurry preparations of 7075 Al alloy had been proposed such as cooling slope [3], induction stirring with simultaneous forced air cooling [16], and a novel technique of rheocasting process developed by the Innovative Metal Technology (IMT) team of the Prince of Songkla University. This technique is called Gas Induce Semi-Solid (GISS) technique [12]. It is a simple, economical and efficient process. Additionally, this technique has succeeded to produce non-dendritic structure of 7075 alloy.

However, in order to obtain high strength 7075 Al alloy, heat treatment is a key process to improve mechanical properties after the forming process. T6 heat treatment is one of

the major factors to enhance mechanical properties of the alloy. It involves three main steps: solution heat treatment, quenching, and artificial aging. The solution heat treatment step aims to dissolve segregated elements and soluble phases into matrix as solid solution. The formation of precipitates after artificial aging contributed to the strengthening increase. The precipitation sequence of 7xxx Al alloy was proposed as followed [17]-[19];

$$\text{SSS} \text{ ------- > GP Zone ------- > } \eta' \text{ ------- > } \eta\,(MgZn_2)$$

Stable η phase has been characterized to be the platelet-like shape and hexagonal structure model, while the coherence interface of meta-stable η' phase with the matrix has been reported. The hardening responsible of individual fine η' phase has been proposed, together with a combination of GP Zone and η' phase. The precipitate type, size, and density could be controlled though an optimum aging temperature and time. Therefore, an optimization of both the solution heat treatment and the artificial aging conditions applied to the alloy is crucial in achieving the required properties [5, 20]. T6 heat treatment schedule of wrought 7075 Al alloy were well established at the solution temperature range of 465-490°C and aging temperature of 120°C [21]. In contrast, dissolving soluble phases of the as-cast 7075 Al alloy should be done at temperature lower than 465°C as advised by Mukhopadhyay [22]. Moreover, various aging times at 120°C for 7075 Al alloy have been proposed to be the peak-aged condition of T6 heat treatment [10], [11].

As the difference in as-fabricated microstructures led to the differences in solution heat treatment and artificial aging conditions, this work hence aims to establish T6 heat treatment data of the 7075 Al alloy produced by rheocasting process along with a GISS technique. T6 heat treatment study of the alloy is focused into two main sections; solution heat treatment and artificial aging. The influence of solution heat treatment and artificial aging temperature and time on mechanical properties and microstructures was investigated.

On the other hand, it is well known that the wrought 7075-T6 Al alloy is one of the precipitate-hardening alloys that possess excellent mechanical properties at temperature between 25°C to 100°C. However, its tensile strength sharply decreases with increasing temperature at temperatures above 100°C [23]. For example, tensile strength of commercial

7075-T651 Al alloy decreased from 598 MPa at 25 °C to 297 MPa at 200 °C [24]. Microstructure stability enhanced creep resistance of 7075 Al alloy by addition of Zr, which forms small precipitates of Al_3Zr has been achieved as a stable dispersoid phase [25]. In contrary, precipitate coarsening of 7010 Al alloy (having composition similar to 7075 Al alloy) during creep was found to exhibit loss in creep strength [26]. Rapid precipitate coarsening rate occurred together with strong interfacial energy between the precipitate and the matrix when it was applied in high temperature applications [27], [28]. Furthermore, over-aged precipitates in Al-Zr alloy also resulted in creep resistance loss [29]. Therefore, fine dispersion precipitates obtained through an optimum T6 heat treatment present a possibility to increase creep resistance for precipitate-hardening alloys. 7075 Al alloy commonly produced by wrought process has been widely studied for its creep properties [30]-[32]. However, semi-solid cast 7075 Al alloy produced by a novel Gas Induced Semi-Solid (GISS) process with the formation of fine dispersion precipitate through the optimum T6 heat treatment condition has never been studied before.

Consequently, the study in the creep property of semi-solid cast 7075-T6 Al alloy produced by GISS process is the second part of this research. The investigations focused on the creep rupture behavior of the alloy and the microstructure examination prior to and after testing to gain a better understanding of the mechanism governing this behavior. The creep rupture of the commercial 7075-T651 Al alloy examined in parallel for comparison.

1.2 Objectives

1.2.1 To improve the mechanical properties of the semi-solid cast 7075 Aluminium alloy produced by GISS process through heat treatment.

1.2.2 To investigate the influence of the heat treatment on creep property of the semi-solid cast 7075 Aluminium alloy produced by GISS process.

1.2.3 To characterize microstructures of semi-solid cast 7075 Aluminium alloy produced by GISS process after heat treatment.

1.3 Significance of the Study

1.3.1 Obtain the suitable heat treatment for improving the mechanical properties and creep property of the semi-solid cast 7075 Aluminium alloy produced by GISS process.

1.3.2 Provide the influence of heat treatment on microstructures of the semi-solid cast 7075 Aluminium alloy produced by GISS process.

1.4 Scope of the Study

1.4.1 The semi-solid cast 7075 Aluminium alloy produced by GISS process is studied in this research.

1.4.2 The temperatures, times, and steps of heat treatment for the semi-solid cast 7075 Aluminium alloy produced by GISS process are investigated.

1.4.3 Hardness, tensile, and creep property of the semi-solid cast 7075 Aluminium alloy produced by GISS process after heat treatment are evaluated.

1.4.4 Microstructure characterizations of the semi-solid cast 7075 Aluminium alloy produced by GISS process after heat treatment and creep test are examined by Optical Microscopy (OM), Scanning Electron Microscopy (SEM), and Transmission Electron Microscopy (TEM)

1.5 Research places

1.5.1 Department of Mining and Materials Engineering, Faculty of Engineering, Prince of Songkla University.

1.5.2 Department of Industrial Engineering, Faculty of Engineering, Prince of Songkla University.

1.5.3 Scientific Equipment Center, Prince of Songkla University.

1.5.4 National Metal and Materials Technology Center, 114 Thailand Science Park Paholyothin Rd., Klong 1, Klong Luang, Pathumthani 12120 Thailand.

1.5.5 Department of Materials Science and Engineering, College of Engineering, University of Wisconsin-Madison, Madison, Wisconsin, 53706 United State of America.

CHARPTER 2

REVIEW OF LITERATURES

2.1 Aluminium Alloy

Aluminium alloy has been widely used in automotive, aerospace, transportation and defense industries where they have been steadily replacing many conventional ferrous alloys, which it could be produced in a variety of forming processes depending on the view of the investment cost, the product size, and the property requirement. However, the difference in alloying elements contained in Al alloy led to obtain a variety of properties for Al alloy. Al alloy was categorized following the alloying elements;

Al alloy containing high Si content : Al-Si alloy group is good castability because of its less shrinkage, high fluidity, less entrapping gases, and less cracking during solidifications. However, Al-12%Si is non-heat treatable.

Al-Si-Cu alloy, Al-Si alloy with adding Cu element led to its heat treatable alloy due to precipitate hardening. Al-5%Si-3%Cu could be solution treated at temperature ranging from 505 $^{\circ}$C to 520 $^{\circ}$C for 6-16 h, and quenched in the water afterward. Artificial aging was subsequent at temperature ranging from 150 $^{\circ}$C to 170 $^{\circ}$C for 6-18 h led to obtain the high static force resistance. The developed Al alloy, Al-11%Si-3%Cu, could be T5 heat treated at temperature interval of 200 $^{\circ}$C-210 $^{\circ}$C for 7-9 h, which it achieved to increase the strength from 190 MPa in as-cast specimen to 250-320 MPa, together with reduction in heat treatment cost.

Al-Si-Mg alloys were good castability and properties more than Al-Si-Cu alloys. Solution heat treatment and artificial aging for Al-7%Si-0.3%Mg has been suggested to be done at 535 $^{\circ}$C for 2-6 h and 150 $^{\circ}$C-180 $^{\circ}$C for 3-5 h, respectively.

Al-Si-Cu-Mg alloy was good properties of as-cat products and less entrapping gases and cracking affects. This alloy with high Cu and low Mg contained $CuAl_2$ phase in its microstructure, while Mg_2Si phase appeared at high containing Mg and low containing Cu alloys. In addition, high impurity Fe content resulted in the formation of the AlCuSiFe phase, which could be dissolved during solution heat treatment stage and may be contributed to the

strengthening through precipitate process. The precipitation of both $CuAl_2$ and Mg_2Si enhanced the strengthening of the alloys. This Al alloy group was solution treated at 525 $^{\circ}$C for 6 h, followed by quench in hot water, and natural aged for 5 days afterward, which gave the strength of 270 MPa with %elongation of 0.8%. When artificial aging at 225 $^{\circ}$C for 5, the %elongation was increased to 1.8%, with no reduction in strength.

Al alloy containing high Mg contents : Commercial Al-10%Mg alloy group has high corrosion resistance and high strength of 450MPa with high elongation of 10-20%. This alloy has been extensively used in the sea applications. T6 heat treated of this alloy resulted in increasing ductility. Higher strength with decreasing elongation, brittle property, was produced by the natural aging because of the formation of β phase at grain boundary. Decreasing in Mg content of 8% with adding Zn of 1.5% could be used to avoid the precipitation of β phase. Instead, it would rather form $Mg_3Zn_3Al_2$ phase.

Al alloy containing high Cu contents : This alloy is the oldest casting Al alloy group. Al-4.5%Cu alloy has been produced as the small machines with non complicate shapes for applied in airplane by casting process. The alloy is also suitable to form by casting with using high stress. Binary Al-Cu alloy composed of α -Al and $CuAl_2$ phases. Al-Cu alloy with high Cu contents led to the larger grain sizes and longer solution treatment times, normally 15-16 h for completely dissolved solid solution. In addition, quenching should be done immediately after solution heat treatment because the rapidly diffusion of Cu was out of Al matrix. For artificial aging, temperature of 120 $^{\circ}$C-170 $^{\circ}$C for 12-14 h was suggested.

Al-Zn-Mg-Cu alloy : Binary Al-Zn alloy has been widely used as the anodes for protecting the ferrous structure applied in the sea. In engineering, addition of Mg and other elements such as Cu, Cr, and Fe could be enhanced the strength and applied to airplane components. 7075 Al alloy is one of Al-Zn-Mg-Cu alloy group, which the standard composition of it is shown in table 2.1[33].

Table 2.1 Standard chemical compositions of the 7075 Al alloy.

Major Elements	**Al**	**Zn**	**Mg**	**Cu**
%wt	87.1-91.4	5.1-6.1	2.1-2.9	1.2-2.0

Table 2.1 (Continue)

Elements	Fe	Si	Mn	Ti	Cr	other
%wt	Max. 0.5	Max. 0.4	Max 0.3	Max 0.2	0.18-0.28	0.15

The solidus and liquid temperature of 7075 Al alloy were at 477 °C and 635 °C [34], respectively. The 7075 Al alloy was developed in the yeas 1930-1940 in the reason of the need the alloy with having the high strength to weight ratio. Zn and Mg elements were the high solubility element in the Al matrix. The alloy could be designed the grain structure through the controlling parameters in the forming process and heat treatment [33]. Addition of Cu element had the influence on the increasing mechanical property of the alloy caused by its enhancement nucleation of GP zones [35].

2.2 Heat Treatment of Aluminium alloys

Table 2.2 Solid solubility of elements in the aluminium matrix [33].

		Maximum solid solubility	
Element	Temperature (°C)	(wt%)	(at%)
Cadmium	649	0.4	0.09
Cobalt	657	<0.02	<0.01
Copper	548	5.65	2.40
Chromium	661	0.77	0.40
Germanium	424	7.2	2.7
Iron	655	0.05	0.025
Lithium	600	4.2	16.3
Magnesium	450	17.4	18.5
Manganese	658	1.82	0.90
Nickel	640	0.04	0.02
Silicon	577	1.65	1.59
Silver	566	55.6	23.8
Tin	228	~0.06	~0.01
Titanium	665	~1.3	~0.74
Vanadium	661	~0.4	~0.21
Zinc	443	82.8	66.4
Zirconium	660.5	0.28	0.08

Note:
(i) Maximum solid solubility occurs at eutectic temperatures for all elements except chromium, titanium, vanadium, zinc and zirconium for which it occurs at peritectic temperatures.
(ii) Solid solubility at 20 °C is estimated to be approximately 2 wt% for magnesium and zinc, 0.1–0.2 wt% for germanium, lithium and silver and below 0.1% for all other elements.

Although most metal elements will contain in Al alloy, a few alloying elements could be soluble as solid solution. A significant solubilities of alloying elements as solid solution were only Zn, Mg, Cu, and Si elements, as revealed in table 2.2. However, transition elements could be soluble below 1%at such as Cr, Mn, and Zr. These elements were primarily to form compounds which control grain structure. With the exception of hydrogen, elemental gases were not soluble in either liquid or solid Al.

High purified Al has very low yield strength of 7-11 MPa after annealing. Increasing in the strength of annealed materials achieved in which solutes dissolved in solid solution, which it should be annealed at the optimum temperature for the dissolution of solid solution. In addition, the solid solutions still remain after quenching without remove to react with other elements to form insoluble phases.

Aluminium alloys could be divided into two groups. One contains those alloys for which the mechanical properties are controlled by work hardening and annealing such as Al-Mg and Al-Mn systems. The second Al alloy group responds to age or precipitate hardening such as Al-Cu-Mg, Al-Mg-Si and Al-Zn-Mg-Cu

2.2.1 Principle of Age Hardening

The basic requirement for an alloy to be amenable to aged hardening is a decrease in solid solubility of one or more of the alloying elements with decreasing temperature. Heat treatment normally involves the following stages;

1. **Solution Heat Treatment** : This stage was to dissolve the alloying element, which it should be done at a relatively high temperature within the single α-Al phase region, as phase diagram of Al-Zn-Mg Al alloy in Fig 2.1.

It should be also concerned that the solution treatment temperature was not over the solidus temperature of the alloys. The compounds will be melted with over solidus temperature. The study of Al-Zn-Mg-Cu Al alloy(7010 and 7055) found that the area fraction of eutectic phases decrease with increasing solution treatment temperatures and times, as shown in Fig. 2.2. Before solution treatment, microstructure of Al-Zn-Mg-Cu Al alloy composed of an α-Al phase and lamella eutectic phases(α-Al+$Mg(Al,Cu,Zn)_2$, including a τ-Al_7Cu_2Fe phase

embedded in the eutectic phases, as depicted in Fig. 2.3 (a)-(b). The eutectic disappeared after 24 h homogenization at 460 °C, while the particles of τ-Al_7Cu_2Fe และ Al_2CuMg still appeared in the microstructures, as revealed in Fig 2.3(c) 7050 and 2.3(d) 7010. The morphology of τ-Al_7Cu_2Fe and Al_2CuMg particles were shown in Fig. 2.3(e) and 2.3(f).

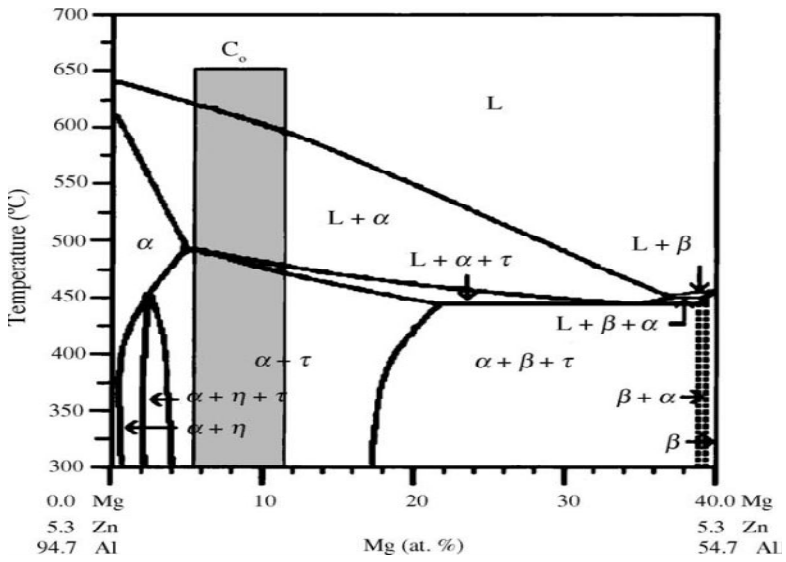

Fig. 2.1 Phase diagram of Al-Zn-Mg Al alloy at the content of Zn-5.3 at%. A vertical bar, the alloy composition of interest [36].

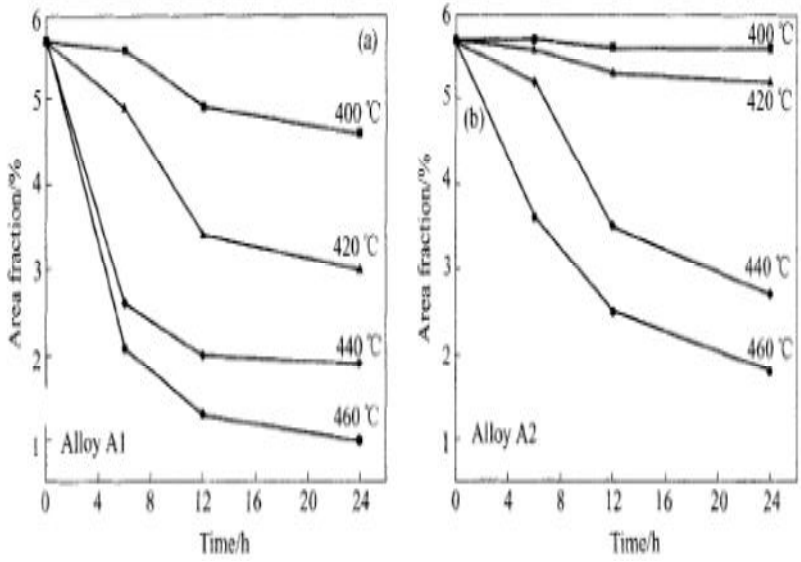

Fig. 2.2 Area fraction of phases other α-Al during solution heat treatment at 400, 420, 440, and 460 °C for various times a) Alloy A1(7050) b) Alloy 2 (7010) [37].

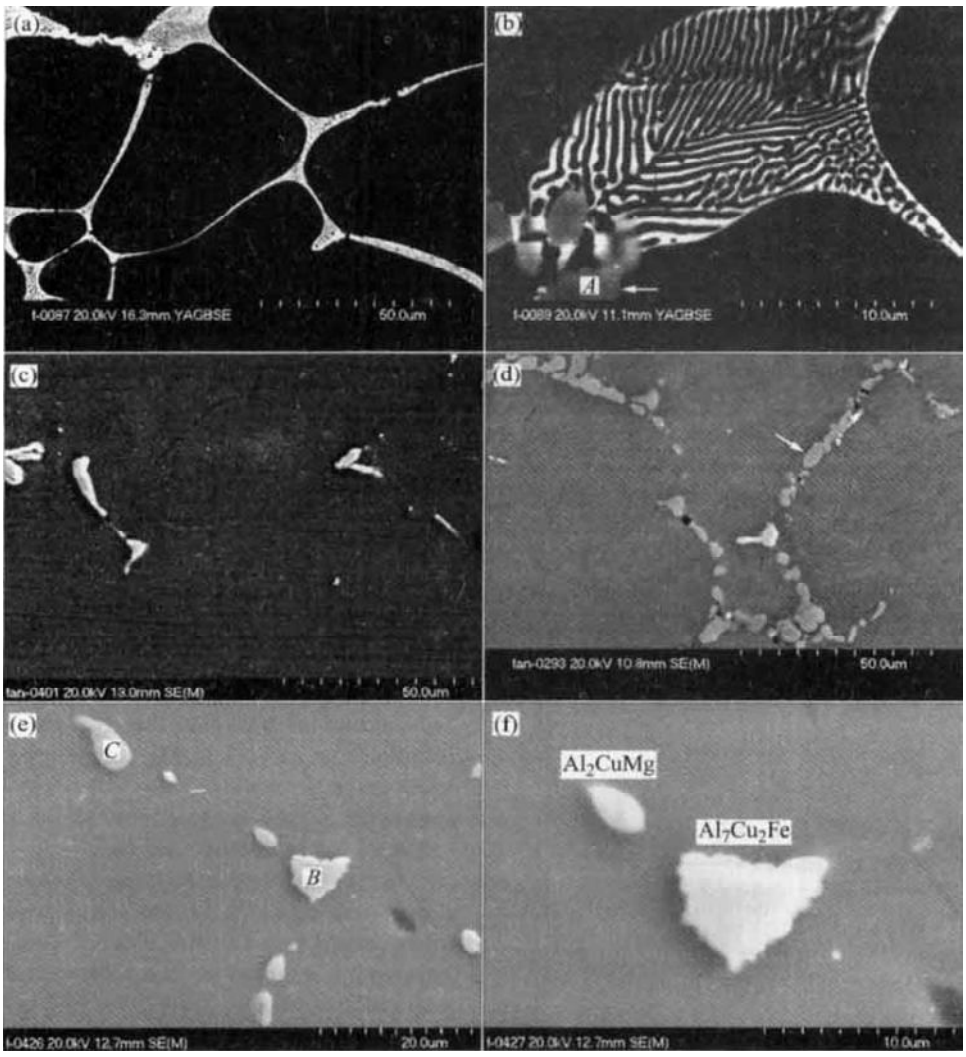

Fig. 2.3 SEM micrographs of two alloys under different heat treatment conditions: (a) As cast microstructures; (b) High magnification of Fig. 2.3(a); (c) 7050 Al alloy (460 °C, 24 h); (d) 7010 Al alloy (460 °C, 24 h); (e) Morphology of coarse particles; (f) High magnification of Fig. 2.3(e) [37].

2. Quenching Quenching is the stage of rapid cooling materials to room temperature after solution heat treatment providing a supper saturated solid solution of alloying elements in aluminium. The water is usually used to be a quenching medium due to its high efficiency for cooling material. The cooling rate has the influence on the mechanical properties of materials after heat treatment [38], as the graph in Fig. 2.4. It could be seen that high cooling rate resulted in the increasing tensile strength of 7XXX, 2XXX, and 6XXX Al alloys [21]. However,

the high cooling rate produces large temperature gradients between thick and thin sections which cause a localized plastic flow and an internal stress, which in turn results in a distortion after quenching. It has been reported that samples were less distorted after quenching with glycol [6]. The distortion effect mostly found to long depth and thinnest samples. Quenching in either hot water or air is then an alternative way. Quenching with low cooling rate resulted in a precipitation. It was found that 7010 Al alloy was cooled down slowly from solution treatment temperature of 475 $^{\circ}$C, η phase formed subsequently at a temperature of lower 440 $^{\circ}$C whereas an appearance of S and T phases was at temperature ranging from 200°C to 300°C. With lower temperatures, η' phase occurred at temperature of interval 100°C-200°C and GP zone also initiated at temperature of 130°C. In addition, heterogeneous site precipitates formed at higher temperatures, while the formation of homogeneous site precipitates was at lower temperature, as a diagram of an ordered precipitation formation during cooling in Fig. 2.5 [39].

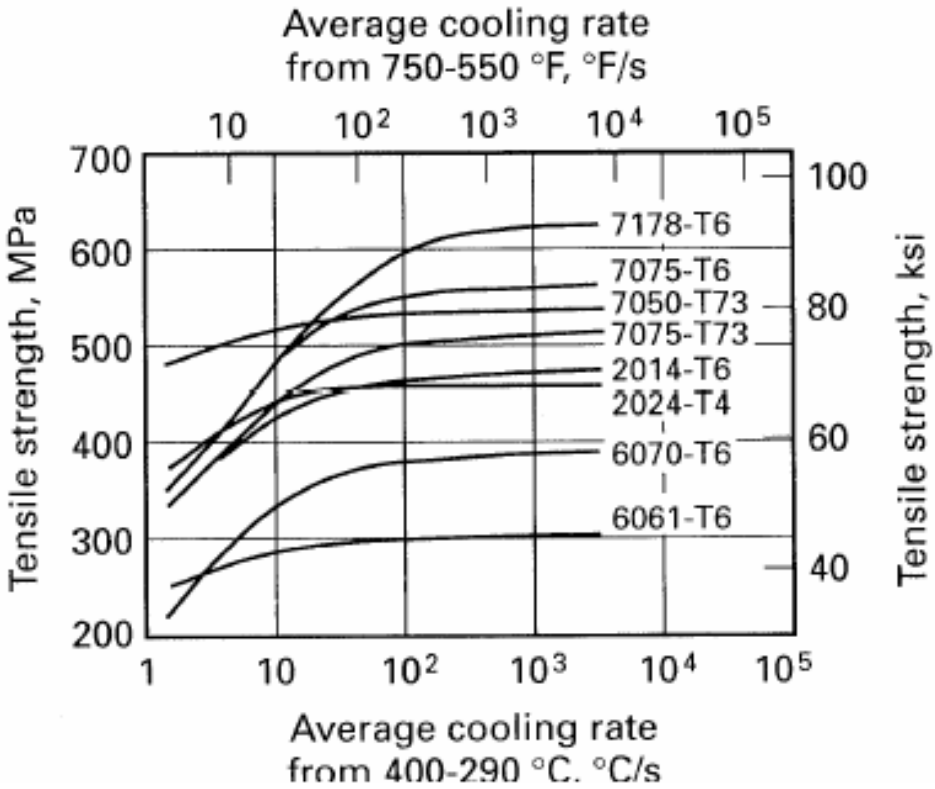

Fig. 2.4 Influence of the cooling rate on the tensile strength of Al alloys [21].

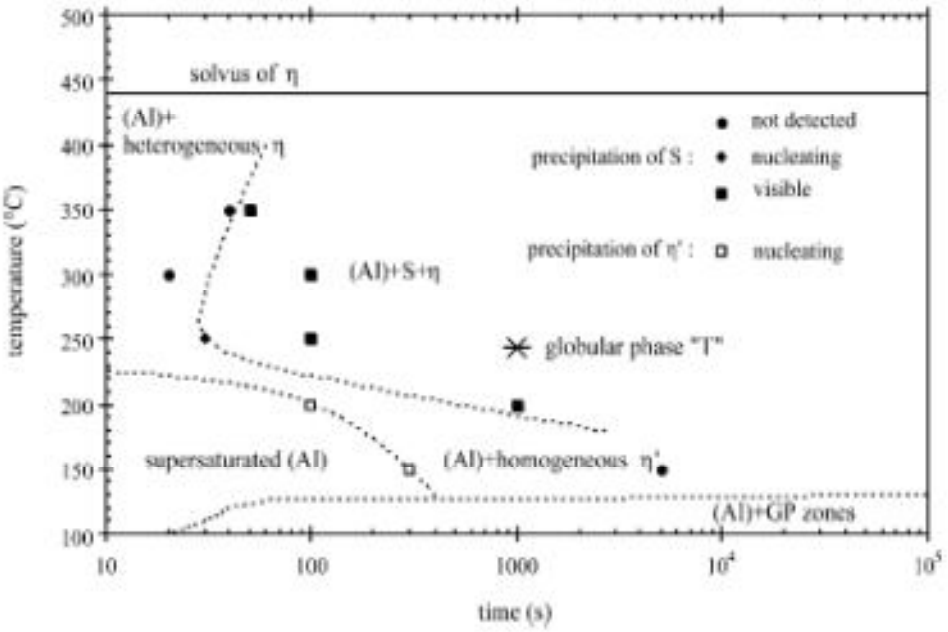

Fig. 2.5 A precipitate nucleation diagram of 7010 Al alloy during quenching [39].

3. Aging

Aging is a stage of controlled decomposition of a super-saturated solid solution to form a finely dispersed precipitate, which is usually by aging for optimum times at either one or sometime intermediate temperatures. The complete decomposition of the super-saturated solid solution is a complex process together with involving several stages. Typically, Guinier-Preston(GP) zone and an intermediate precipitate may be formed in addition to the equilibrium phase. In the Al-Zn-Mg-Cu system, precipitate sequences has been proposed as 3 stages, as followed [40] :

GP Zone ------- > η' ------- > η ($MgZn_2$)

The element mapping study with novel technique of 3D Atomic Probe Field Ion Microscopy (APFIM) revealed spherical and elliptical GP zone shapes for Al-Zn-Mg-Cu Al alloy [36], as depicted in Fig. 2.6. Moreover, it has been reported that GP zones was classified to be the GP zone I and the GP zone II [41]. GP I, internally ordered on {100}-planes, spherical zones with 2–3 nm in diameter, whereas GP II are zones a few atoms thick on {111}-Al planes [18], [42]. Zhihui et al. [43] found the GP zone I in Al alloy (Al-6.23Zn-2.88Mg-1.58Cu) formed at aging temperatures in the range from room temperature to 150^{o}C, GP zone II initially formed at

either temperature over 450°C after quenching or aging temperatures over 70°C. Fig. 2.7 displays the morphology of GP zone I and GP zone II.

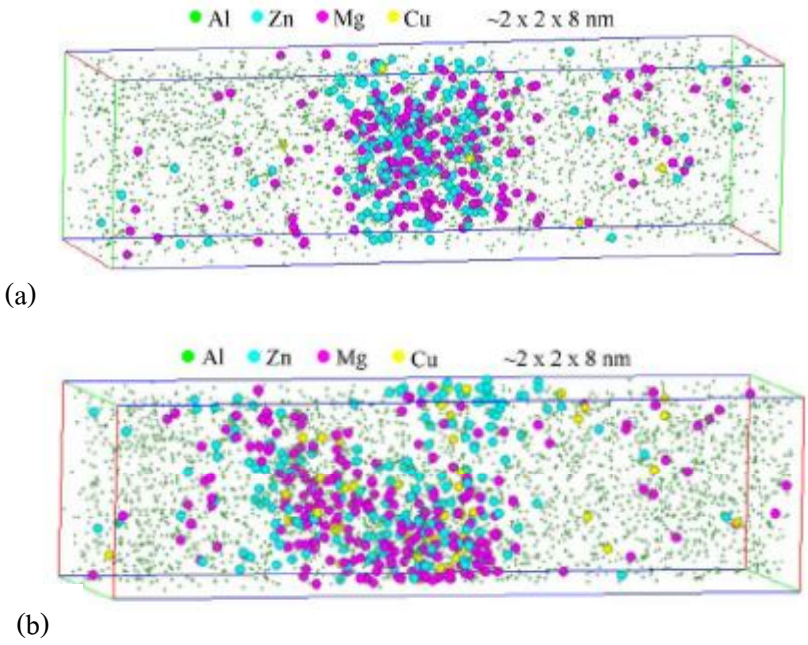

Fig. 2.6 Element mapping 3DAP of GP Zone in Al-Zn-Mg-Cu system (a) spherical GP Zone shape (b) ellipsoidal GP Zone shape [35].

GP Zones are solute-rich groups of either only one or two atom planes in thickness. Although they can produce appreciable elastic strains in the surrounding matrix, they are coherent with the matrix. Diffusion associated with their formation involves the movement of atom over relatively short distances and is assisted by vacant lattice sites that are also retained on quenching. GP zones are normally very finely dispersed and densities may be as high as 10^{17} - 10^{18} cm^{-3}. The nucleation rate and the actual structure may be greatly influenced by the presence of the excess vacant lattice sites.

The intermediate precipitate is commonly much larger in size than a GP zone and is only partly coherent with the lattice planes of the matrix. It has been generally accepted to have a definite composition and crystal structure both of which differ only slightly from those of the equilibrium precipitate. In some Al alloys, the intermediate precipitate may be precipitate from, or at, the sites of stable GP zones. In others this phase nucleates heterogeneously at

dislocation or particles such as Al_3Zr. The shape and hexagonal crystal structure of intermediate precipitate η' phase showed in Fig. 2.8.

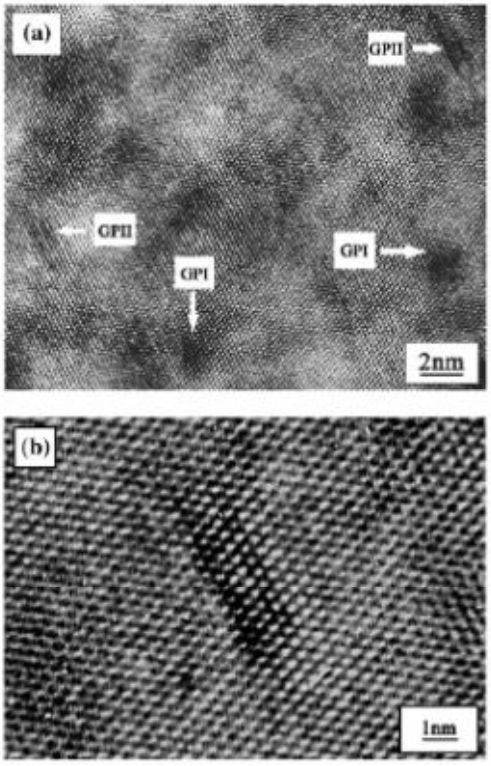

Fig. 2.7 HREM micrographs showing (a) GP Zone I and GP Zone II (b) high magnification micrograph of GP Zone II [43].

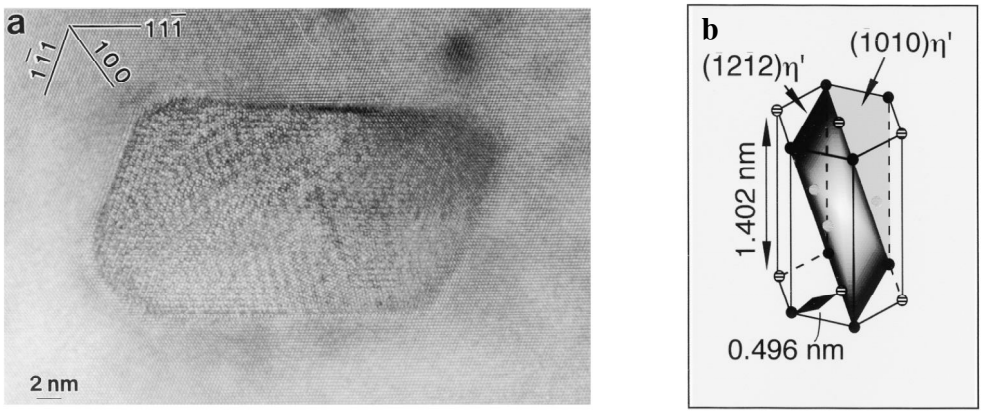

Fig. 2.8 (a) HRTEM image of η' in Al-1.7Zn-3.4Mg-0.1Ag Al alloy (b) crystal structure of η' [44].

Most aluminium alloys respond to aging, especially Al-Zn-Mg-Cu alloy group. Aging at ambient temperatures is called “natural ageing” that the rate of precipitations is extremely than that of at elevated temperatures which has well known as “artificial aging”. Fig. 2.9 shows a Time-Temperature-Transformation (TTT) diagram of Al-6.1Zn-2.4Mg-1.6Cu (7075 Al alloy) in which a formation of precipitate varies to aging temperatures and time. The shaded B area corresponds to a maximum YS. A area corresponds first-stage ageing regimes with minimum duration, at which precipitates of GP2 and η' phase, inherited in the case of second-stage ageing at 160–180 $^{\circ}$C, are forming [45].

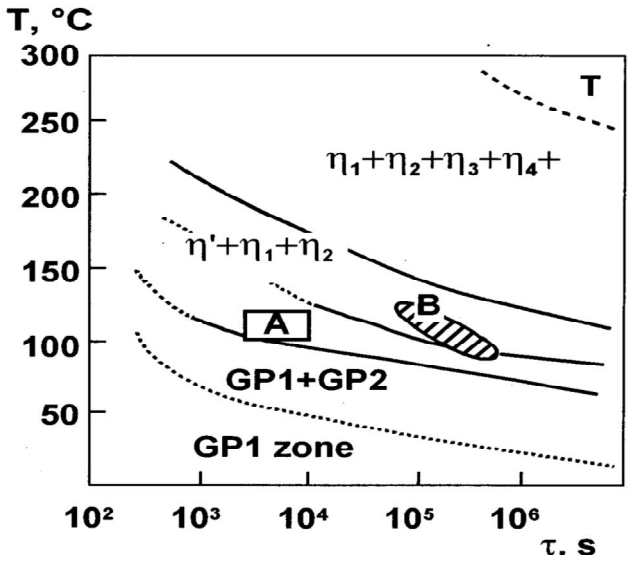

Fig. 2.9 TTT diagram for ageing of Al–6.1Zn–2.4Mg–1.6Cu (wt.%) alloy [45].

At one particular temperature, which varies with each alloy, the highest value of hardness will be recorded. Softening that occurs on prolonged artificial ageing is known as “overaging”. In commercial heat treatment, an aging treatment is usually selected that gives a desired response to hardening (strengthening) in a convenient period of time.

Maximum hardening in aluminium alloys normally was achieved when a critical dispersion of GP zones, or an intermediate precipitate, or a combination of both were presented. Fig. 2.10 indicated the relation between yield strengths and precipitate type formation for an Al-Zn-Mg alloy and an Al-Zn-Mg-Cu alloy after solution treatment at temperature of 470 $^{\circ}$C for 30 minutes, quenched in water, and aging at 2 h for various temperatures. Al-2.4Zn-2.14Mg-0.5Cu

alloy obtained the highest yield strength at which a combination of GP zones and intermediate precipitate η' phase predominant. For Al-2.4Zn-2.14Mg, only GP zones responded to the first strengthening stage giving lower yield strength than Al-2.4Zn-2.14Mg-0.5Cu alloy [35].

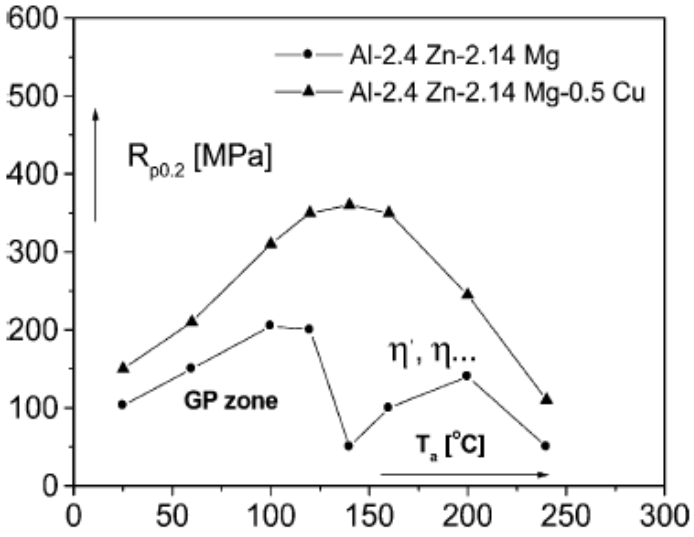

Fig. 2.10 Yield strength dependence of various aging temperatures at 2h [36].

2.3 Creep property

The continuity plasticity deformation of materials with time-dependence under a fixed stress or load at an elevated temperature is called in term of "creep". A variation of strains under creep test conditions is recorded and displayed as creep curve in Fig 2.11. Several aspects of the curve are classified to three regions stage: stage I or primary creep, stage II or secondary creep, and stage III or tertiary creep. For the primary creep, the strains increase immediately after loading, consequently the creep rate (plastic strain-rate) is generally decreasing with increasing plastic strains or times. The creep rate variation is less or constant where is in the secondary creep. Minimum creep rate, or secondary creep rate, or steady state creep rate is used to be parameters for designing and accessing creep life of materials. The creep rate rapidly increases during the tertiary stage, eventually leads to rupture or fracture.

Steady state creep rate ($\dot{\varepsilon}_s$) or minimum creep rate ($\dot{\varepsilon}_m$) varies with temperatures (T) and stresses (σ), including materials. Power's law equation is use to describe the relation of those variables as followed [25];

$$\dot{\varepsilon}_s = A\sigma^n \exp(-Q_c / RT) \qquad (2.1)$$

Where A is the constant, depending on microstructures

R is the gas constant(8.314 J/mol.K)

Q_c is the activation energy for creep

n is the stress exponent

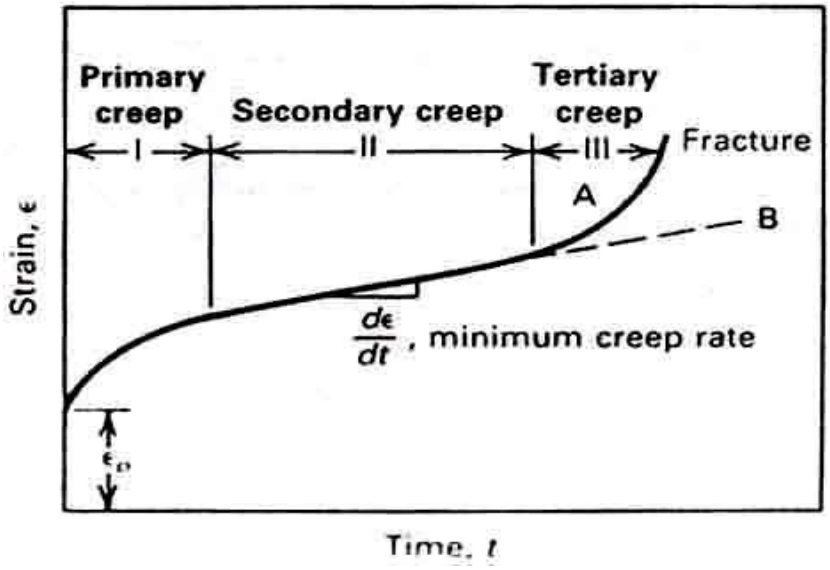

Fig. 2.11 Creep curve.

The temperature dependence of the secondary creep

Increasing temperatures ($T_1>T_2>T_3>T_4$) at a constant stress obtained the different creep curves as shown in Fig. 2.12. Secondary creep rate and creep life occurs faster at higher temperatures.

At a constant stress, the temperatures have influenced on the secondary creep rate as Arrhenius's law equation.

$$\dot{\varepsilon}_s = A\exp(-Q_c / RT) \qquad (2.2)$$

Where A is a constant depending on stresses and materials. When secondary creep rates ($\dot{\varepsilon}_s$) were plotted with reciprocal temperatures in Kelvin (1/T) in a semi-log scale, the activation energy for creep could be calculated from the slope of the graph as shown in Fig 2.13.

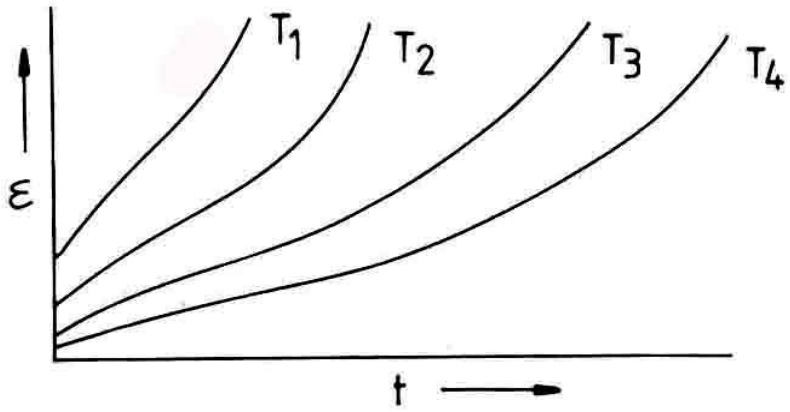

Fig. 2.12 Creep curves at various temperatures ($T_1 > T_2 > T_3 > T_4$) and a constant stress.

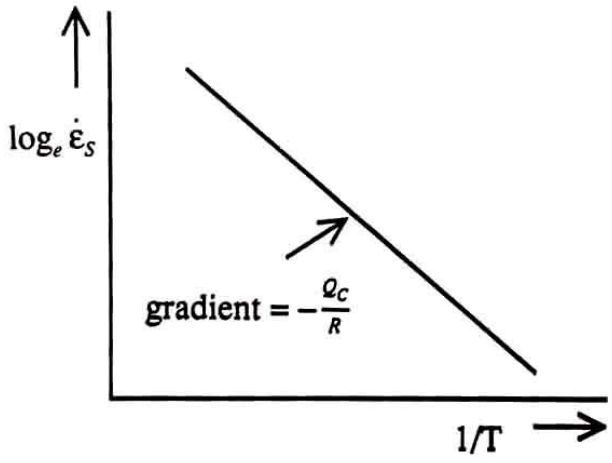

Fig. 2.13 Plotting between the steady state creep rates or minimum creep rates and temperatures for determining the activation energy.

The stress dependence of the secondary creep

At a constant temperature, the secondary creep rate depends on the stresses which power law creep equation could be explain in the simple form of Norton' equation.

$$\dot{\varepsilon}_{ss} = B\sigma^n \tag{2.3}$$

When B is temperature-dependent material parameter. The secondary creep rates increase with increasing the stresses and creep curves vary with the stress as shown in Fig. 2.14.

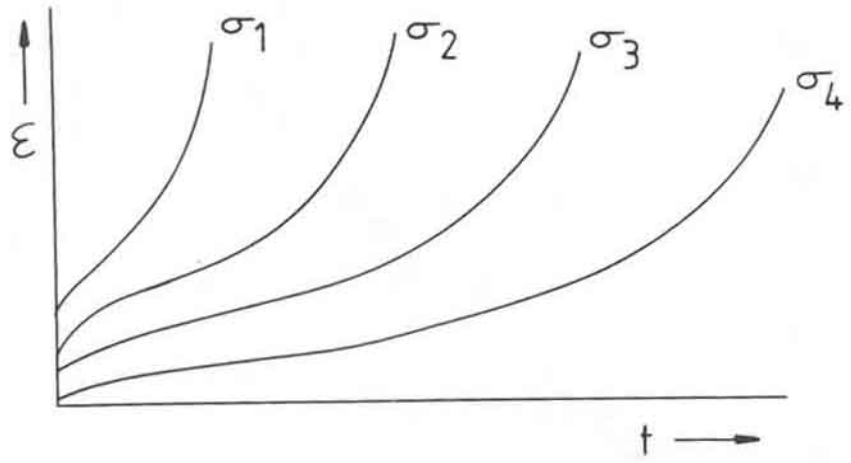

Fig. 2.14 Creep curves of various stresses ($\sigma_1 > \sigma_2 > \sigma_3 > \sigma_4$) and a constant temperature.

Plotting between the secondary creep rates and the stresses in the log-log scale, the stress exponent n could be calculated from the slope of the straight line as shown in Fig. 2.15.

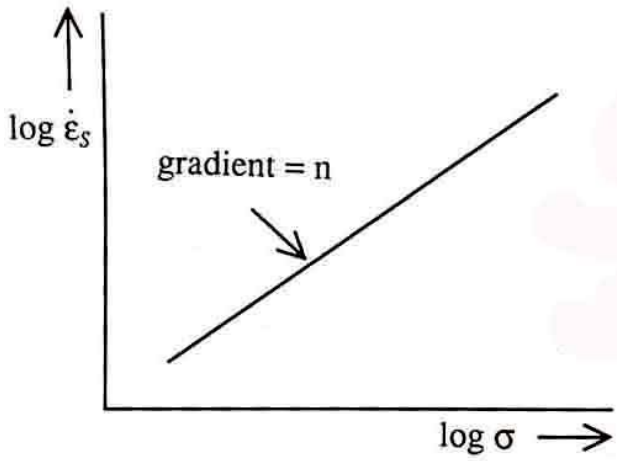

Fig. 2.15 Plotting between the steady state creep rates or minimum creep rates and stresses for determining the stress exponent.

The stress exponents varied with the applied stresses as revealed in Fig. 2.16. The stress exponents could be used to predict mechanisms controlled creep deformations. At low stresses, the stress exponent of *n* is 1 which creep deformation is controlled by diffusion creep. The ranging stress exponents of 4-6 at high stresses were referred to dislocation creep mechanism controlled. The power low breakdown theory described the creep deformation at very high stresses.

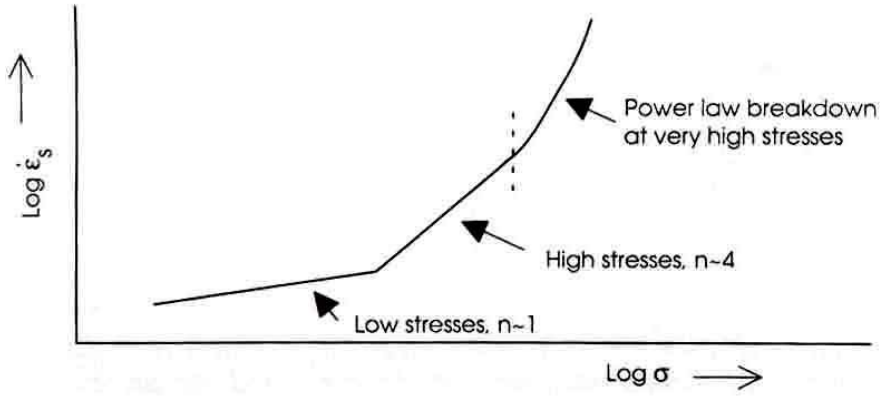

Fig 2.16 Plotting between $log\,\dot{\varepsilon}_{ss}$ and $log\sigma$.

2.3.1 Creep behavior of precipitate- hardening alloys

It is well known that precipitates lead to increase the strength of precipitate-hardening alloys for low temperature applications. The increased strength has been widely proposed to be the required strength for dislocation movement through the coherence precipitates. Orowan stress is determined to be the stress requirement for dislocation motions passed the precipitates by Orowan loop mechanism. Yield strength at low temperature is likely to be Orowan stress [46].

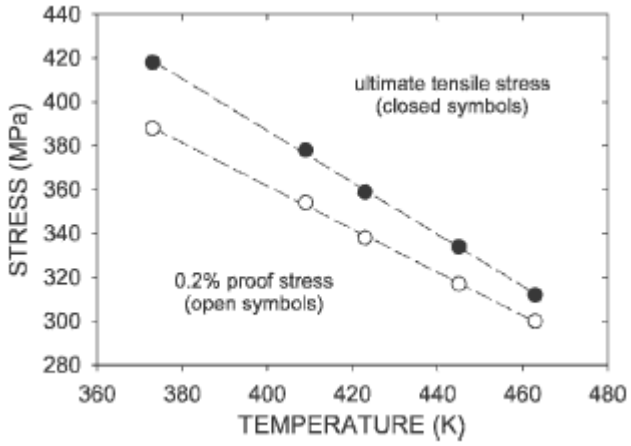

Fig. 2.17 The temperature dependences of the yield strength (0.2 pct proof stress) and the UTS for 7010 Al alloy [26].

However, yield strength decrease at elevated temperature, as shown in Fig. 2.17. It could be seen that yield strength of the 7010 Al alloy depends on the temperature, while it is strengthening by Orowan bowing. It is generally assumed that bowing process did not activated by thermal. However, dislocations can across particles or precipitates with no shear by climbing. Therefore, the stress at elevated temperatures requires only a partly stress of Orowan bowing. The required stress in precipitate hardening alloys usually determines in the term of threshold stress (σ_{TH}). It was found that the threshold stress of Al-Sc-Gd and Al-Sc-Yb alloys with obtaining coherence precipitates is high because of elastic interaction between coherence precipitates and climbing dislocations. In contrast, the threshold stress of those alloys with obtaining large size precipitate decreased because the precipitate density number decreased and free spacing precipitate increased [47]. The precipitates are the obstacles of dislocation motions. When applied stress is lower than threshold stress, creep deformation could not be measured. Therefore, power's law equation for precipitate hardening alloy demonstrates in the form as followed;

$$\dot{\varepsilon}_{ss} = A(\sigma - \sigma_{th})^n \exp\left(-\frac{Q_c}{RT}\right) \tag{2.4}$$

The threshold stress could be determined from the graph plotting between the steady stage creep rate or minimum creep rate and the stress, the trend solid lines were back extrapolate subsequently meet the stress axis which the stress value at the intercept is the

threshold stress as shown in Fig. 2.18. This figure revealed that Al-Sc-Gd alloys obtained the precipitate size of 2.4, 3.6, and 19.7 nm reached the threshold stress of 28, 36, and 24 MPa, respectively.

On the other hand, it could be determined as an followed equation [48].

$$\sigma_{th} = (1 - V_l)\sigma_{OR} \tag{2.5}$$

Where V_l is the volume fraction of precipitates and σ_{OR} is the orowan stress which derived from an equation as followed;

$$\sigma_{OR} = a\frac{Gb}{\pi\lambda}\ln\frac{d}{4b} \tag{2.6}$$

Where a is a constant depending on active slip systems, G is a shear modulus of matrixs, b is a burger vector, d is a diameter of precipitates, and λ is free spacing precipitates.

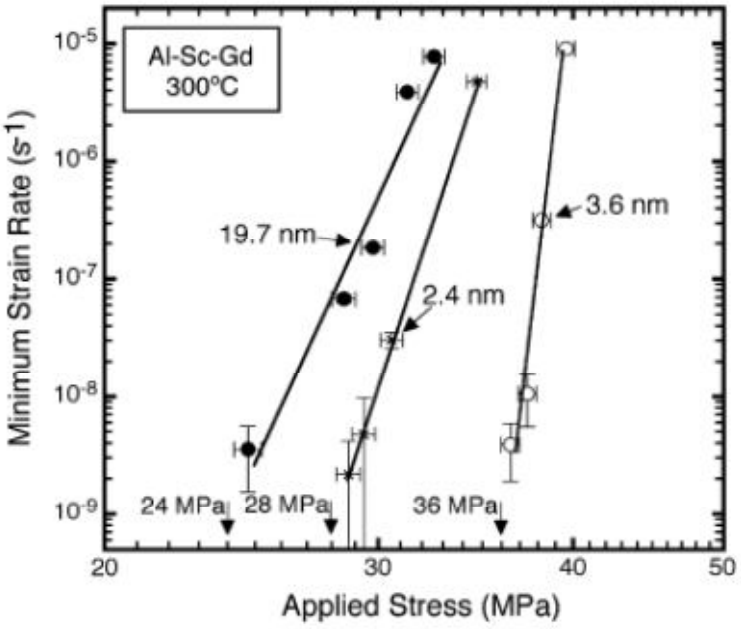

Fig. 2.18 Minimum strain rate vs applied stress for Al–Sc–Gd alloy at 300 °C and threshold stresses are marked on the stress axis [47].

2.3.2 Creep rupture

Creep rupture in uniaxial tension under constant stress has been described by the Monkman–Grant relationship, which states that the rupture of creep-deforming materials is controlled by the steady-state creep-rate, $\dot{\varepsilon}_{ss}$, equation (2.7),

$$\dot{\varepsilon}_{ss}^{m} t_f = k_{MG} \tag{2.7}$$

where k_{MG} is sometimes referred to as the Monkman–Grant constant and m is a constant typically about 1.0. Some data that illustrates the basis for this phenomenological relationship is in Fig.2.19. Although not extensively validated over the past 20 years, it has been shown to be valid for creep of dispersion-strengthened cast aluminum where cavities nucleate at particles and not located at grain boundaries [49].

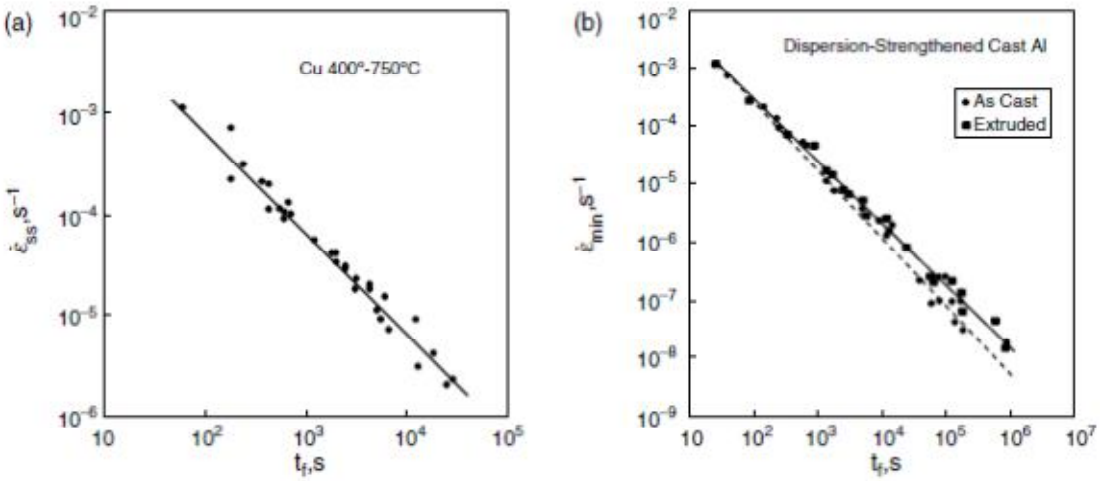

Fig. 2.19. (a) The steady-state creep-rate (strain-rate) versus time-to-rupture for Cu deformed over a range of temperatures (b) dispersion-strengthened cast aluminum [49].

Creep rate in the ternary creep stage is accelerated continuity, eventually creep rupture meet. It has been proposed that creep rupture caused by cavity. Mostly, cavity is initiated at the triple junction of grain boundary which is called as wedge type cavity as illustrated in Fig. 2.20(a). It is easily initiated at high stresses (low temperatures) and large grain sizes, when grain boundary sliding is not accommodated. Some have suggested that the wedge type cracks nucleate as a consequence of grain boundary sliding. Another mode of fracture has been associated with r-

type irregularities or cavities illustrated in Fig. 2.21. The wedges may be brittle in origin or simply an accumulation of r-types voids, as shown in Fig.2.20 (b).

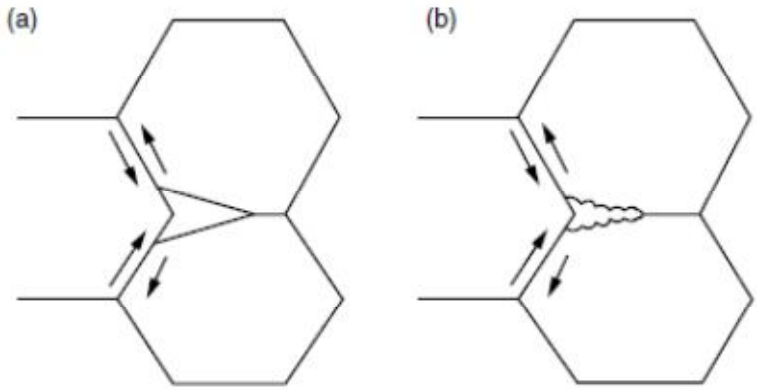

Fig.2.20 (a) Wedge (or w-type) crack formed at the triple junctions in association with grain-boundary sliding. (b) a wedge crack as an accumulation of spherical cavities [49].

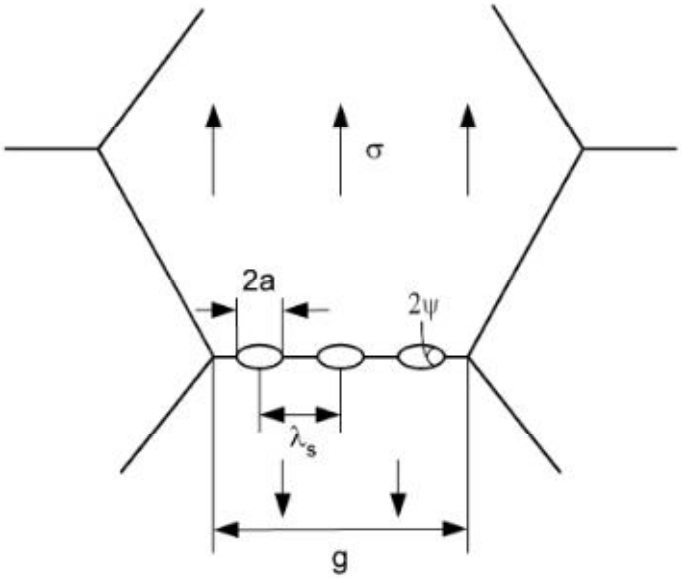

Fig. 2.21 Cavitation (r-type) or voids at a transverse grain boundary [49].

CHAPTER 3

RESEARCH METHODOLOGY

This chapter will present details of research methodologies which explain into the materials, heat treatment, tensile test, creep test, and microstructure characterization. The sample preparations for optical microscope, scanning electron microscope (SEM), and transmission electron microscope (TEM) examination will also explain. These details contain in four mainly topics. One will start from the topic of material applied in this research, semi-solid cast 7075 Al alloy. Afterward, the topic of the influence of solution heat treatment temperatures and times on microstructure, hardness, and tensile strength of the alloy will be explicated. The topic of the influence of artificial aging temperatures and times on microstructures, hardness, and tensile strength of the alloy will be explained later. Another topic is the details of the influence of T6 heat treatment on creep rupture behavior of the alloy studies.

3.1 Materials

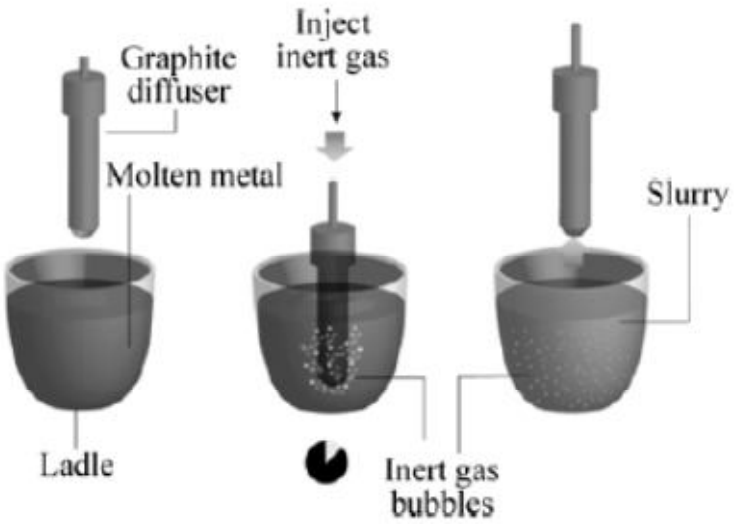

Fig. 3.1 Schematic of the GISS process [50]

The material used in this study was semi-solid cast 7075 Al alloy produced by the GISS process. Schematic of the GISS process is shown in Fig. 3.1. In this process, the alloy

ingots were melted in a graphite crucible using an electric resistance furnace. The melt was fluxed at 700 °C before casting. About 500 g of the molten alloy was taken out from the furnace using a ladle cup. A graphite diffuser was immersed in the liquid alloy at the rheocasting temperature of 643°C for 7 seconds and holding it for 30 seconds to produce a semi-solid slurry . The slurry was then poured into a die cavity, which was preheated to 280-300°C. A squeeze cast was subsequently applied at a pressure of approximately 80 MPa. Afterward, the as-cast plate was took off from the die and left it in ambient air for cooling down temperature.

The as-cast dimension plates were 100x100x15 mm. An as-cast 7075 Al alloy plate was sectioned into small 12 plates with dimension of 15x15x50 mm for heat treatment, hardness test, and microstructure examination as shown in Fig. 3.2(a) and (b). For tensile and creep specimens, An as-cast alloy plate was sectioned into small 6 plates with dimension of 15x15x100 mm as shown in Fig. 3.2(c).

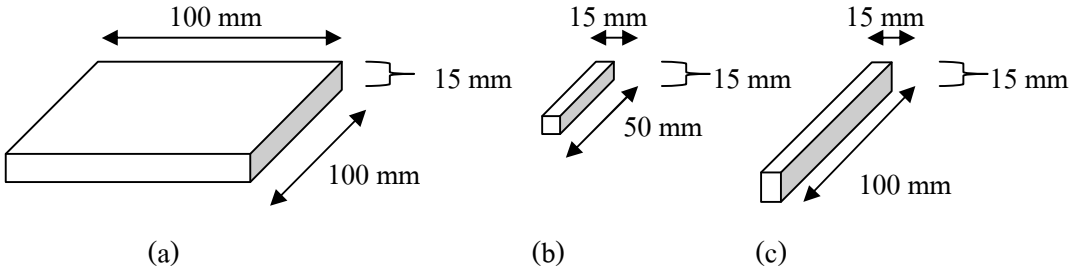

Fig. 3.2 (a) An as-cast 7075 Al alloy plate (b) shape and dimension of specimen for heat treatment, hardness test, and microstructure examination (c) specimen was sectioned for tensile test and creep test.

3.1.1 The chemical compositions and compounds

The as-cast plate was cut to square plate of 2.54x2.54 mm for a chemical composition analysis. The chemical composition of as-cast alloy was examined by Optical Emission Spectrometer (OES) and show in the table 3.1.

Table 3.1 The chemical composition of semi-solid cast of 7075 Al alloy produced by GISS technique.

Elements	Zn	Mg	Cu	Fe	Si	Cr	Al
%wt	6.08	2.50	1.93	0.46	0.4	0.19	Bal.

A phase formation in microstructure of the semi-solid cast 7075 Al alloy produced by GISS after the solidification stage was characterized by X-ray diffraction (XRD)

3.1.2 Microstructure examined by optical microscope and scanning electron microscope

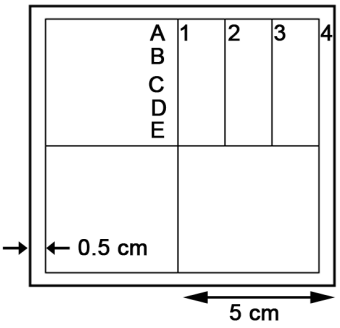

Fig. 3.3 Positions in as cast plates for microstructure examinations.

The as-cast plates were cut the rim out of 5mm (0.5 cm). The microstructure of as-cast alloy is examined in a quarter of plate from selected two plates. Each quarter plate was sectioned into 3 pieces with dimension of 15 x 15 x 50 mm. Cross section microstructures explore along the surface of 1 and 2 for first two pieces, and the surface of 3 and 4 for the third piece as presented in Fig. 3.3. The microstructure of each surface is investigated into 5 positions of A, B, C, D, and E as shown in Fig. 3.3. Each piece with dimension of 15 x 15 x 50 mm is cut into 5 cubic specimens for 5 microstructure examination positions. Cubic specimens are cold mounted with rasin, then are polished by using SiC sand papers from 320, 600, 800, and 1,200 grit and followed by 5, 1, and 0.3 μm micro-polishing alumina powder, respectively. The last step, the samples are etched with 0.5%HF reagent for up to 5 seconds before rinsing by distilled water. Afterward, the microstructures of all samples are examined by optical microscope and scanning electron microscope.

3.2 Influence of solution heat treatment temperatures and times on microstructure, hardness, and tensile strength of the semi-solid cast 7075 Al alloy

3.2.1 Solution heat treatment

The as-cast specimens were solution treated at either temperatures of 450° C or 480 °C for 1, 4, 8, and 12 h and subsequently quenched in water at temperature of 25°C. Three specimens were supplied to each condition of solution heat treatment for microstructure analysis, hardness test, and tensile test.

3.2.2 Microstructure examined by optical microscope(OM) and scanning electron microscope(SEM)

Three solution heat treated specimens with dimension of 15 x 15 x 50 mm. for each solution heat treatment condition cut into cubic shape specimen with dimension of 15 x 15 x 15 mm. All cubic specimens were cold mounted by the resin. They were then polished by using SiC sand papers from 320, 600, 800, and 1,200 grit and followed by 5, 1, and 0.3 μm micro-polishing alumina powder, respectively. The last step, the specimens were etched with 0.5%HF reagent for up to 5 seconds before rinsing by distilled water. Afterward, the microstructures of all samples were examined by optical microscope and scanning electron microscope couple with Energy Dispersive Spectroscopy (EDS).

3.2.3 Quantitative analysis of Microstructures

The area fraction of remaining grain boundary phases, Al-Fe-Cu, Mg_2Si, and coarse black particles were analyzed by optical micrographs with magnification of 20x along with photo shop and image tool program. The numbers of analyzed micrographs were approximately 20-30 micrographs for a solution heat treatment condition. Al-Fe-Cu and Mg_2Si phases were quantified by the difference in color contrast. Mg_2Si phases and coarse black

particles could be separated by the shape and size. The fist step painted the counting phase with the red colors by using a photo shop program as shown in Fig. 3.4(a)-(b).

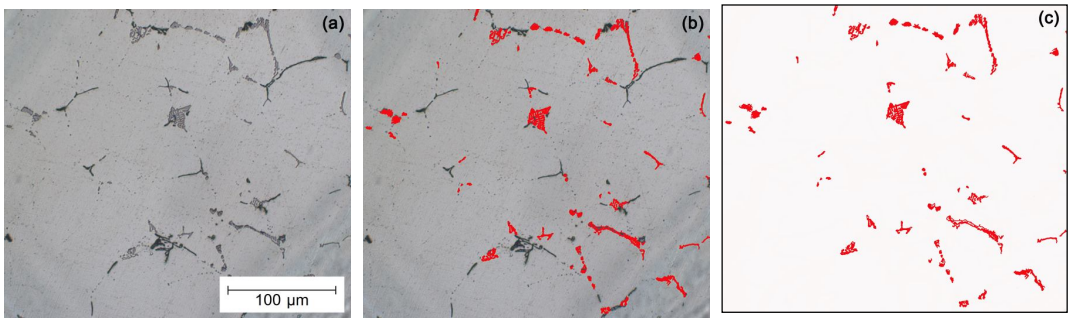

Fig. 3.4 Represent micrographs for determining the area fraction of phases (a) before painting (b) painted the Al-Fe-Cu phases (gray contrast color) with red color (c) conversed other areas to be white color areas.

Afterward, other areas were conversed to be white area counted by an image tool program as shown in Fig 3.4(c). The area fraction of each phase could be calculated as followed.

The area fraction of phase A = Area of phases A / Total Area (3.1)

3.2.4 The influence of solution heat treatment condition on artificial aging

The as cast specimen with dimension of 15 x 15 x 50 mm were solution treated at either temperatures of 450° C or 480 °C for 1, 4, 8, and 12 h and subsequently quenched in water at temperature of 25°C. All as-quench specimen of each solution heat treatment condition were artificial aged at 120°C for 12 h. Three specimens were solution heat treated for a condition. The hardness test was applied for the primary evaluation property.

3.2.5 Hardness Test

Both surfaces side of as cast specimens and specimens passed the process in the topic 3.2.4 were polished with 180 grit SiC sand paper for flatten. The specimens were then tested the hardness of Rockwell scale B followed as ASTM E18-03[51]. A specimen with dimension of 15 x 15 x 50 mm was indented five points for a side which the hardness value for one solution heat treatment condition was averaged from three specimens with 30 indented points.

3.2.6 Tensile Test

3.2.6.1 Tensile Specimen

As cast specimens and some solution heat treated specimens were tensile tested. Tensile specimens were dumbbell shape as shown in Fig. 3.5. The dimension of specimen followed as ASTM B 557M-02a [52] in table 3.2 according to specific variables in Fig 3.5. In thesis, the tensile specimens applied the small-size specimens proportional to standard with diameter of 5 mm, gauge length of 25 mm, and threaded-end specimen of M10 x1.50 as shown in Fig 3.6.

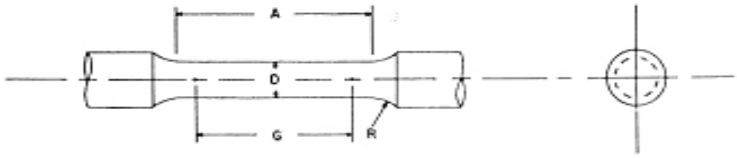

Fig. 3.5 Tensile specimen with specific variables of specimen dimension.

Table 3.2 Examples of small-size specimens proportional to the standard specimen.

	Dimensions, mm			
Nominal Diameter	Standard Specimen	Small-Size Specimens Proportional to Standard		
	12.5	9	6	4
G-Gage Length	62.50±0.10	45.00±0.09	30.00±0.06	20.00±0.04
D-Diameter (Note 1)	12.50±0.25	9.00±0.10	6.00±0.10	4.00±0.05
R-Radius of fillet,min	9	8	6	4

A-Length of Reduced Section,min (Note 2)	75	54	36	24

Fig. 3.6 Tensile specimen.

3.2.6.2 Tensile test machine and variable for tensile test

The tensile test machine was HOUNSFIELD TEST EQUIPMENT Model H 100ks Serial No. 0068. The tensile test was operated at crosshead speed of 1.5 mm/min or strain rate of 1×10^{-3}.

3.3 Influence of artificial aging temperatures and times on microstructures, hardness, and tensile strength of the semi-solid cast 7075 Al alloy

3.3.1 Artificial Aging

The as cast specimen with dimension of 15 x 15 x 50 mm were solution treated at optimum solution heat treatment condition derived from the topic 3.2 and subsequently quenched in water at temperature of 25°C. As-quenched specimens were aged at different temperature of 120 $^{\circ}$C, 145 $^{\circ}$C, 165 $^{\circ}$C, and 185 $^{\circ}$C for various time conditions from 20 minutes to 132 hours, then quenched in water at room temperature.

3.3.2 Hardness Test

Both surfaces sides of aged specimens passed the aging process in the topic 3.3.1 were polished with 180 grit SiC sand paper for flatten. The specimens were then tested the

hardness of Rockwell scale B followed as ASTM E18-03[51]. A specimen with dimension of 15 x 15 x 50 mm was indented five points for a side which the hardness value of one solution heat treatment condition was averaged from three specimens with 30 indented points.

3.3.3 Tensile Test

As-cast specimens with dimension of 15 x 15 x 50 mm were passed the aging conditions at peak hardness times for each aging temperature, including under-aged condition at 120°C for 24 h and over-aged condition at 180°C for 12 h . Afterward, the specimens were then machined to dumbbell shape with the dimension followed as the topic 3.2.6.1. The tensile test machine and operating variables followed the topic 3.2.6.2.

3.3.4 Microstructure characterization

The microstructure of T6-aged specimen was characterized by a JEM-2010 JEOL transmission electron microscopy (TEM). In order to prepare TEM specimens, a heat treated plate with the size of 15 mm×15 mm×50 mm was machined to a 3 mm diameter rod. This rod was then sliced into about 0.8 mm thick discs by using a low speed diamond saw. Both sides of the discs were mechanically polished to about 40–60 μm thickness with the 1200 grit SiC sand paper and 5 μm micro-polishing alumina powder. The specimen was then electro-polished on a Tenupol-3 electropolisher with a solution of 20–25 vol% nitric acid and 80–75 vol% methanol at -15 ˚C to -20 ˚C and an applied current of 1.2–1.5 A.

3.4 Influence of T6 heat treatment on creep rupture behavior of semi-solid cast 7075 Al alloy at the temperature of 200°C and the stresses of 120 MPa – 180 MPa

The creep rupture behavior of a semi-solid cast 7075-T6 Al alloy produced by GISS technique was investigated in comparison with a commercial wrought 7075-T651 Al alloy. A square plate dimension of the as- semi solid cast 7075 Al alloy was 100x100x15 mm. They were cut to small square plates to the dimension of 15x100x15 mm for T6 heat treatment. The

samples were solution heat treated at temperature of 450°C for 4 h, quenched in 25°C water, then artificially aged at temperature of 120°C for 72 h. These samples were then called the semi-solid cast 7075-T6 Al alloy. The commercial 7075 Al alloy with passed the rolling and thickness of 12.7 mm(ALUSA HA75-A Lot No. E04913) was produced in Switzerland and bought through the dealer company, NASA METALS CO. LTD. The chemical composition of the commercial 7075 Al alloy reveals in the table 3.3.

Table 3.3 The chemical composition of the commercial wrought 7075-T651 Al alloy.

Elements	Zn	Mg	Cu	Fe	Si	Cr	Al
%wt	5.92	2.64	1.70	0.19	0.07	0.19	Bal.

3.4.1 Creep specimens

The creep specimens of both alloys were machined in dumbbell shape followed as the topic of 3.2.6.1

3.4.2 Creep machine

All creep tests were performed in a custom-built lever-beam type test equipment as developed by Zhou [53]. Fig. 3.7 shows the creep machine which composes of (1) structure frame (2) furnace (3) weight loads (4) LVDT (Linear Variable Displacement Transducer) holder accessories (5) storage data instrument.

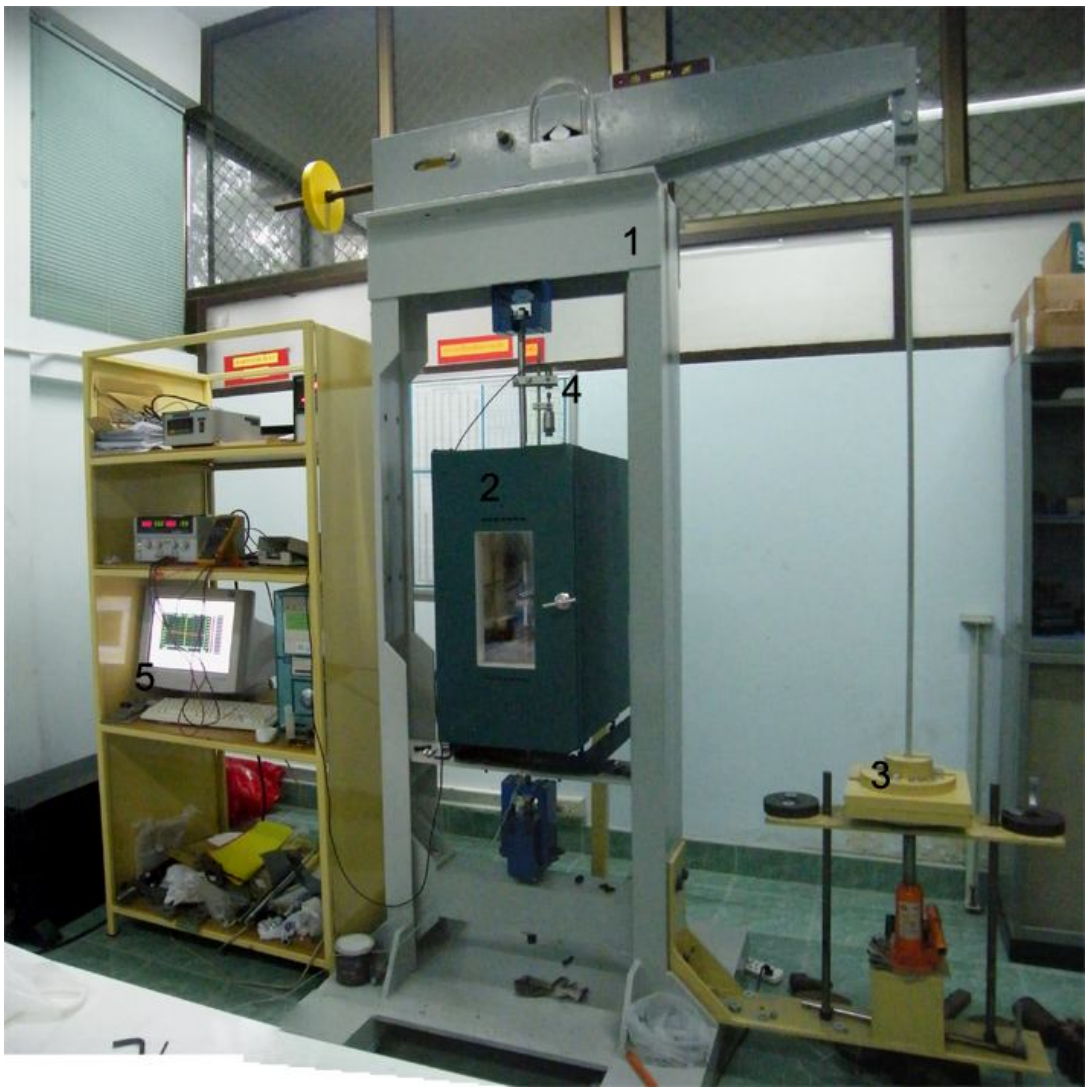

Fig. 3.7 Creep machine

3.4.3 Specimen holder and LVDT holder

A LVDT is an instrument for measuring the displacement of the specimen. The displacement measurement series were designed as shown in Fig. 3.8(a). The LVDT composed of a needle and a case obtained electromagnetic coils which have a hole through its. The LVDT needle placed on the tip of the micrometer which held with rectangular plate and fixed with the reference rod as shown in Fig. 3.8(b). The LVDT case was held with upper rectangular plate which fixed with pull rod as shown in Fig. 3.8(b). The reference rod could move through upper

rectangular plate. Another tip of reference rod fixed through a rectangular place connected with the specimen as shown in Fig. 3.8(c). When the specimen displaced during creep test, the reference rod also moved leading to a LVDT needle move freely through the hole of the LVDT case and then could generate the signals. The LVDT signals was transferred to collect in the computer by using the program of National Instruments Virtual Bench™ Version 2.6 500615D - 00. The micrometer used to readjust the position of a LVDT needle when the elongation of the specimen was nearly the length of a LVDT needle.

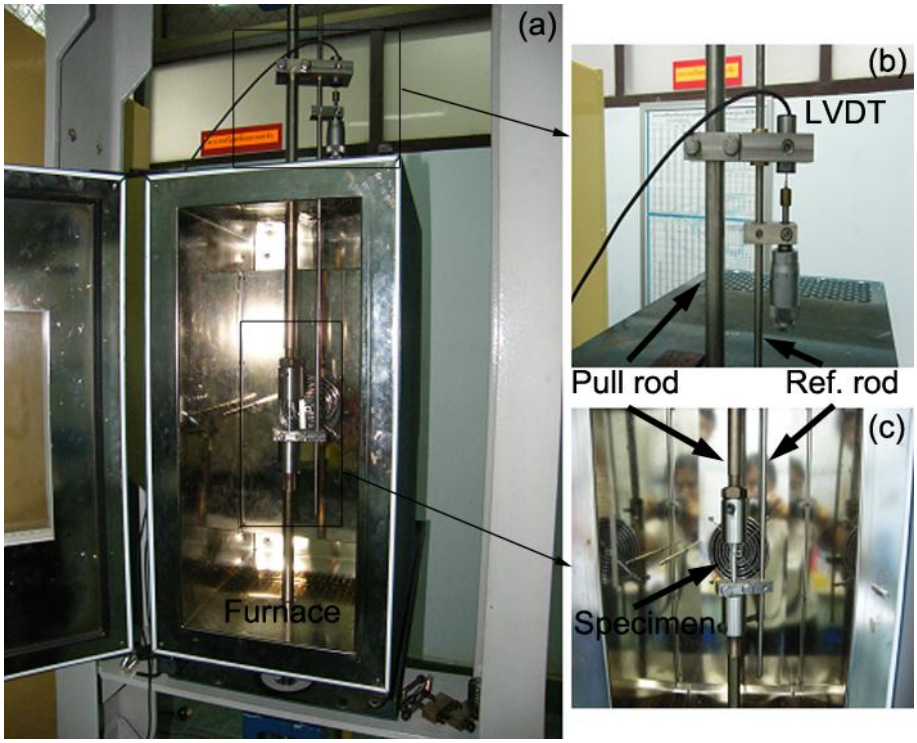

Fig. 3.8 (a) Displacement measurement series (b) LVDT accessories and connection (c) A specimen connection.

3.4.4 Load calibration

The real specimen load could be calibrated by a load cell. The ratio of specimen load and weight load was determined as the graph in Fig. 3.9 and the straight line was derives to equation (3.2).

$$y = 4.9604x + 1.8996 \quad (3.2)$$

y = the specimen load

x = the weight load

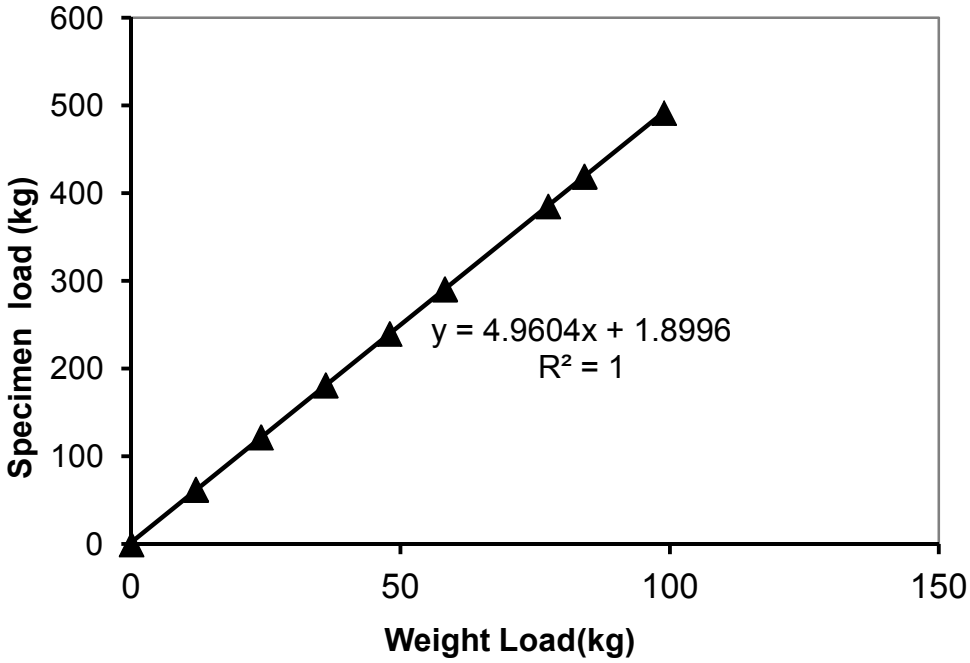

Fig. 3.9 Graph of load cell calibration.

3.4.5 Creep rupture test

The creep rupture test was performed in air under constant load condition at initially stress levels ranging from 120 to 180 MPa and a temperature of 200°C ±1°C. Prior to creep loading, the creep specimens were preheated from room temperature to 200°C for 1 h. The specimen temperature was sensed by a thermocouple attached to the centre of the gauge section and measured by a digital temperature meter to a precision of ±1 °C. The creep rupture test procedure followed as :

(1) Take the specimen to the holder and connect to the pull rod with the slungs.

(2) Connect the reference rod with the specimen and LVDT accessories.

(3) The square plates connecting with the specimen and LVDT accessories should be leveled. Turn on the power supply for inputting the voltage to LVDT.

(4) Turn on computer and open the collected data program.

(5) Take the hydrolic jack to support a load pan, next load the required weight to the load pan, and then turn the the hydrolic jack for adjusting the balance of the lever-beam.

(6) Turn on the furnace and heat up from room temperature to 200°C for 1 h.

(7) Release the hydrolic jack for taking the loads to the specimen.

(8) When the specimen rupture, quench it in the room temperature water immediately.

3.4.6 Microstructure characterization

3.4.6.1 Microstructure characterized by OM and SEM

Microstructures of both alloys before creep test were characterized by both an optical microscope (OM) and a scanning electron microscope (SEM) couple with energy dispersive spectroscopy (EDS). Both specimen alloys were cut into cubic shape specimen with dimension of 15 x 15 x 15 mm. All cubic specimens were cold mounted by the resin. They were then polished by using SiC sand papers from 320, 600, 800, and 1,200 grit and followed by 5, 1, and 0.3 μm micro-polishing alumina powder, respectively.

Cross-section microstructures of an area near the rupture surface were investigated by an optical microscope (OM) and a scanning electron microscope (SEM) couple with energy dispersive spectroscopy (EDS). Specimen preparations were started to cut crept specimens far away the tip of approximately 10 mm, then cold mounted them in horizontal direction with the resin. Afterward, they were polished by using 180 grit SiC sand papers until obtained the cross-section area, and were then polished continue from 320, 600, 800, and 1,200 grit and followed by 5, 1, and 0.3 μm micro-polishing alumina powder, respectively.

Fracture surfaces of specimens after creep test were examined by a scanning electron microscope (SEM) couple with energy dispersive spectroscopy (EDS). In order to specimen preparations, crept specimens were cut approximately 10 mm from a tip of rupture specimens. They were placed in vertical direction on the stab for SEM examining.

3.4.6.2 Microstructure characterized by TEM

Precipitates of preheated specimens before creep loading and crept specimens after creep loading at 200°C and 140 MPa for 5 h of both alloys were examined by TEM. The specimens were machined to a 3 mm diameter rod. This rod was then sliced into about 0.8 mm thick discs by using a low speed diamond saw. Both sides of the discs were mechanically polished to about 40–60 μm thickness with the 1200 grit SiC sand paper and 5 μm micro-polishing alumina powder. The specimen was then electro-polished on a Tenupol-3 electropolisher with a solution of 20–25 vol% nitric acid and 80–75 vol% methanol at -15 °C to -20 °C and an applied current of 1.2–1.5 A.

CHAPTER 4

RESULTS AND DISCUSSIONS

The objective of this research is to investigate the influence of T6 heat treatment process on the microstructure and mechanical properties of semi-solid cast 7075 Al alloy produced by GISS technique. Microstructures of an as-semi solid cast alloy were examined, which was illustrated and discussed in the first topic. Three topics of T6 heat treatment studies were explored. The first studies determined the optimum solution heat treatment condition for the alloy which focuses to the influence of solution heat treatment temperatures and times on microstructures, hardness, and tensile strength of the alloy. The next one explored the effect of aging temperatures and time on precipitates, hardness, and tensile strength for inquiring into the peak aged of the alloy. The last one, creep rupture behavior of the alloy passed the peak aged heat treatment condition was examined for seeking the possibility high temperature applications. In addition, the creep rupture test of commercial 7075 Al alloy also provide for a comparison with the semi-solid cast 7075 Al alloy. This chapter will report and discuss the all study results.

4.1 Microstructures of Semi-solid Cast 7075 Al Alloy

As semi solid cast 7075 Al alloy was produced by GISS with introducing gas bubble for 7 s and holding for 30 s before pouring to the mold, subsequently squeeze cast with pressure of 80 MPa. As-cast samples are a square plate with dimension of 100 mm x 100 mm x 10 mm. The sample is cut the rims of each side out for 0.5 mm and use only a quarter of each plate for examining cross section microstructures. The quarter of plate is sectioned into three pieces which one side of the fist two pieces from the center(as column 1 and 2) and both sides of the third piece(as colum 3 and 4) are represented the microstructures. Five positions of A, B, C, D, and E of each side are examined the microstructures from the top to the bottom as the diagram shown in Fig 4.1(a). A representation of the microstructures reveals in Fig 4.1(b). It could be seen that the microstructure of as semi solid cast 7075 Al alloy produced by GISS is non-dendritic and homogenous structure.

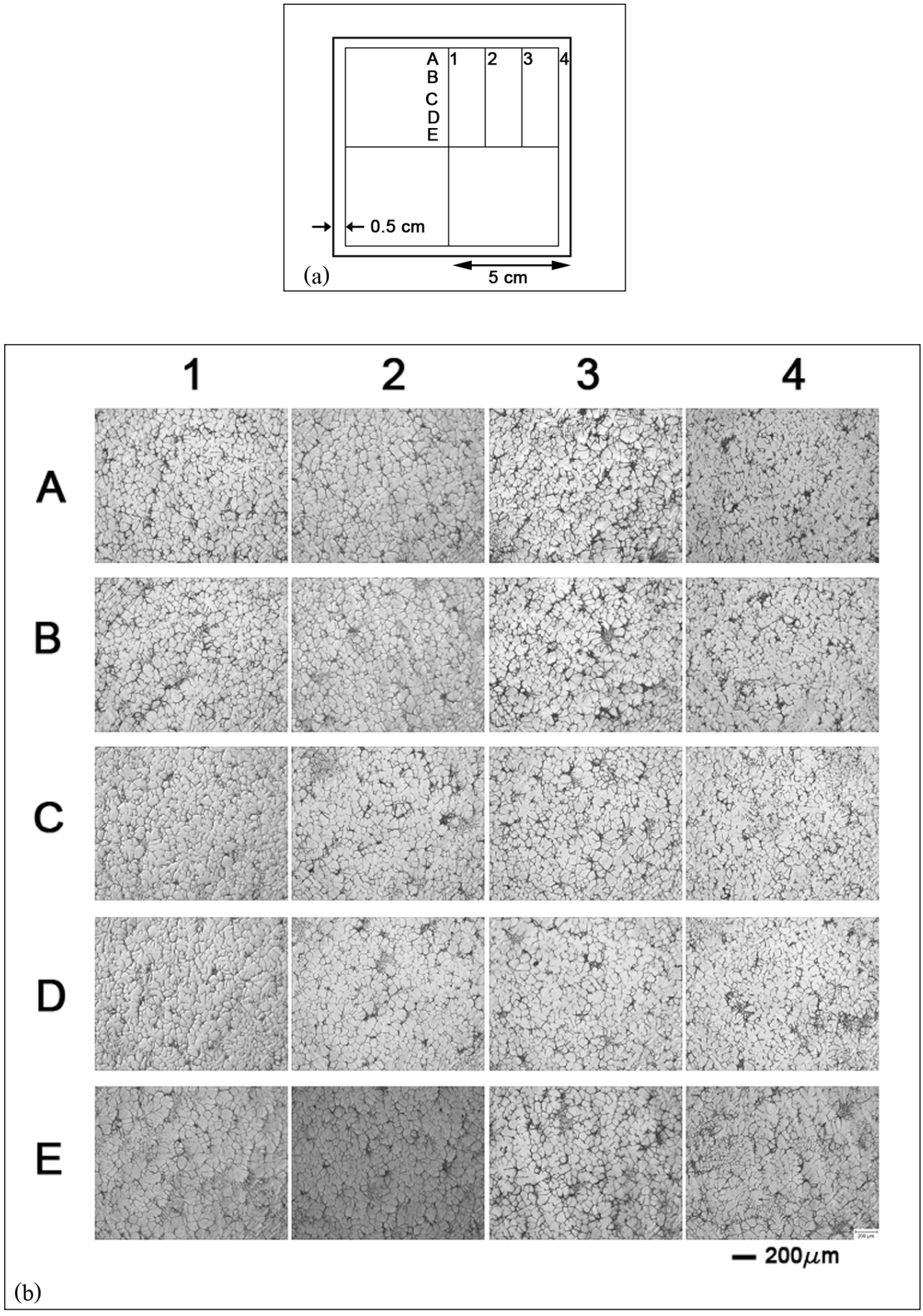

Fig. 4.1 (a) A diagram pointed out the positions for examining microstructures (b) optical micrographs of semi-solid cast 7075 Al alloy produced by GISS technique followed as the position in (a)

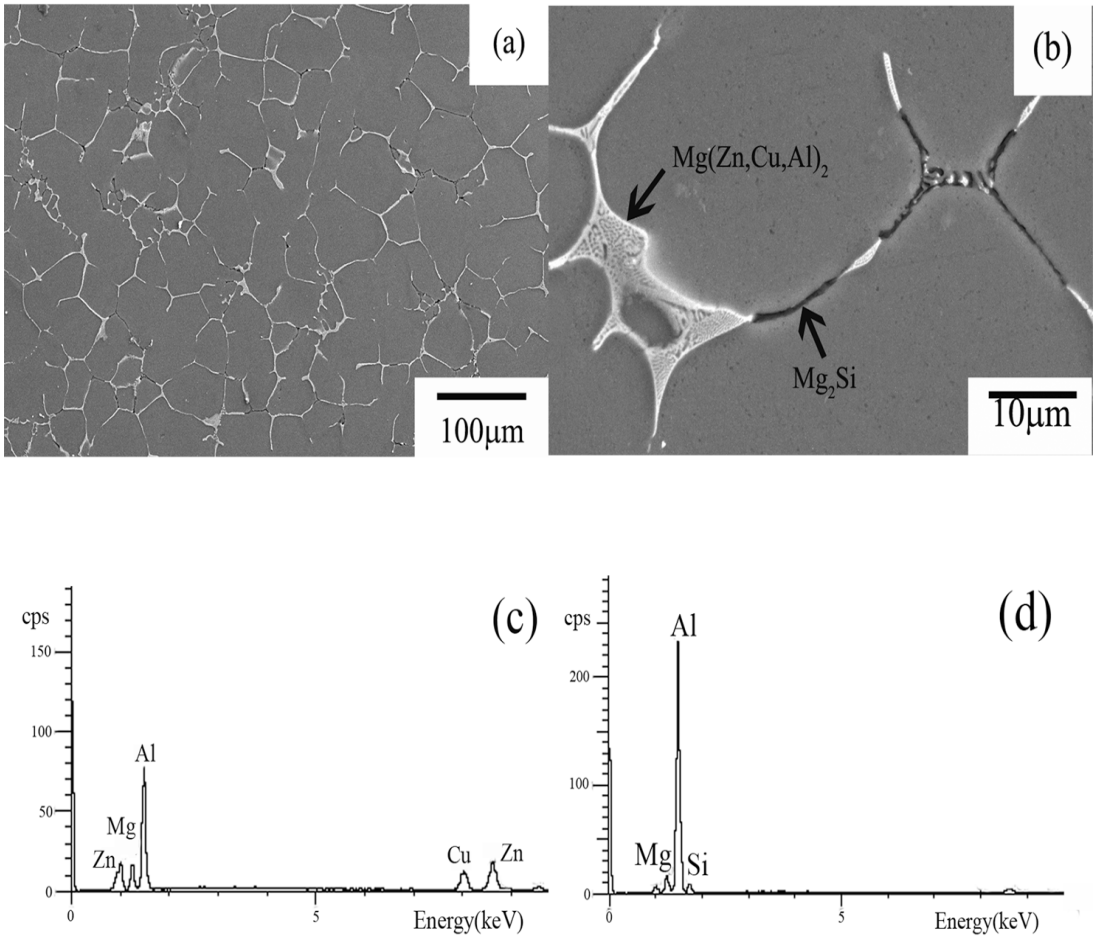

Fig. 4.2 SEM micrographs of (a)-(b) as-cast semi-solid 7075 Al alloy (c) EDS result of bright area and (d) EDS result of elongated black area.

Secondary electron images of as-cast microstructures reveal a non-dendritic grain structure and a white contrast of grain boundary (GB) phases as shown in Fig. 4.2(a). A high magnification image of GB phases in Fig.4.2(b) presents large bright areas and elongated black areas at grain boundaries of matrix-α (Al). The SEM-EDS point analysis of the bright areas at grain boundaries shows high concentrations of Zn, Mg, and Cu elements because of solute segregation during casting, as illustrated in Fig.4.2(c). One previous investigation [54] referred that if Zn/Mg ratio of Al-Zn-Mg-Cu alloy is more than 2.2, the dominant second phase in the solidification eutectic should be the $MgZn_2$ phase. In this research, Zn/Mg ratio of the alloy is 2.4. In addition, the XRD result of the as-cast specimens mainly consists of α-Al and η-$MgZn_2$ as shown in Fig. 4.3. Therefore, most of bright GB phases should be quaternary $Mg(Zn,Cu,Al)_2$

phase in that some Al and Cu atoms have dissolved in the η-phase and form the same crystallographic lattice constant as $MgZn_2$, as reported by Eivani et al [55]. The EDS result shown in Fig. 4.2(d) indicates that the elongated black area at the grain boundary in Fig. 4.2(b) is Mg_2Si phase. However, the existence of this small amount of Mg_2Si cannot be verified by the XRD test.

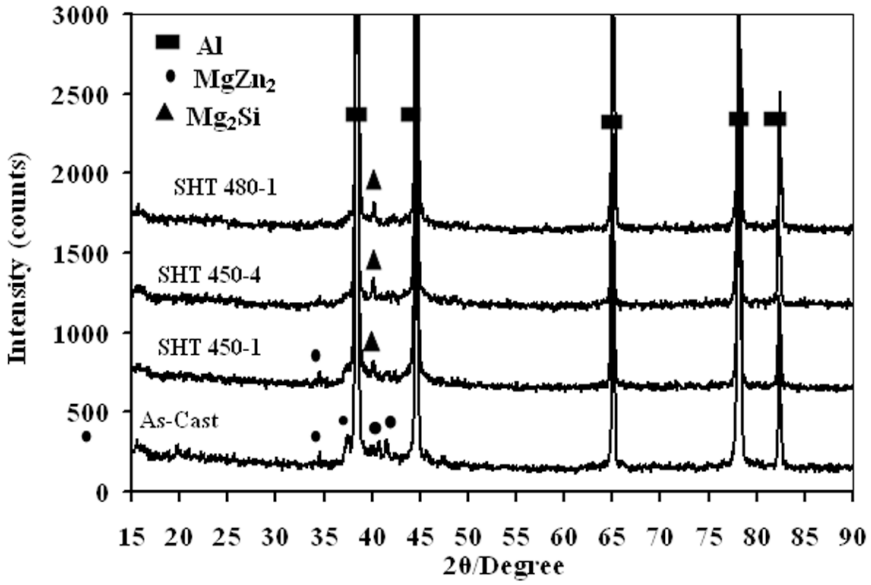

Fig. 4.3 XRD results of as-cast and solution heat treated (SHT) samples (SHT 450-1: 450 °C/1 h, SHT 450-4: 450 °C/4 h, SHT 480-1: 480 °C/1 h).

4.2 Effect of solution heat treatment on microstructure and mechanical properties

Grain boundary (GB) initially presents as a spatially continuous white contrast color, including minor amount of black line structure. The microstructure mainly consisted of matrix-α (Al) and grain boundary (GB)-eutectic phase (α-Al + η-$MgZn_2$). Predominantly, the observed phases at GBs of the as-cast Al–Zn–Mg–Cu alloy are η($MgZn_2$), T($Al2Mg_3Zn_3$) and S(Al_2CuMg) [56]-[58]. The Fe-rich phases and Mg_2Si also formed in the alloy containing Si and Fe impurities [59]. The evolutions of morphology and content of GBs depended strongly on solution heat treatment temperature and time, as shown in Fig. 4.4 and 4.5. The mechanism for evolution of GB phases during heat treatment has been proposed in three stages: thinning, discontinuation, and dissolution [55]. In this research, spatially continuous GB phases of as-cast

specimens were subsequently dissolved after solution heat treatment at either temperature. The discontinuation stage could be more notably observed than other stages. It evolved into isolated phases and decreased in content after SHT at either temperature of 450°C or 480°C. After 450 °C SHT for 1 h, the discontinuous GB phases were observed (Fig. 4.4(b) and 4.5(b)), while isolated GB phases were clearly observed in the specimens solution treated at 450°C longer than 4 h (Fig. 4.4(c)-(d) and 4.5(c)-(d)) and at 480°C-1 h (Fig. 4.4(e) and 4.5(e)).

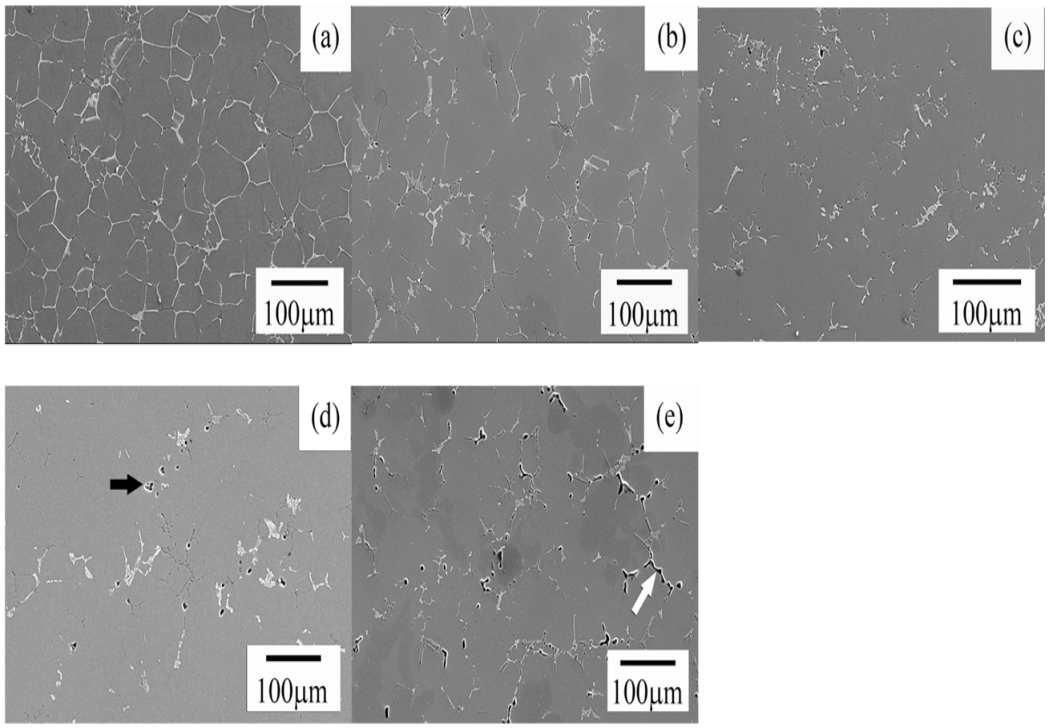

Fig. 4.4 SEM micrographs of GISS processing rheocast 7075 Al alloy (a) as-cast and as quenched after (b) SHT 450 °C/1h (c) 450 °C/4h (d) 450 °C/8h (e) 480 °C/1h specimens.

Area fractions of the remaining grain boundary phases in the solution treated samples were quantitatively analyzed from optical micrographs (the selected micrograph as shown in Fig. 4.5) and illustrated in Fig. 4.6. It is observed from Fig. 4.6 that the remaining GB phases sharply decreased in the first hour of solution treated temperatures at 450 °C and 480 °C. However, the area fraction of the GB phase in the sample solution treatment at 480 °C remained almost constant when the solution treatment time is longer than 1 h; indicating that this phase may be completely or almost dissolved within the first hour of solution treatment at 480 °C. This

result was confirmed by the XRD result showing the disappearance of η-$MgZn_2$ phase in Fig. 4.3. On the other hand, solution treating of the sample at 450 °C for 1 h was not enough to allow diffusion to establish an equilibrium solid solution since the major second phase of $Mg(Zn,Cu,Al)_2$ was not completely dissolved as indicated by XRD, OM and SEM-EDS results shown in Fig. 4.3, Fig. 4.5(b), and Fig. 4.8(a)-(b), respectively. Hence, the area fraction of the GB phase in the sample solution treated at 450 °C continued to decrease for further solution treating until complete dissolution was met at the solution treating time of 4 h leading to the disappearance of η-$MgZn_2$ phase in the XRD result as shown in Fig. 4.3.

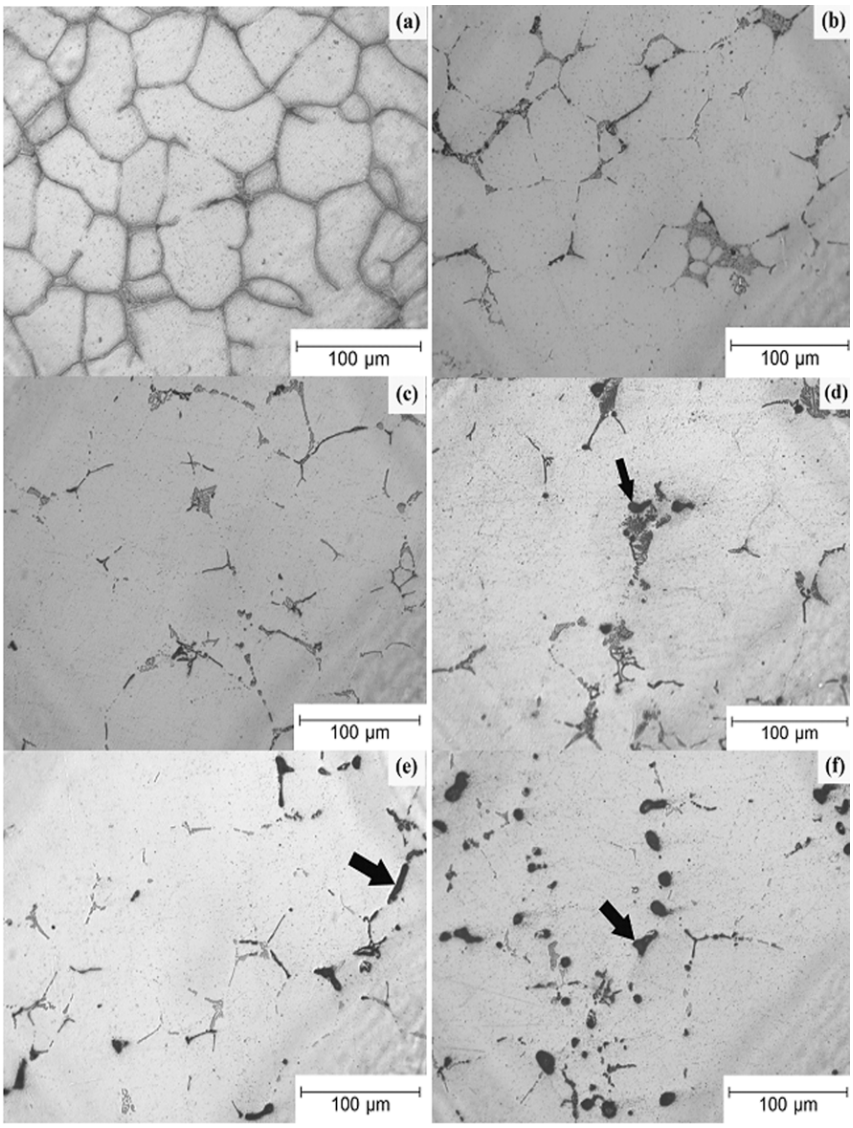

Fig. 4.5 Optical micrographs of (a) as-cast (b) SHT 450 °C/1h (c) SHT 450 °C/4h (d) SHT 450 °C/8h (e) SHT480 °C/1h, and (f) SHT 480 °C/8h specimens.

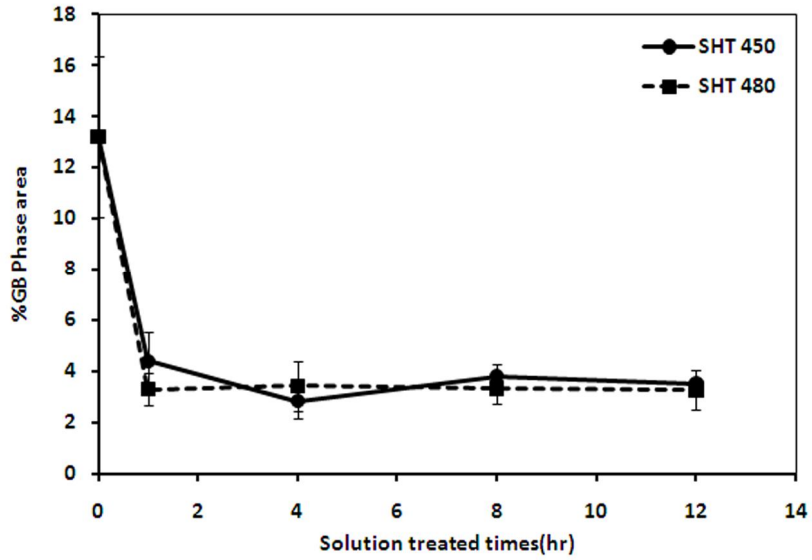

Fig. 4.6 Area fractions of GB phases after solution heat treatment at 450 °C and 480 °C at various holding times.

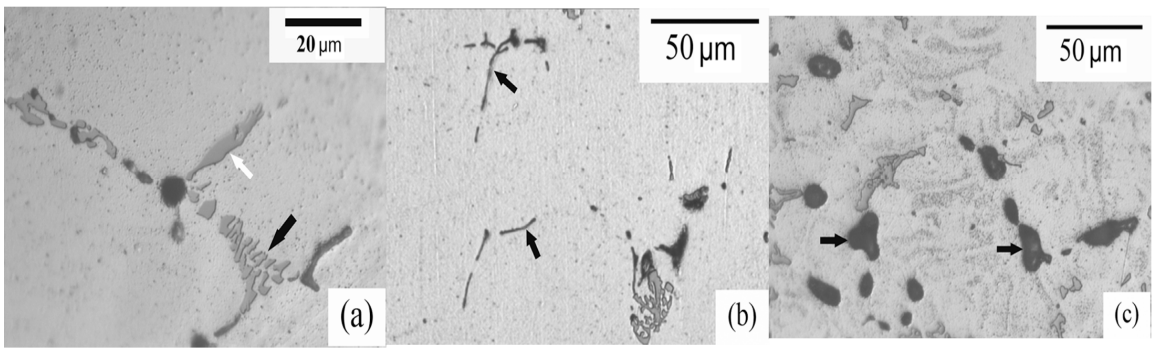

Fig. 4.7 Optical micrographs showing (a) skeleton and irregular shaped (b) black line shaped (c) coarse black particles in the SHT specimen, as indicated by arrows.

Optical micrographs in Fig. 4.7 revealed remaining grain boundary phases in two different color contrasts; gray and black. Most of the remaining phases at the first 4 h of 450°C-SHT showed gray contrast with the shapes of either a skeleton or an irregular shape, as pointed out by black and white arrows in Fig. 4.7(a), respectively. These microstructures were similar to those presented by Doroshenko et al. [60]. Dark and light gray skeleton phases were

identified as $(Cu,Fe)Al_6$ and Cu_2FeAl_7, respectively, while irregular-shaped particles were $(Cu,Fe)Al_6$. It is in agreement with the SEM micrograph and EDS result in fig 4.8(c) and 4.8(d). Black line phase observed in fig. 4.7(b) and 4.8(e) were the same phase which also identified as Mg_2Si in agreement with EDS result in fig. 4.8(f) appeared the high peak intensity of Mg and Si. In addition, coarse black particles were clearly observed in the 450°C-8 h, and 480°C-1 h or prolonged holding time SHT specimens, as indicated by arrows in Fig. 4.4(d)-(e), 4.5(d)-(f), and 4.7(c).

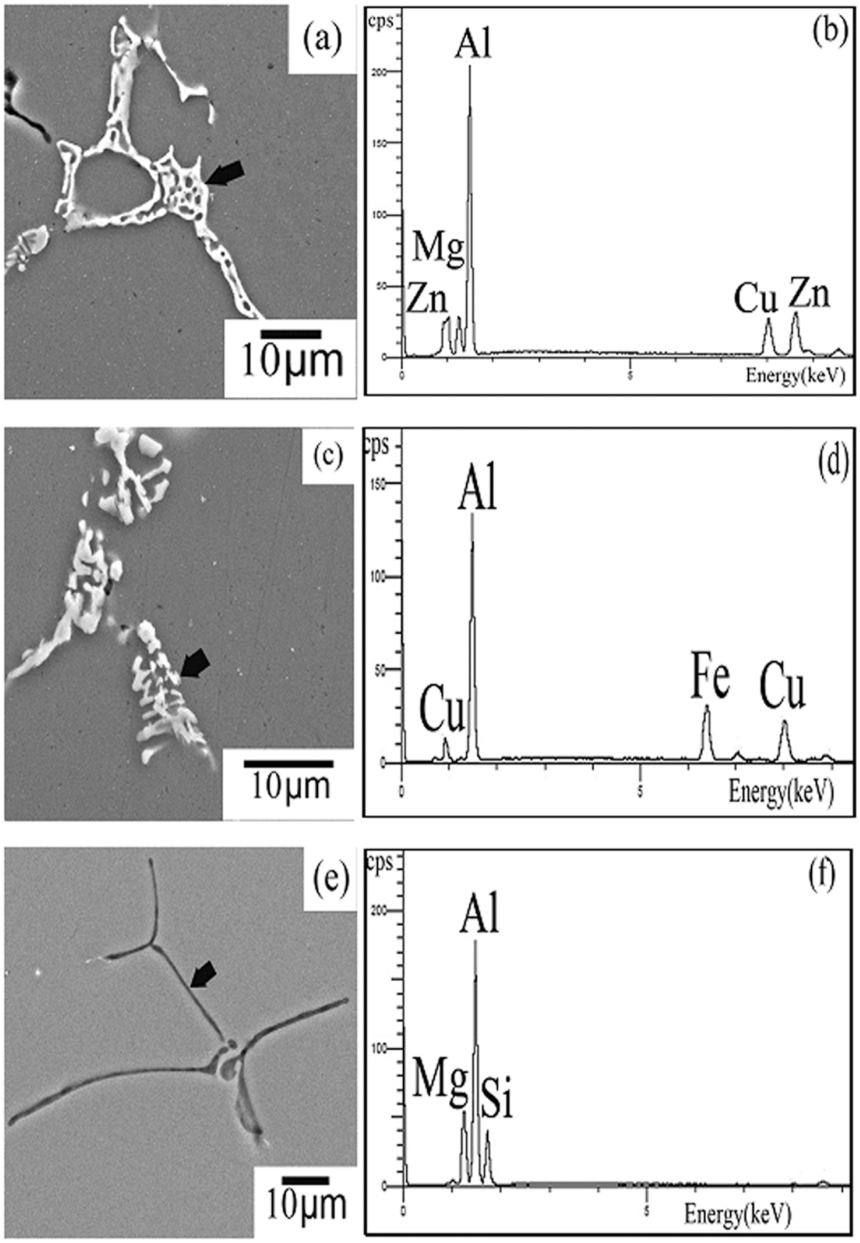

Fig. 4.8 (a), (c), (e) SEM micrographs and (b), (d), (f) EDS results of remaining GB phases after solution heat treatment at 450 °C for 1 h.

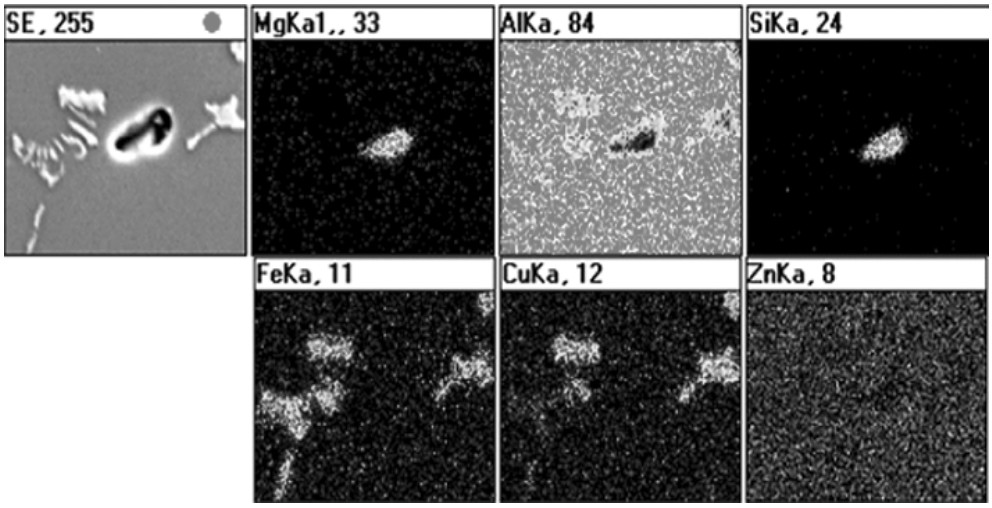

Fig. 4.9 Elemental mapping of constituent particles in the sample solution heat treated at 480 °C for 1h.

Coarse black particles were found to form after solution heat treatment at 450 °C for 8 h and at 480 °C for 1 h. The number of these particles increased with increasing solution treatment time from 1 h to 8 h at 480 °C as shown in Fig. 4.5(e) and Fig. 4.5(f). Chen et al [61] identified the coarse black particles to be melted constituents due to homogenization at high temperature while Curle and Govender [16] reported that it was the pores caused by incipient melting during solution treatment. Fig. 4.9 shows the elemental mapping results of a black constituent particle in the sample solution treated for 1 h at 480 °C; revealing that this particle could be an incipient melting of low melting point $Mg(Zn,Cu,Al)_2$ phase in multinary eutectic area. Owing to high diffusion coefficients of Zn, these atoms would easily diffuse throughout the matrix as solid solution, leaving behind the segregated sluggish silicon atoms to form overheated Mg_2Si particles during quenching. Formation of the Mg_2Si overheated particles was confirmed by the XRD result as shown in Fig. 4.3 and was found to be undesirable because it would reduce toughness and aging response due to the lower supersaturated solid solution remaining in the solution treated sample.

The influence of SHT temperature and time on the microstructure of the alloy was quantitatively analyzed on the area fraction of Al-Cu-Fe phase, Mg_2Si phases, and coarse black particles as shown in Fig. 4.10-4.12. The area fraction results in Fig.4.10 reveal that the content of Al-Cu-Fe intermetallic phases gradually decreases with increasing solution heat treatment time at both temperatures. In contrast, the amounts of Mg-Si intermetallic phase in Fig.4.11 clearly increase when SHT time was over 8 h at 450°C while it slightly changes when SHT times were from 1-12 h at 480°C. It can be noticed from Fig. 4.12 that coarse black particles were not found in the specimen solution treated at 450°C for the first 4 h, however, these particles started to form for prolonging SHT times. On the other hand, coarse black particles were found to form when the specimens were solution treated only for 1 h at 480°C. This observation suggests that SHT temperature of 480°C is high enough to melt $Mg(Zn,Cu,Al)_2$ phase in multinary eutectic area and form coarse Mg_2Si phase afterward leaving no chance of forming black line Mg_2Si as observed in 450°C - solution treated specimens.

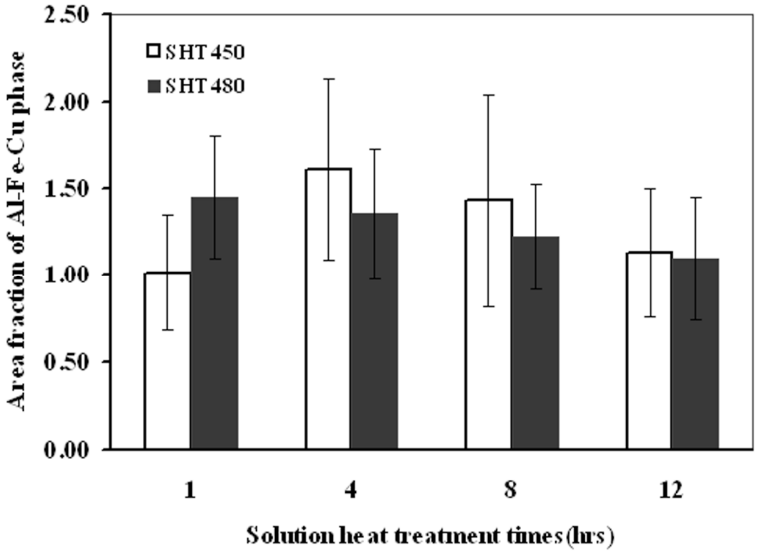

Fig. 4.10 Area fraction of Al-Fe-Cu phases in GISS processing rheocast 7075 Al alloy after SHT at 450°C and 480°C for various time durations.

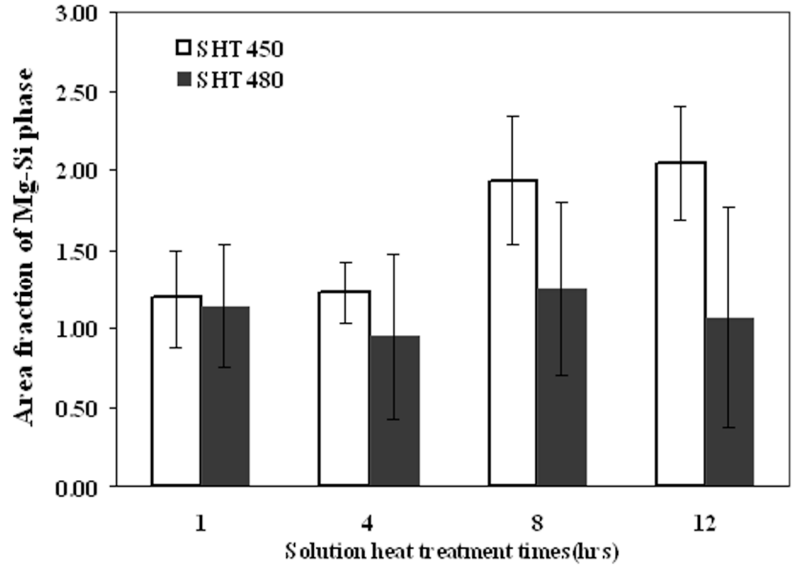

Fig. 4.11 Area fraction of Mg-Si phases in GISS-processed rheocasting 7075 Al alloy after SHT at 450°C and 480°C for various time conditions.

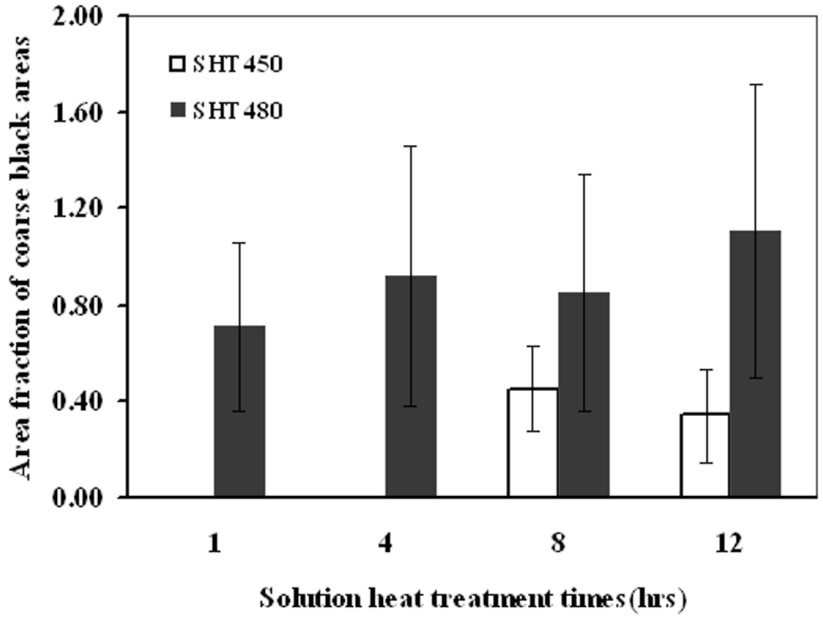

Fig. 4.12 Area fraction of coarse black area in GISS-processed rheocasting 7075 Al alloy after SHT at 450°C and 480°C for various time durations.

The influence of SHT temperature and time on the microstructure of the alloy was quantitatively analyzed on the area fraction of Al-Cu-Fe phase, Mg_2Si phases, and coarse

black particles as shown in Fig. 4.10-4.12. The area fraction results in Fig.4.10 reveal that the content of Al-Cu-Fe intermetallic phases gradually decreases with increasing solution heat treatment time at both temperatures. In contrast, the amounts of Mg-Si intermetallic phase in Fig.4.11 clearly increase when SHT time was over 8 h at 450°C while it slightly changes when SHT times were from 1-12 h at 480°C. It can be noticed from Fig. 4.12 that coarse black particles were not found in the specimen solution treated at 450°C for the first 4 h, however, these particles started to form for prolonging SHT times. On the other hand, coarse black particles were found to form when the specimens were solution treated only for 1 h at 480°C. This observation suggests that SHT temperature of 480°C is high enough to melt $Mg(Zn,Cu,Al)_2$ phase in multinary eutectic area and form coarse Mg_2Si phase afterward leaving no chance of forming black line Mg_2Si as observed in 450°C - solution treated specimens.

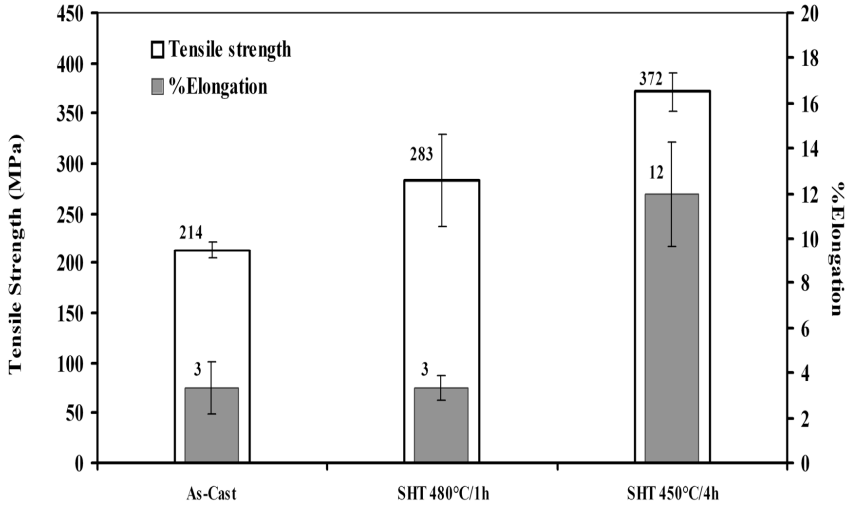

Fig. 4.13 Tensile strength and % elongation of GISS-processed rheocasting 7075 Al alloy before and after SHT.

Effects of SHT on the ultimate tensile strength (UTS) and elongation were carried out. Tensile test results of solution treated specimens are given in Fig. 4.13 indicating that UTS and elongation of 450°C-4 h specimens were higher than those of 480°C-1 h specimens. High density of coarse black particles was a major cause of low strength and elongation in 480°C-1 h. These results hence indicate that the higher SHT temperature, 480°C, at any treated

time and the lower SHT temperature, 450°C, at prolonging SHT time, > 4 h, were not proper to be performed on this alloy. Short SHT time of 1 h at 450°C was also improper for this alloy because the eutectic phase was not completely dissolved. Fig. 4.14 shows the hardness values of 120°C-12 hours artificially aged specimens under different solution treated conditions. It can be seen from this figure that the optimum SHT condition giving the highest hardness value is 450°C-4 h. Therefore, the present study chose to use SHT condition of 450°C-4 h to further investigate the aged hardening effect on the specimen.

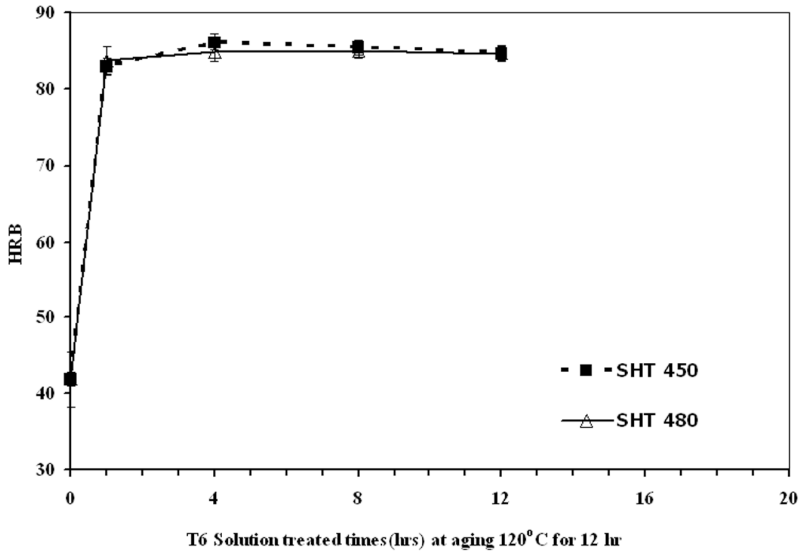

Fig. 4.14 Effects of solution treatment temperature and time on hardness value of the 120°C-12 h artificially aged specimens.

4.3 Effect of Aged hardening on microstructure and mechanical properties

Aging treatment was carried out in order to increase the strength and hardness of the alloy. During a proper solution treatment, the alloy constituents would be dissolved as much as possible without forming brittle and coarse particles. If the alloy is rapidly cooled, e.g. by quenching in water, this rich solid solution will not be stable and excess elements or compounds would precipitate out of the solution resulting in an increase in strength of the alloy. The aging temperatures used in this study were 120°C, 145°C, 165°C, and 185°C. Table 4.1 and Fig. 4.15 shows how the hardness of the specimens varies as a function of time at each aging temperature.

The maximum hardness of the aged specimens produced by GISS technique in this work was attained by aging at 120 °C for 72 h. This result was not in agreement with some previous studies in which the peak aged conditions of 7075 Al alloy formed by squeeze casting and by extrusion were obtained by aging at 120 °C for 24 h [1] and 121°C for 48 h [10], respectively. It is possible that our alloy contained high amount of Fe and Si leading to the formation of the Fe-rich phases and the Mg_2Si phase during casting as mentioned above. These insoluble phases resulted in low supersaturated solid solution in matrix after SHT process. Since aging response depends mainly on the supersaturation degree of the matrix [62], the aging response of this alloy is then slower than that of the 7075 Al alloy containing low contents of Fe and Si. It is also noted from Fig. 8 that the outstanding peak aged conditions of the three other aging temperatures; 145°C, 165°C, and 185 °C, were not present. Instead, the hardness plateau was maintained and the onset hardness for artificial aging at temperatures 145°C, 165°C, and 185 °C were at 6, 3, and 1 h, respectively. As anticipated, the onset of hardness plateau is reached in a shorter time with increasing aging temperatures as diffusion rates are faster at higher temperatures.

Table 3.1 Average hardness values(HRB) of semi-solid cast 7075 Al alloy after solution heat treatment at 450°C and 4 h and followed by aging at 120°C, 145°C, 165°C, and 185 °C for various duration times.

Aging temperature(°C)	**Aging times (h)**	**Hardness number (HRB)**	**SD**
120	0.33	61.9	1.6
	6	82.7	2.1
	12	86.1	0.9
	24	87.8	1.3
	36	88.5	1.3
	48	87.8	1.5
	72	90.3	1.0
	132	87.8	2.9

Aging temperature(°C)	Aging times (h)	Hardness number (HRB)	SD
145	0.33	64.3	2.1
	3	83.7	1.0
	6	86.6	1.2
	12	86.7	2.0
	24	87.4	1.4
	72	85.3	1.3
165	0.33	65.7	2.1
	1	79.8	2.3
	2	82.8	2.1
	3	84.9	1.3
	6	84.3	1.6
	12	84.7	1.3
	24	84.2	1.3
	72	77.7	1.1
185	0.33	70.7	2.4
	1	81.9	1.7
	3	82.7	1.8
	12	77.7	1.3

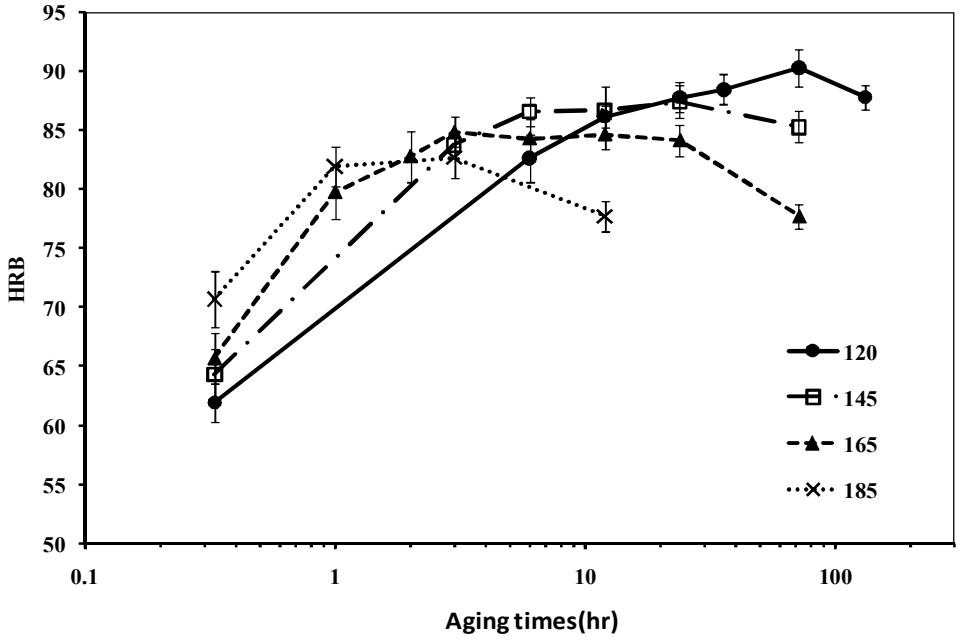

Fig. 4.15 Hardness vs. time for various aging temperatures.

The tensile strength and % elongation of the alloy aging to the peak hardness value and the onset hardness plateau values are shown in Fig. 4.16. The highest average tensile strength of 484 MPa with an average elongation of 3% was measured from specimens aged at temperature of 145^{o}C for 6 h. This was close to an average tensile strength of 479 MPa derived from specimens aged at 120°C for 72 h. Although the strength of the alloy in this study did not meet the wrought alloy target [21], the value was close to those of the thixoformed products as reported in Ref. [2] and [3]. Slight increase in elongation of aged specimens compared to the as-cast specimens and trends of increase in elongation with increasing aging temperatures were observed in the 7075 Al alloy produced by rheocasting with GISS technique. The disappearance of eutectic phases and the existence of insoluble phases resulted in the improvement of average elongation in the SHT specimens to 12%. After aging, however, there was a loss in elongation of about 75% but a gain in strength of about 35% owing to precipitation hardening. Elongation is governed by defects [4] and insoluble phases [60], [63]. High strength casting 7075 Al alloy could be produced through predeformed alloy on aging [64], while thermomechanical process was reported to increase the elongation of cast 7075 Al alloy [65]. However, a combination of precipitate hardening and strain hardening due to dislocation exerts influence on mechanical properties depending on the

predeformed degree [64]. In addition, increase in strength of the alloy with no adverse effect on ductility by two-step artificial aging has been reported [67]. Strength and elongation improvements of the alloy produced by the GISS technique still need to be further investigated.

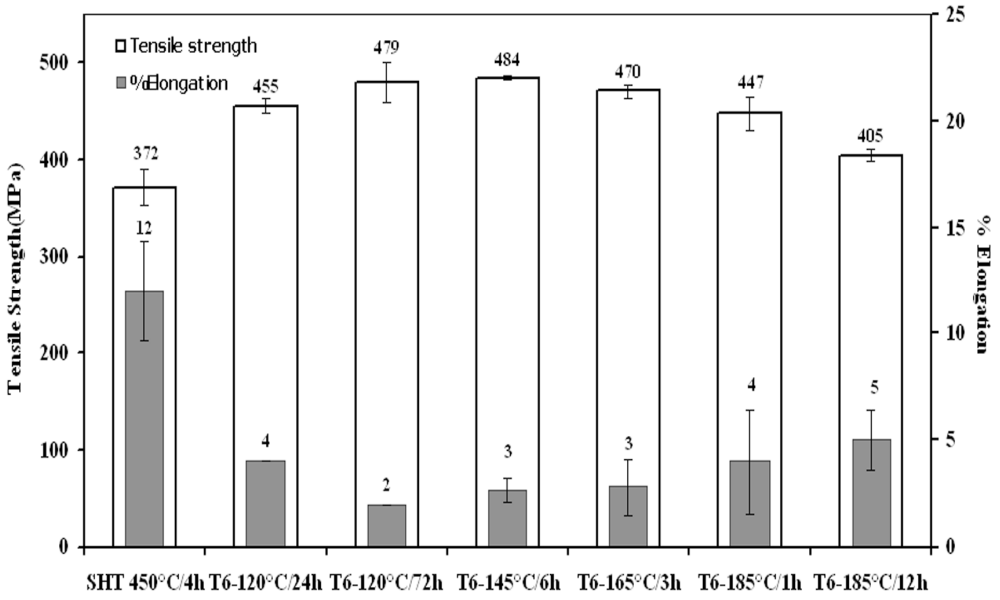

Fig. 4.16 Tensile strength and %elongation of GISS-processed rheocasting 7075 Al alloy after T6 aging process at various temperatures and time durations.

Precipitations in the aged specimens were determined using bright field (BF) imaging and selected area electron diffraction (SAED) analysis on TEM. Fig. 4.17(a) shows [110] zone axis of α -Al matrix in the 120°C-24 h aged specimen. There are no extra spots other than those from the α -Al matrix suggesting that fine precipitates in the aged specimen as shown in Fig. 4.22(a) were GP zone precipitates having the same crystal structure as that of the matrix [67]. This observed precipitate, GP zone, was different from the η' phase formed in commercial 7075 Al alloy after aging under the same conditions, 120°C-24 h [11]. The GP zone precipitates got coarsening and transformed to η' precipitates after increasing aging time to 72 h as observed in Fig. 4.22(b). This evidence was confirmed by the appearance of extra weak precipitate spots shown in [114] zone axis of the 120°C-72 h as shown in Fig. 4.17(b) which corresponded well to the diffraction pattern of precipitates reported in Du et al. [68]. Electron diffraction patterns of

specimens aged at 145°C, 165°C, and 185°C to the onset of hardness plateau also showed the existence of η' phase as observed in Fig. 4.18(b), 4.19(b) and 4.20(a), respectively. It was indexed by diffraction spots at 2/3{220} position, while early nucleation η phase was also indexed by diffuse diffraction around 2/3{220} position at aging conditions of 145°C, 165°C, and 185°C for 6, 3, and 1 h, respectively. Emani et al. [10] suggested that diffraction contrast would increase as the precipitates became coarsened and completely transformed to the transition phases. Clear precipitate spots with no diffusion shown in Fig. 4.21(b) indicated that η phase dominantly formed after aging at 185°C for 12 h corresponding to larger size precipitates as illustrated in Fig. 4.22(f). In the analysis of the diffraction pattern in [112] zone axis using schematic diffraction pattern of Ref. [40] and [17]. η' phase was also found to transform to η phase after aging at 145°C for 6 h, which were indexed by weak diffuse spots at 2/3{220} and 2/3{311} positions, as shown in Fig. 4.18(a). After aging at 165°C for 3 h, precipitate spots , identified to be dominantly η', clearly appeared at 1/3{422} position as shown in the electron diffraction pattern of [111] zone axis in Fig. 4.19(a). In addition, weak η phase spots were also observed near 2/3{220} position, identical to that reported in Ref. [19], [69], [70]. However, extremely weak diffuse spots at 1/3{442} position and low intensity around 2/3{220} position in diffraction pattern [111] zone axis in Fig. 4.20(a) implied that η phase had just started to form in the specimen after aging at 185°C for 1 h. Additionally, η phase spots also appeared on electron diffraction pattern in [001] zone axis, as shown in Fig. 4.20(b). This is in accordance with the schematic diffraction patterns of Ref [42] and [71]. Li et al. [41] reported that GP Zone and η' phase are formed predominantly in the microstructure of the 7075 al alloy at peak aged conditions after a T6 temper coupled with prestretching. In contrast, the present results indicate that fine dispersion of η' phase is mainly responsible for the peak hardness in the alloy, which is in good agreement with the report by Park and Ardell [72]. Moreover, η' phase also predominated and η phase started early to form in the microstructure of the alloy after artificial aging at the three aging temperatures of 145°C, 165°C, and 185°C for onset hardness plateau times.

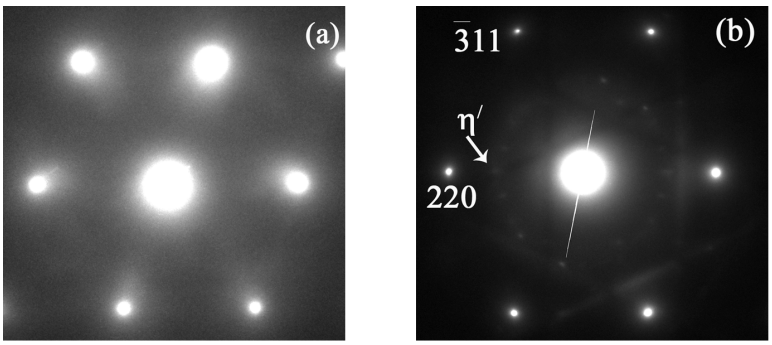

Fig. 4.17 Diffraction patterns (a) [110] zone axis after aging at 120°C-24h (b) [114] zone axis after aging at 120°C-72h.

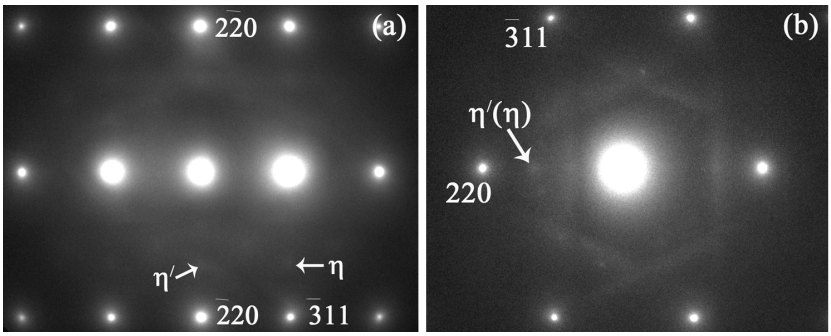

Fig. 4.18 Diffraction patterns after aging at 145°C-6h (a) [112] zone axis (b) [114] zone axis.

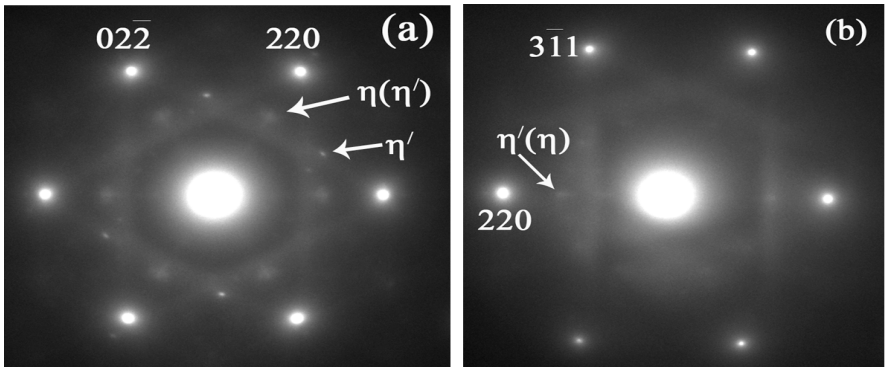

Fig. 4.19 Diffraction patterns after aging at 165°C-3h (a) [111] zone axis (b) [114] zone axis.

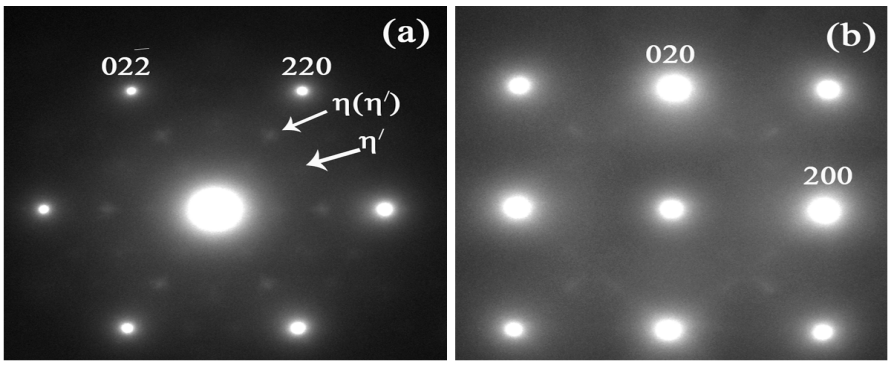

Fig. 4.20 Diffraction patterns after aging at 185°C-1h (a) [111] zone axis (b) [001] zone axis.

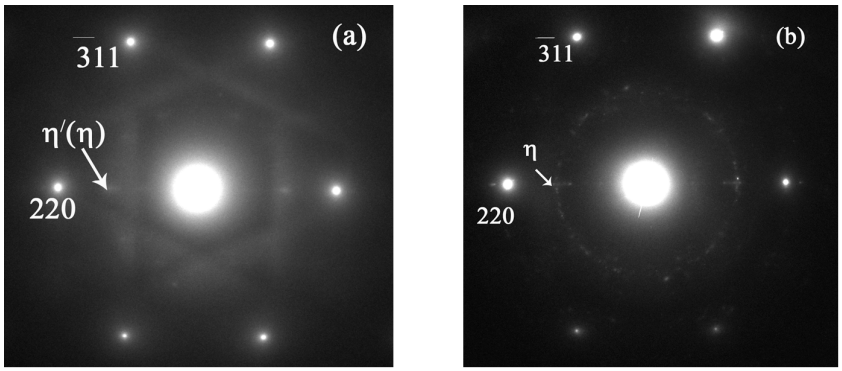

Fig. 4.21 Diffraction patterns of [114] zone axis in specimens aged at (a) 185°C-1h (b) 185°C-12h.

Fig. 4.22 shows the difference in precipitate size and number density of specimens aged at various conditions. High density of very fine GP zone was observed in the specimen aged at an underaged condition of 120°C for 24 h as shown in Fig. 4.22(a). With increasing aging time to 72 h or at optimum ageing condition, the growth of those fine precipitates can be clearly seen (Fig. 4.22(b)). The same trend was observed when comparing specimens aged at 185°C for 1 h to that aged at 185°C for 12 h, an overaged condition, as illustrated in Fig. 4.22(e) and Fig. 4.22(f), respectively. Fig. 4.22(c)-4.22(e) illustrates precipitate morphology in the specimens aged to the onset of hardness plateau at 145°C, 165°C, and 185°C, respectively. From these figures, precipitates seemed to get bigger in size but lower in density at higher aging temperature.

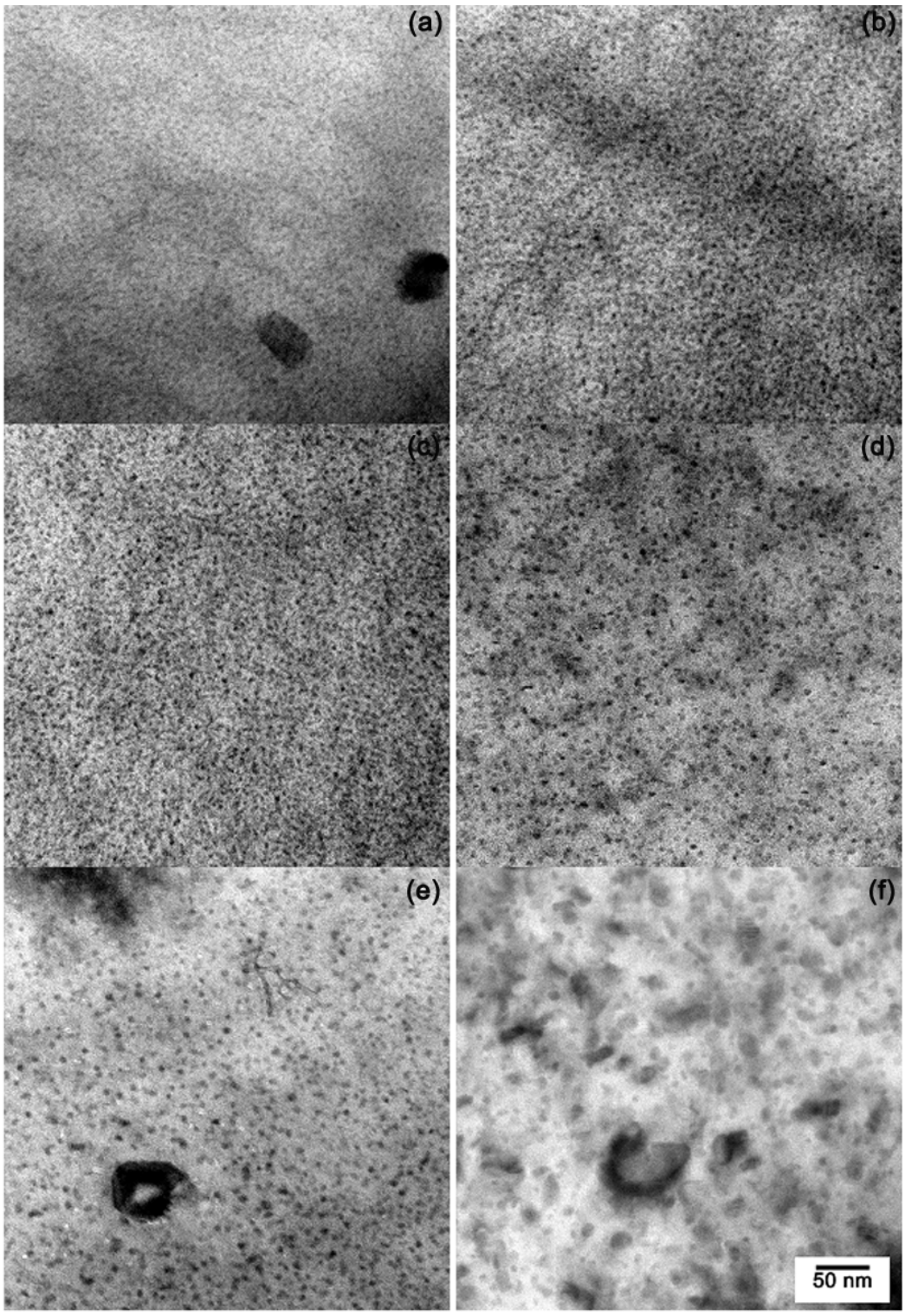

Fig. 4.22 TEM bright field imaging in [011] zone axis of specimen aged at (a) 120°C-24h; and in [114] zone axis of specimens aged at (b) 120°C-72h (c) 145°C-6h (d) 165°C-3h (e) 185°C-1h (f) 185°C-12h.

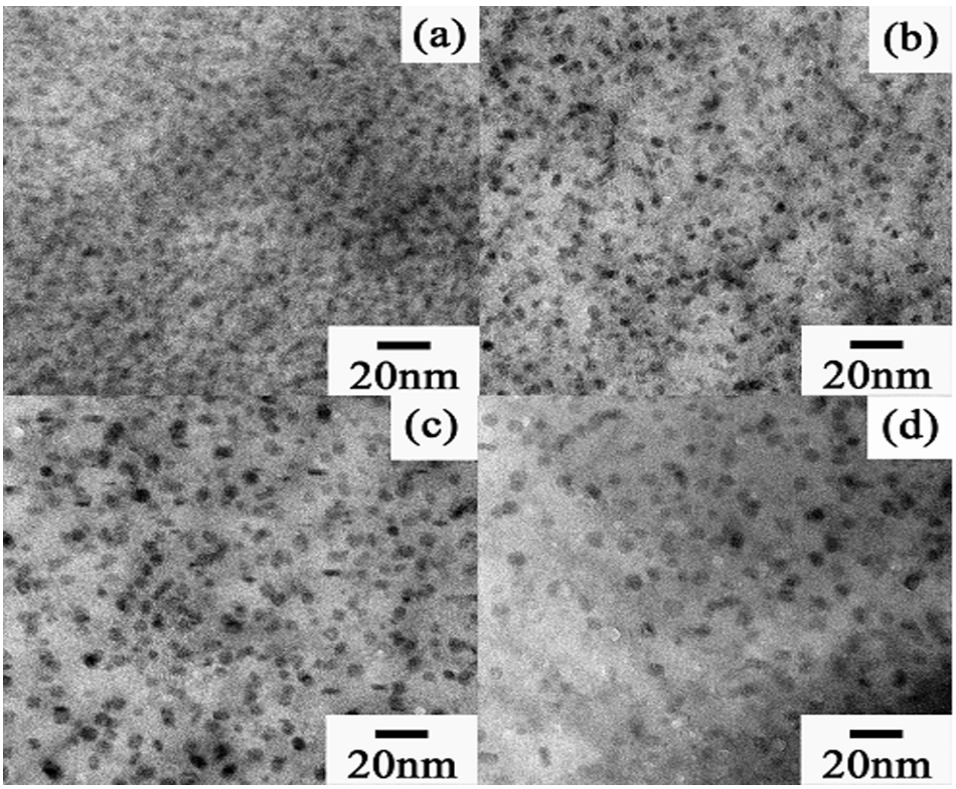

Fig. 4.23 TEM bright field imaging at higher magnification taken in [114] zone axis showing relative precipitate size and number density in four different aged conditions at (a) 120°C-72h (b)145°C-6h (c) 165°C-3h (d) 185°C-1h.

Higher magnification of TEM images in Fig. 4.23 clearly reveals precipitates in the specimens with aging temperatures of 120°C, 145°C, 165°C, and 185°C for 72, 6, 3, and 1 h, respectively. Despite high magnification, it is quite difficult to quantitatively measure the accurate precipitate size and number density from the 120°C-72 h aged specimen. Therefore, the average precipitate size and the precipitate density were only semi-quantitatively measured from the other three ageing conditions and the results were presented in Fig. 4.24. By qualitative comparison from Fig. 4.23, the average precipitate size and the number density of precipitates in 120°C-72 h aged specimen appeared to be smaller and higher than those in other three specimens. Fine precipitates in the three different aged specimens appeared in shape to be both spherical and plate-like. Diameter of precipitates was approximated from the average measurements on the long and short axes of the precipitates [73].

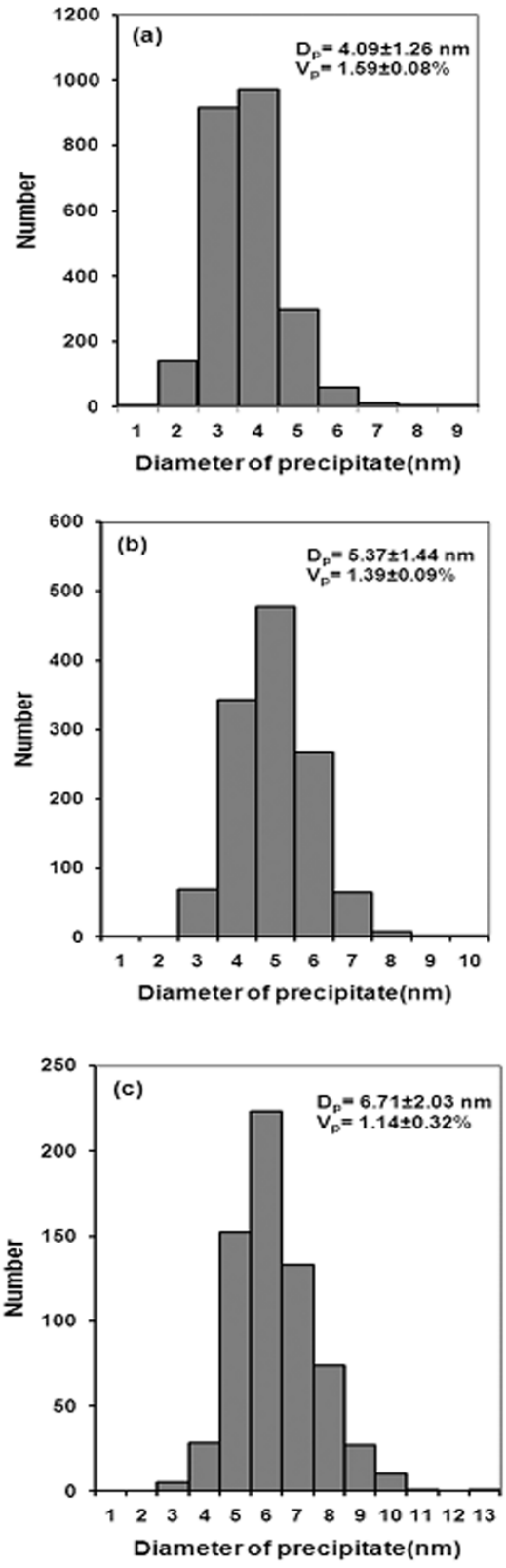

Fig. 4.24 Average precipitate size distributions of aged specimen at (a) 145°C-6h (b) 165°C-3h (c) 185°C-1h.

From Fig. 4.24, fine precipitates of a 145°C-3 h aged specimen were in the size range of 2 to 7 nm in diameter, an average diameter (D_p) of 4.09 nm and volume fraction (V_p) of 1.59%. For a 165°C-3 h and a 185°C-1 h aged specimens, precipitates size increased to be in the range of 3-8 nm and 3-10 nm in diameter with an average size of 5.37 nm and 6.71 nm, respectively. On the other hand, volume fraction in both aging conditions decreased to 1.39% and 1.14%, respectively. Therefore, it can be concluded that by aging specimen at a higher temperature to the optimum condition, η' phase nucleated under the influence of a smaller driving force than at a lower temperature. Thus, precipitate dispersion would be coarser and the volume fraction would be reduced, causing the hardness and the tensile strength to decrease. The precipitate size distribution in this study was consistent with a prior study by Park and Ardell [72] that the diameter of η' phase was in the range of 3-10 nm.

Apparent activation energy for precipitate hardening process of the alloy can be determined following the notation in Ref. [74]. Artificial aging times (in seconds) at the onset of hardness plateau as a function of artificial aging temperatures (in Kelvin) were plotted following an Arrhenius-type response in the equation $t_{T6} = C \exp(Q/RT)$ with C the pre-exponential factor, Q the apparent activation energy in J/mol and R the universal gas constant = 8.314 J/mol.K, as shown in Fig. 4.25. The Arrhenius-type response for the obtained 7075 Al alloy produced by GISS technique is given in equation (4.1)

$$t_{T6} = 4 \times 10^{-8} \exp(95{,}827/RT) \qquad (4.1)$$

The apparent activation energy for precipitate process in the alloy was calculated to be 95,827 J/mol. It had been reported by Garcia and Louis [75] that the apparent activation energies of η' precipitation and η' dissolution in 7075-T6 alloy were 69,200 J/mol and 97,400 J/mol, respectively. It is noted that the activation energy determined from our study is close to the value of the η' dissolution activation energy, indicating that at the onset of hardness plateau the η' phase started to coarsen and transform to η phase. By using equation (4.1), one could predict the time to reach maximum hardness (t_{T6}) of the 7075 Al alloy in this study.

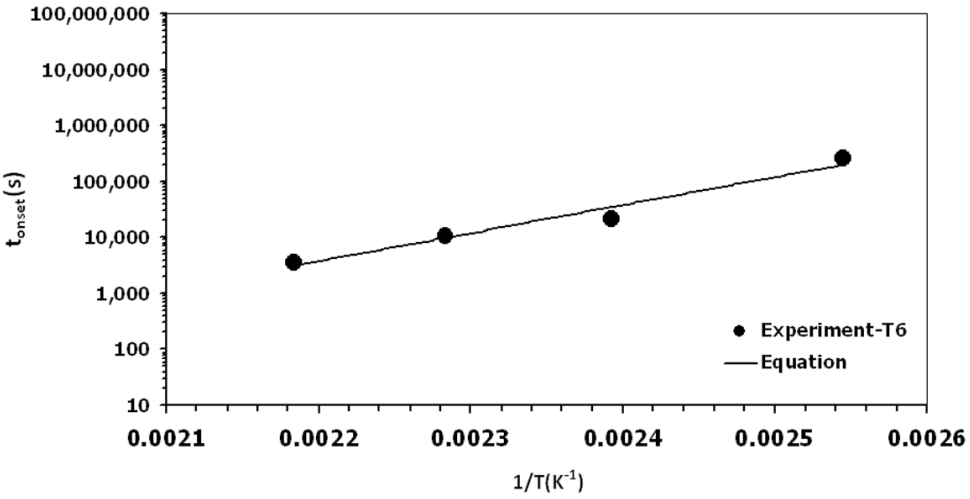

Fig. 4.25 Arrhenius-type plot between aging temperature and onset of hardness plateau time of the alloy.

4.4 Creep rupture behavior of semi-solid cast 7075-T6 Al alloy produced by GISS technique

4.4.1 Microstructure of the alloys prior to creep rupture test

Fig. 4.26 illustrates the polished microstructure prior to creep test observed in the semi-solid cast 7075-T6 Al alloy in comparison with the as-obtained commercial 7075-T651 Al alloy in the longitudinal direction. The semi-solid cast 7075-T6 Al alloy contains large size and high density of the insoluble constituent particles, as depicted in Fig. 4.26(a)-(b). In contrast, the particles break down to smaller size and align as stringer in the rolling direction for commercial 7075-T651 Al alloy, as revealed in Fig. 4.26(c)-(d). Insoluble particles of Al_7Cu_2Fe, $Al_{23}CuFe_4$, Al_6Fe, and Mg_2Si have been mainly observed in 7075 Al alloy [32], [60], [76]. These agree with the EDS analysis in this study with Mg-Si phase for black contrast particles and Al-Fe-Cu particle for white contrast particles, as shown in Fig 4.26(e) and 4.26(f), respectively. The effect of the insoluble particle sizes on creep fracture had been reported that they were acting as the nucleation sites of the cavity [32].

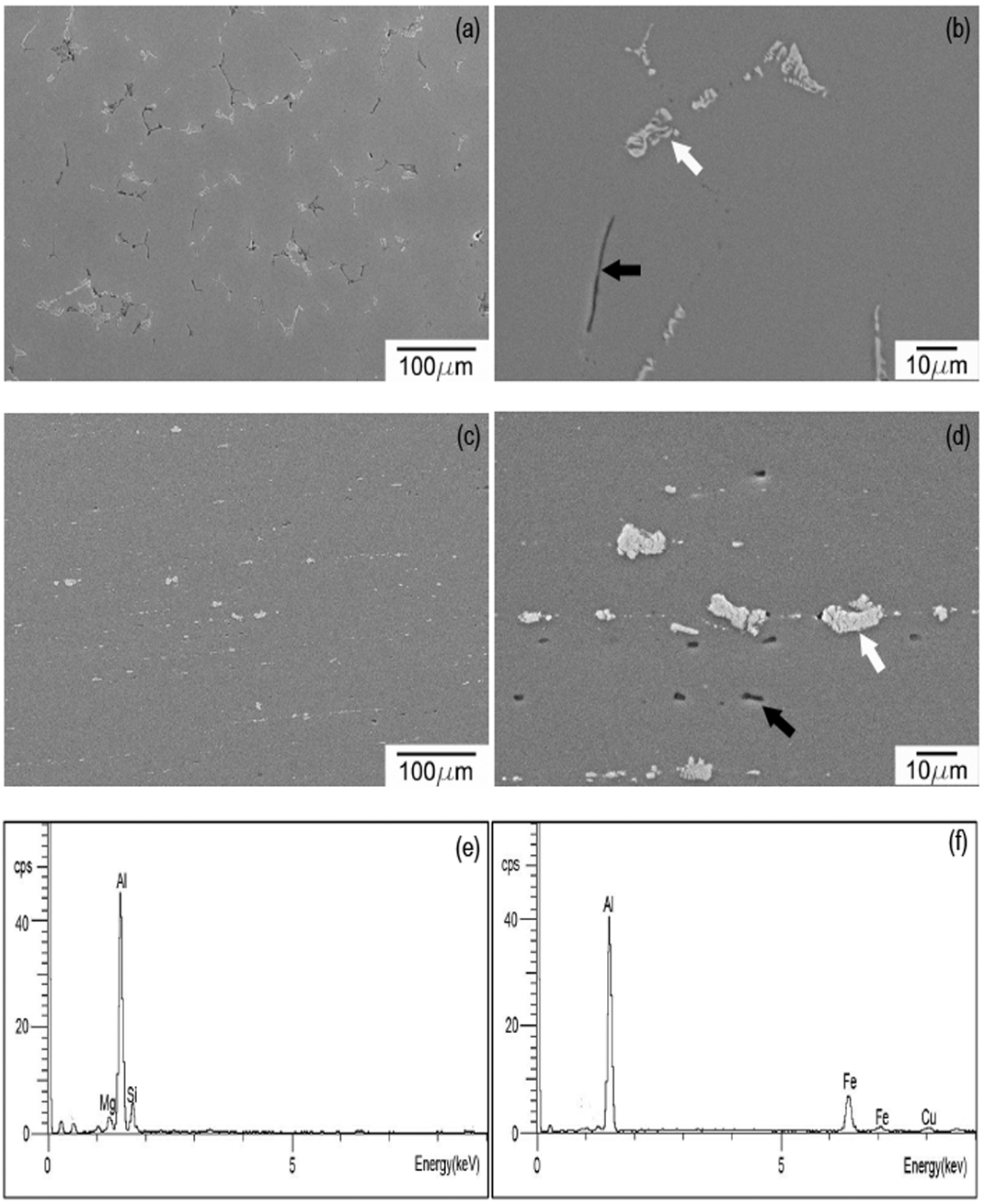

Fig. 4.26 SEM micrographs of (a)-(b) the semi-solid cast7075-T6 Al alloy (c)-(d) the as-obtained commercial 7075-T651 Al alloy (e) EDS result for black contrast particles and (f) EDS result for white contrast particles.

4.4.2 Creep rupture behavior

Typical creep curves of semi-solid cast 7075-T6 Al alloy and commercial 7075-T651 Al alloy under creep test at temperature of 200 °C and stress in the range of 120 MPa to 180 MPa are shown in Fig.4.27. Higher creep rupture strain obtained in the commercial alloy was compared to the semi solid cast alloy. The creep rupture strain of both alloys remained relatively constant with increasing stress levels from 120 MPa to 180 MPa. However, the creep rupture time of the semi-solid cast 7075-T6 Al alloy was longer than the commercial 7075-T651 Al alloy in all applied stress regimes.

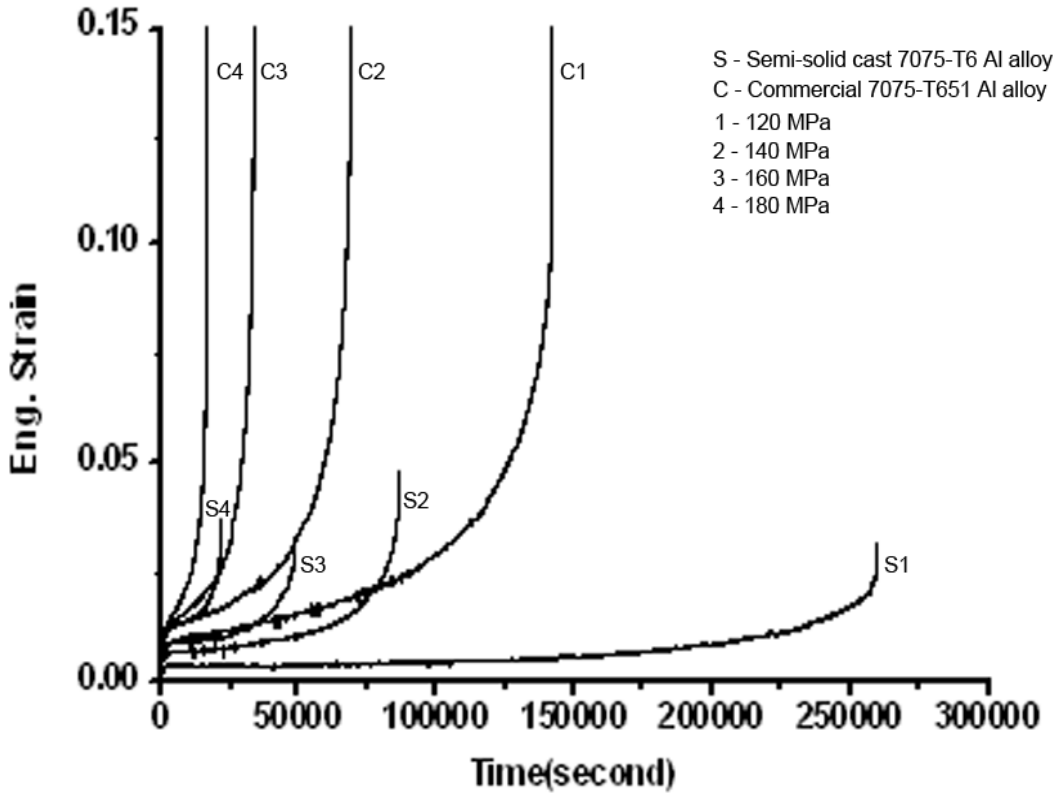

Fig. 4.27 Typical creep curve showing engineering creep strain as function of time under creep test at 200°C and stress ranging from 120MPa to 180MPa.

The applied stress (σ) dependence of the minimum creep rate ($\dot{\varepsilon}_{\min}$) can be approximated by a power law, which was developed for practical purposes in the following simple form of Norton's law:

$$\dot{\varepsilon}_{\min} = A\sigma^n \qquad (4.2)$$

where A is the temperature and microstructure-dependent constant, and n is the stress exponent for the creep. The n value commonly explains the governing creep mechanism. As shown in Fig. 4.28, the minimum creep rate ($\dot{\varepsilon}_{\min}$) has been plotted against the applied stress (σ) on a semi-logarithmic scale. The solid lines fit through the experimental data of the minimum creep rate for each applied stress. The stress exponent n of both alloys was then calculated to be 6.3, coincidentally equal. The presence of an instantaneous strain upon loading and a relatively decelerating primary stage, as observed in Fig.4.27, including the n value of 6.3, partly implied that dislocation creep mechanism is predominant in the controlling of creep deformation in both alloys. Park and Lee [31] derived an n value of 9 for 7075 Al alloy under creep test at temperature between 210°C and 290°C and stress between 49 and 123 MPa. They were quite sure that creep deformation was controlled by dislocation recovery. On the other hand, the n values of the overheated and the annealed 7075 Al Alloy were reported equally to be 5.3 which characterized the dislocation creep controlled [32]. The stress enhancement factor (f) was also evaluated following the form of $\dot{\varepsilon}_{\min} = A(f\sigma)^n$ proposed by Yousefiani et al [32]. They characterized that the stress enhancement factor f=1 referred to the bulk overheated 7075 Al Alloy that deformed uniformly as given by Eq.(4.2), while the factor f=1.48 implied a combination of dislocation creep and grain boundary sliding (GBS) for the annealed 7075 Al alloy. In this study, the factor f of the commercial 7075 alloy was calculated to be 1.3 whereas the factor f was 1.0 for the semi-solid 7075-T6 alloy. Microstructure examinations were performed further to specify the creep mechanism of both alloys.

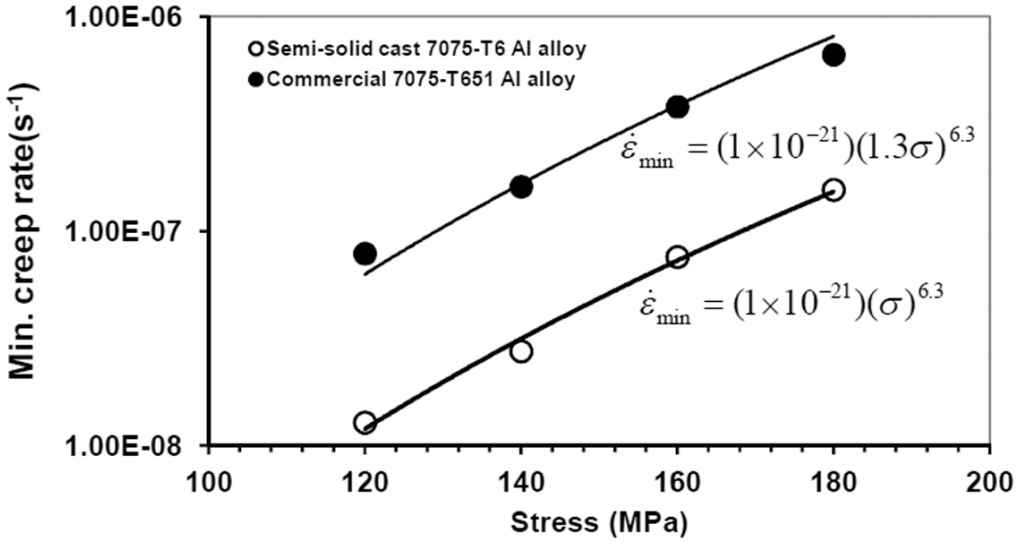

Fig. 4.28 The stress dependence of minimum creep rate.

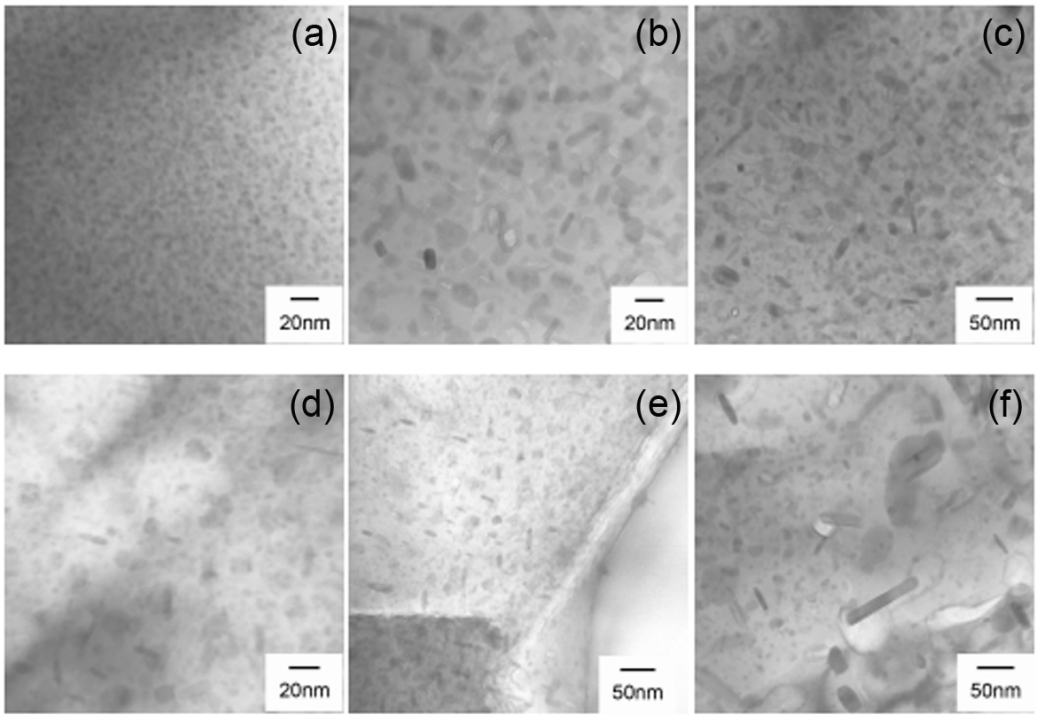

Fig. 4.29 TEM micrographs revealing the precipitates of the semi-solid cast 7075-T6 Al alloy after (a) preheated (b)-(c) creep test for 5 h at 200°C under 140MPa stress; and the commercial 7075-T651 Al alloy after (d)-(e) preheated (f) creep test for 5 h at 200°C under 140MPa stress.

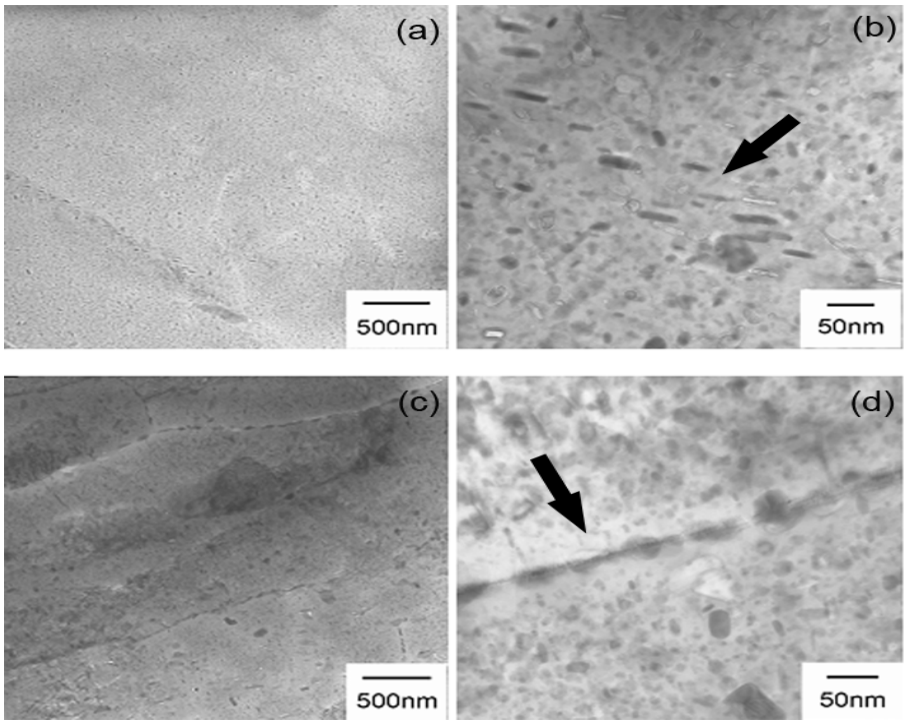

Fig. 4.30 TEM micrographs around the grain boundary after creep test for 5 h at 200°C under 140MPa stress for (a)-(b) the semi-solid cast 7075-T6 Al alloy and (c)-(d) the commercial 7075-T651 Al alloy.

The microstructures of the alloys were then characterized. Densely fine dispersion precipitates could be observed in the microstructure of the semi-solid cast 7075-T6 Al alloy after preheating from room temperature to 200°C for 1 h prior to creep loading, as illustrated in Fig. 4.29(a). Larger precipitate size and lower precipitate density appeared in the microstructure of the commercial 7075-T651 Al alloy, as shown in fig. 4.29(d). It can be noted that these precipitates of both alloys were coarsened after creep loading for 5 h at an applied stress of 140 MPa and temperature of 200°C, as depicted in Fig. 4.29(a)-(b) for the semi-solid cast 7075-T6 Al alloy and 4.29(e)-(f) for the commercial 7075-T651 Al alloy. However, the precipitate coarsening in the commercial 7075-T651 Al alloy was qualitatively faster than the semi-solid cast 7075-T6 Al alloy, as can be visualized in the comparison between Fig. 4.29(c) and 4.29(f). Moreover, the appearance of precipitate free zones (PFZs) coupled with the precipitates at the grain boundary were clear in the commercial 7075-T651 Al alloy, while formation of the PFZs in the semi-solid

cast 7075-T6 Al alloy was not noted, as depicted in fig. 4.30. The PFZs provided the locations for easy dislocation movements [76]. However, grain boundary sliding (GBS) was inhibited when many large particles were present at the grain boundaries [77], making GBS mechanism in the commercial 7075-T651 Al alloy less effective. It is known that the interface of grain boundary precipitate and PFZ is relatively weak [78]. In addition, the difference in precipitate size, precipitate density, as well as free precipitate spacing resulted in the difference in the threshold stresses [46]-[48]. The threshold stress, σ_{th}, is the stress necessary for dislocation to bypass precipitates by Orowan bowing mechanism [46]. The precipitates act as effective obstacles to dislocation motion and no appreciable creep of the alloys can occur below the threshold stress. Hence, the power's law equation at one constant temperature for a steady-state creep rate or a minimum creep rate, $\dot{\varepsilon}_{\min}$, of precipitation-strengthened alloy can be written as followed in Equation (4.3):

$$\dot{\varepsilon}_{\min} = A'\left(\sigma - \sigma_{th}\right)^{n_m} \tag{4.3}$$

Where σ is the applied stress; A', $A' \neq A$, is a constant, and n_m, $n_m \neq n$, is the stress exponent of the matrix. Pure aluminium's n_m (≈ 4.4) was used in this work as suggested by M. E. Van Dalen et al. [47]. Thus, by plotting $\dot{\varepsilon}_{\min}^{\,1/n_m}$ versus σ, one could predict the threshold stress of both alloys from back extrapolation of the creep rate at which it cannot be experimentally measured, as shown in Fig. 6. The figure reveals that the threshold stress of the semi-solid cast 7075-T6 Al alloy having relatively high density and fine precipitates equals to 47.5 MPa, while that of the commercial 7075-T651 Al alloy having larger size and longer free spacing of precipitates is 33.3 MPa. Therefore, the stress enhancement occurring in the commercial 7075-T651 Al alloy was caused by a lower stress threshold and hence led to a higher minimum creep rate compared to that of the semi-solid cast 7075-T6 Al alloy as observed in Fig. 4.28 and Fig. 4.31.

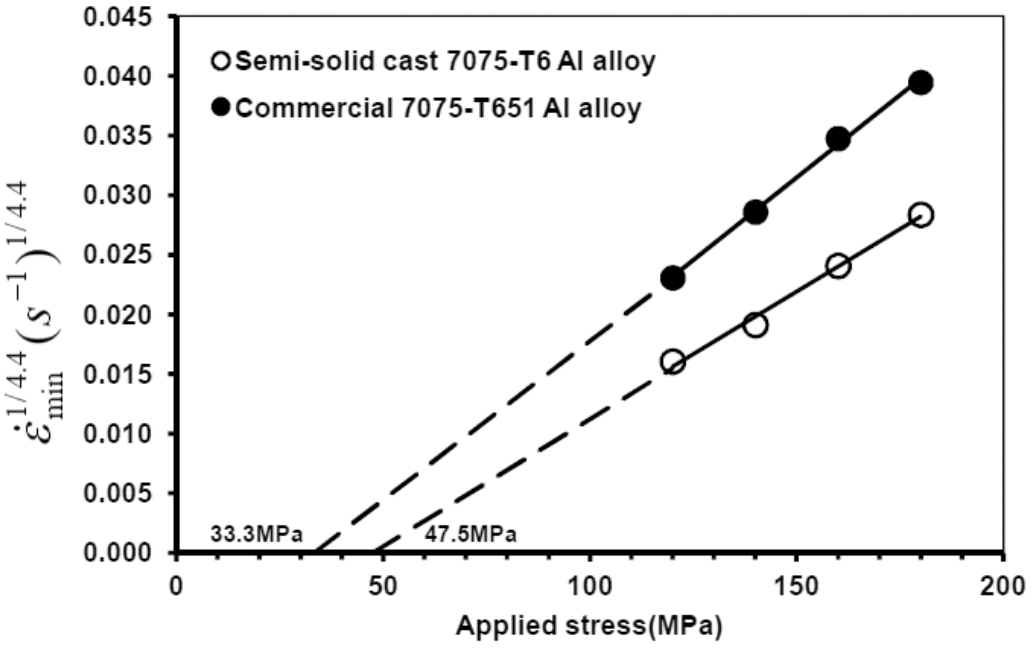

Fig. 4.31 Plotting of $\dot{\varepsilon}_{\min}^{1/4.4}$ vs. applied stress for the determination of threshold stress (σ_{th}) by back extrapolation (dash lines).

Furthermore, precipitate coarsening during creeping led to a decrease in creep strength. Microstructure degradation such as precipitate coarsening, which is a mechanism controlling creep rupture [27] and has been classified by the creep-damage tolerance (λ), is as followed [32], [79]:

$$\lambda = \varepsilon_f / (\dot{\varepsilon}_{\min} t_f) \qquad (4.4)$$

Creep cavitation is dominant when the λ values take on the range from 1 to 2.5. The values are 5 or more for microstructure degradation controlled behavior such as precipitate coarsening. The two mechanisms co-exist if the values fall within the interval of 2.5-5. The creep-damage tolerances λ were plotted against the applied stresses for both alloys in this study, as presented in Fig. 4.32. It can be seen that the λ values for both alloys ranged from 7.9 to 13.5. From the above criteria, precipitate coarsening must have played a significant role in the rupture for both alloys. However, the λ value only refers to whether or not microstructure instability initiates tertiary creep acceleration, and hence metallographic examinations of rupture specimens are necessary to further establish the cause of failure [79].

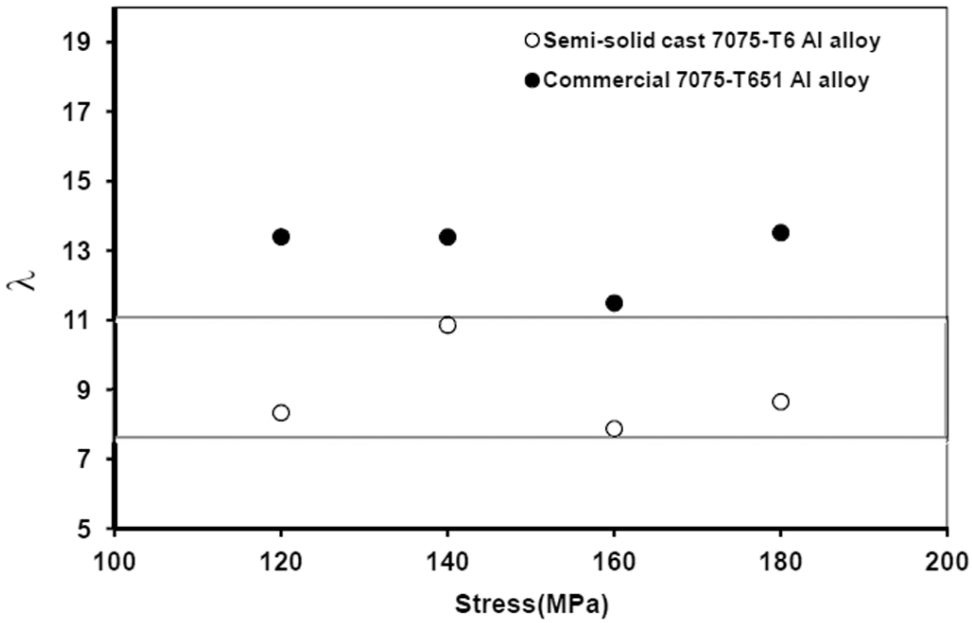

Fig. 4.32 Damage tolerance parameter, λ, as a function of applied stress.

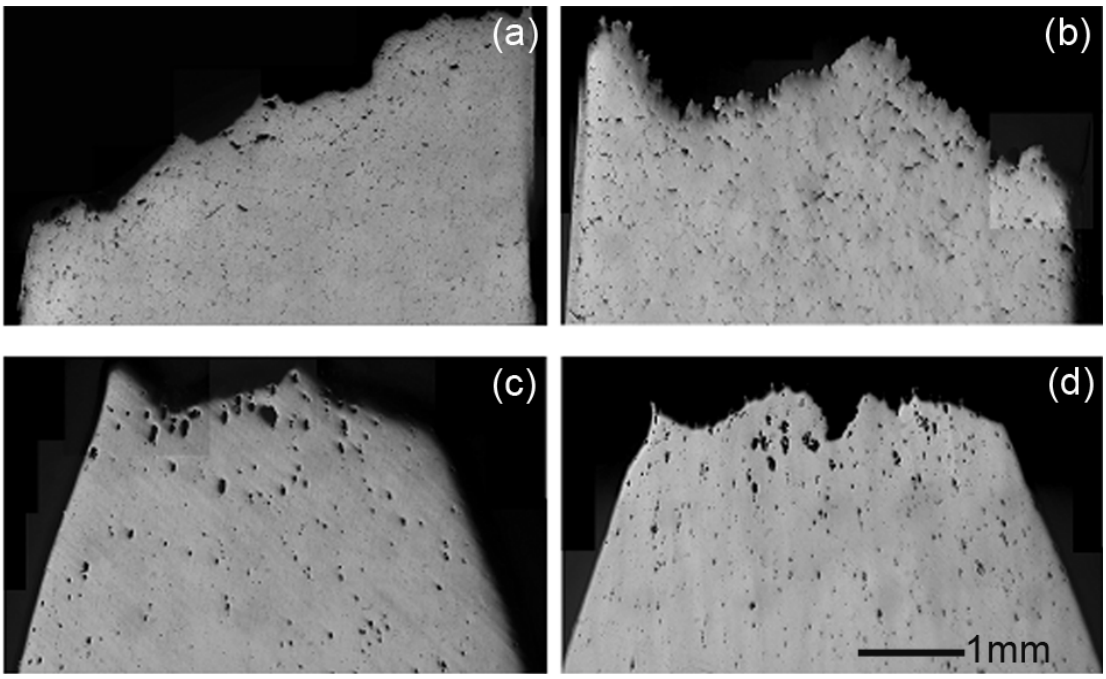

Fig. 4.33 Creep rupture specimens covering a large area near the rupture surface at stress of (a) 120 MPa (b) 180 MPa for the semi-solid cast 7075-T6 Al alloy and (c) 120 MPa (d) 180 MPa the commercial 7075-T651 Al alloy.

Fig. 4.33 shows the polished longitudinal cross sections of selected creep rupture specimens under the lower stress of 120MPa and the higher stress of 180MPa. Under this examination, it can be seen that the deformation and the cavitation regions away from the tips are thus: (1) widespread and large cavitations occur in the commercial 7075-T651 Al alloy samples for both stress regimes; (2) cavity distribution of both alloys increase with increasing stress; (3) more elongated cavities along the direction of the tensile axis appear in the commercial 7075-T651 Al alloy samples; (4) the morphology of cavities in the semi-solid cast 7075-T6 Al alloy samples under both stress conditions has no correlation with the direction of the tensile axis; and (5) necking can be observed only in the commercial 7075-T651 Al alloy samples. The difference in cavity morphology of both alloys might be assumed to have the difference in the creep rupture controlled mechanism [32]. More detailed microstructure examinations of selected creep rupture specimens were conducted through high magnification SEM micrographs and are presented in Fig. 4.34-4.35. The observed semi-solid cast 7075-T6 Al alloy samples under the stress of 120 MPa can be characterized that the appearance of insoluble Al-Fe-Cu particle cracking was initiated like that in position 1 and then extended to form a cavity similar to that in position 3, as seen in Fig. 4.34(a). On the other hand, cavities have also nucleated at insoluble Al-Fe-Cu particles/matrix interfaces for both alloys under all stress regimes, as that in position 2 seen in the micrographs of Fig. 4.34(a)-(b) and Fig. 4.35(b)-(c), due to high stress concentrations. The insoluble Al-Fe-Cu particles/matrix de-cohesion appeared specifically in the semi-solid cast 7075-T6 Al alloy samples under the stress of 180 MPa, as pointed out by the white arrow in Fig. 4.34(c). Matrix deformation in the commercial 7075-T651 Al alloy samples can be clearly observed after the creep rupture test, as pointed out by the black arrow in Fig. 4.35(a), whereas it did not appear in the semi-solid cast 7075-T6 Al alloy samples in Fig. 4.35(b). It can be deduced from these evidences in the present work that creep cavitation is predominantly a creep rupture controlled mechanism in the semi-solid cast 7075-T6 Al alloy with λ values of around 7-11, and the λ values of the semi-solid cast 7075-T6 Al alloy are lower than that of the commercial 7075-T651 Al alloy. Precipitate coarsening and creep cavitation together induce the creep rupture in the commercial 7075-T651 Al alloy with λ values of more than 11. According to the criteria proposed in other reference [32], as mentioned earlier, our λ results should have led a conclusion that our creep rupture mechanism should be that of precipitation coarsening, but they are not. In

other words, the λ values of the alloys in the present work are not in agreement with previous reference if it were to be used as the same criteria. In the present work, to stress again once more, creep cavity control predominate over for λ values of 11 or lower, and a combination of rapid precipitate coarsening and cavity control the creep rupture for λ values higher than 11. This effect could be due to different heat treatment methods to the parent Al materials. As for other materials, such as steel, it has been reported that the values for cavity developed cracks are for $\lambda < 2$, while microstructure instability controlled mechanism or precipitate coarsening cracks occur for $\lambda > 2$ [79].

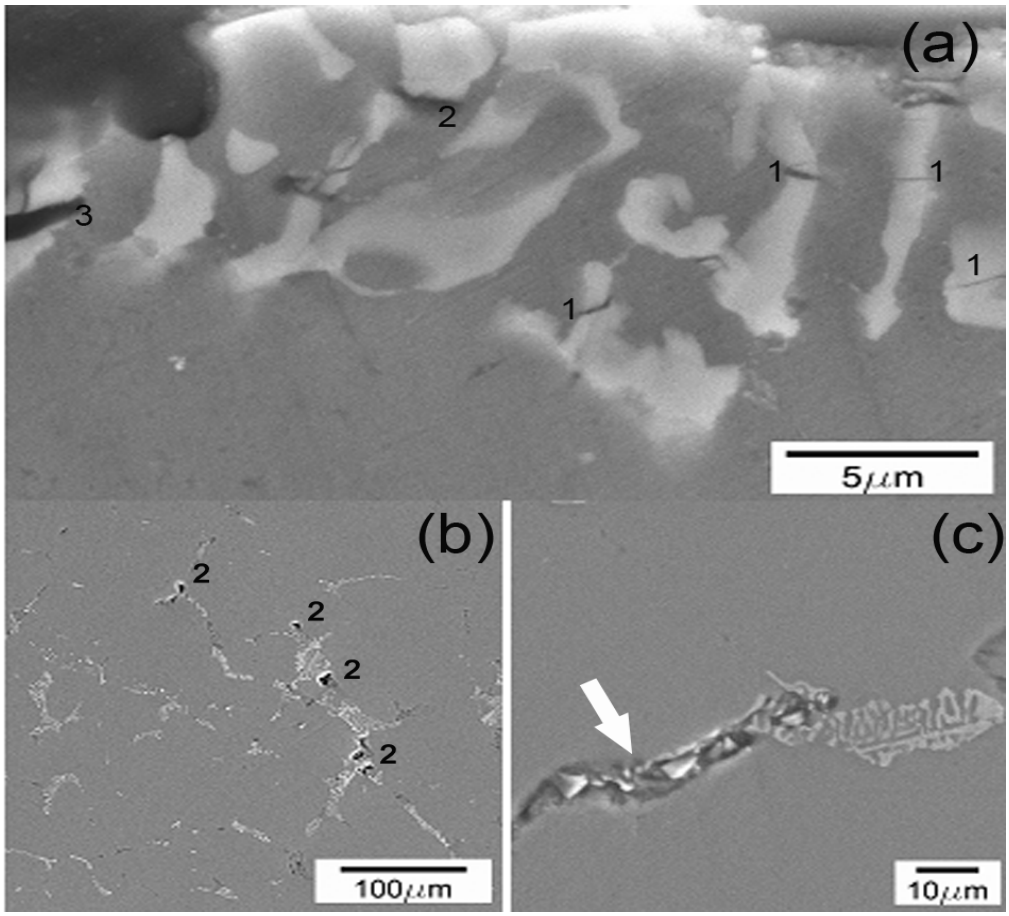

Fig. 4.34 Typical cavity nucleation in the semi-solid cast 7075-T6 Al alloy at the area away from the rupture tip within 0.4 mm.

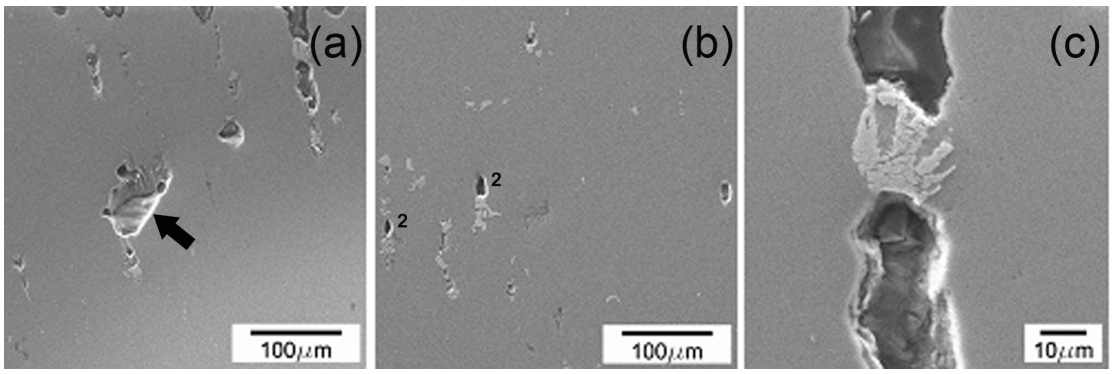

Fig. 4.35 Typical cavity nucleation in the commercial 7075-T651 Al alloy at the area away from the rupture tip (a) and (c) within 0.4 mm, and (b) more than 0.4 mm.

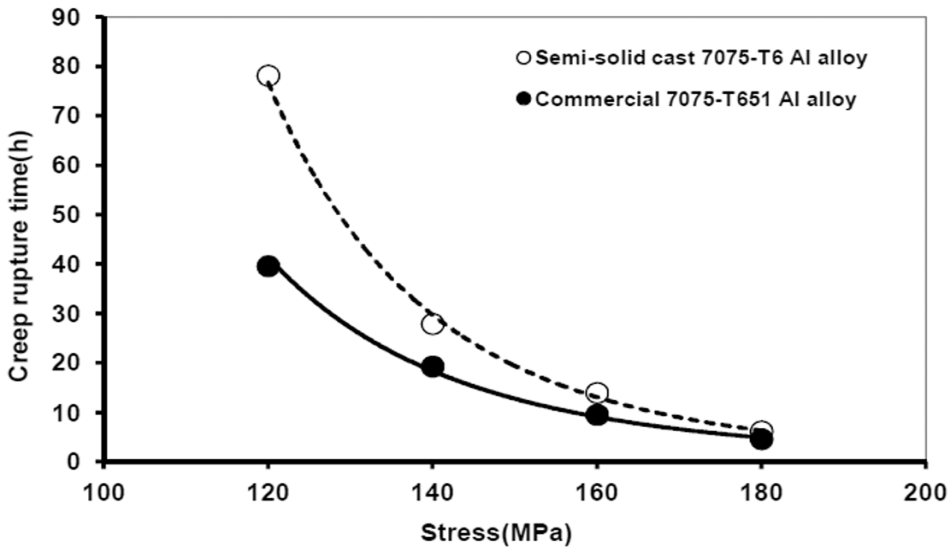

Fig. 4.36 Stress dependence of creep rupture time.

Fig. 4.36 shows the stress dependence to the creep rupture time. The creep rupture time of either alloy is shorter with increasing stress. Generally, the creep rupture time of the semi-solid cast7075-T6 Al alloy is longer than the commercial 7075-T651 Al alloy under creep test at all applied stress regimes. The difference in creep rupture time is distinct at the lower applied stresses of 120 MPa and 140 MPa. At higher applied stresses of 160 and 180 MPa the creep rupture times of both alloys are not so markedly different. De-cohesion occurs when a stress reaches a critical value at a failure site [80]. It is plausible that the increase in the applied stress

accelerates de-cohesion between the insoluble Al-Fe-Cu particles/matrices beyond the nucleating cavity sites at insoluble Al-Fe-Cu particle/matrix interfaces, as evident in Fig. 4.34(c). This effect produces propagation of cavities and accelerates creep rupture time in the semi-solid cast 7075-T6 Al alloy at the higher applied stresses.

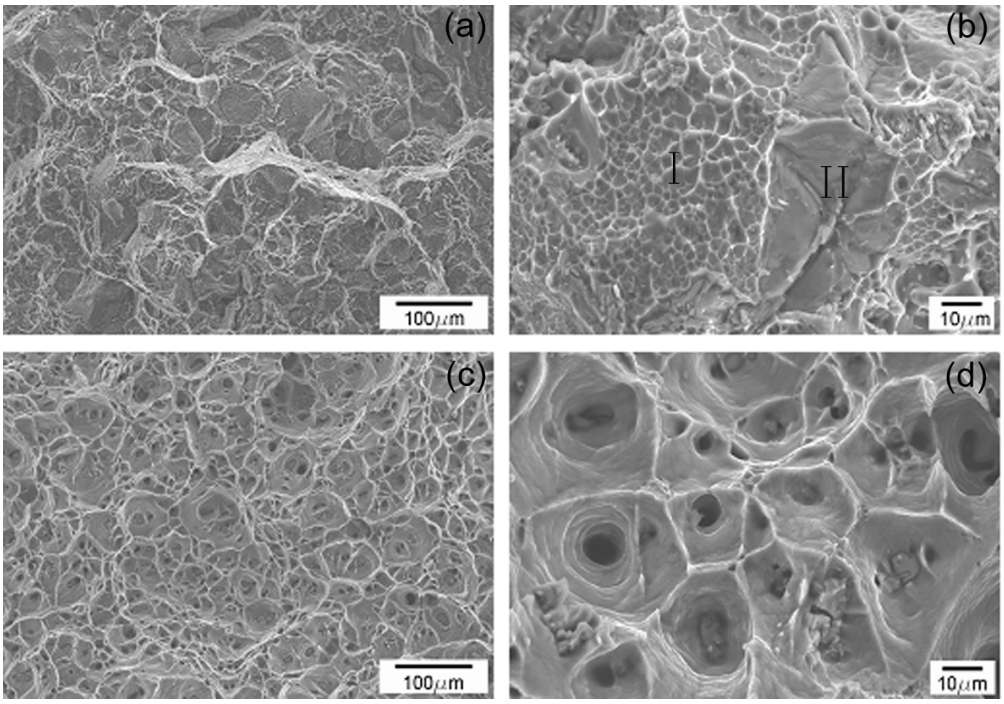

Fig. 4.37 Rupture surface under selected creep test condition at stress of 180MPa for (a)-(b) the semi-solid cast7075-T6 Al alloy and (c)-(d) the commercial 7075-T651 Al alloy

Fig. 4.37 shows SEM micrographs of distinctive rupture surface characteristics of both alloys. The semi-solid cast7075-T6 Al alloy ruptured in a brittle manner of quasi-cleavage form, conforming to that described in Ref. [81]. Higher magnification in Fig. 4.37(b) reveals two typical features observed in the rupture surface: (1) less ductile regions I, created by the growth and the coalescence of voids formed within the α-Al matrix and (2) apparently quasi-cleavage region II, created by de-cohesion between insoluble particle/matrix interfaces. Element mapping of the rupture surface for the semi-solid 7075-T6 Al alloy highlights the quasi-cleavage areas being either Mg-Si particles or Al-Fe-Cu particles, as seen in Fig. 4.38.

Ductile manner appeared in the commercial 7075-T651 Al alloy, as characterized by dimples in the rupture surfaces [32], [81] depicted in Fig. 4.37(c) and (d). In contrast, smaller surface areas of those insoluble particles appear in the commercial 7075-T651 Al alloy, as noted in Fig. 4.39. Signal within dimples cannot be detected. However, particles within dimples could be analyzed by EDS point scan. These particles were found to be in the Fe-rich phase, as shown in the EDS sample result in Fig. 4.40.

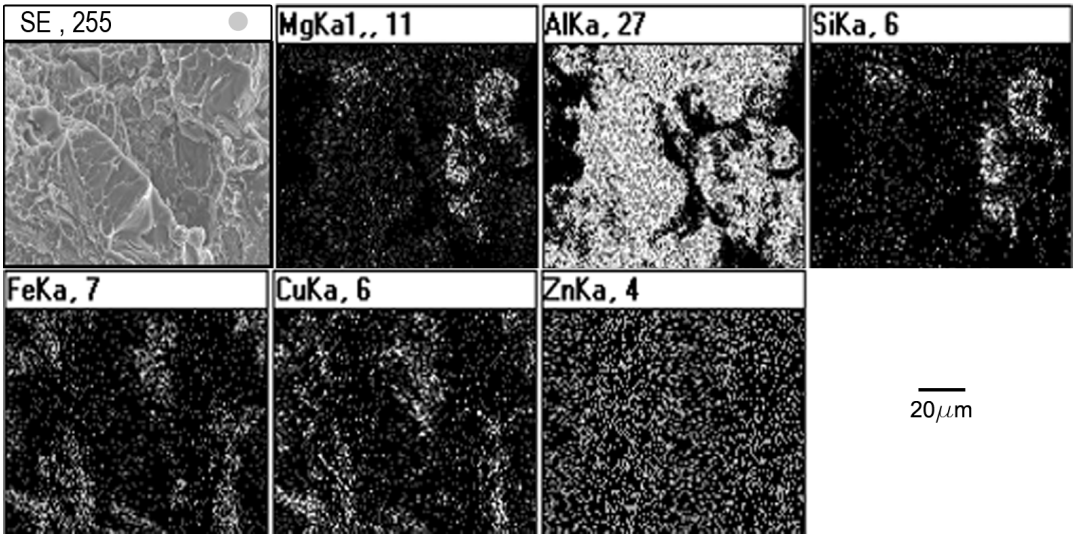

Fig. 4.38 Element mapping of the rupture surface under creep rupture test at stress of 180MPa for the semi-solid 7075-T6 Al alloy.

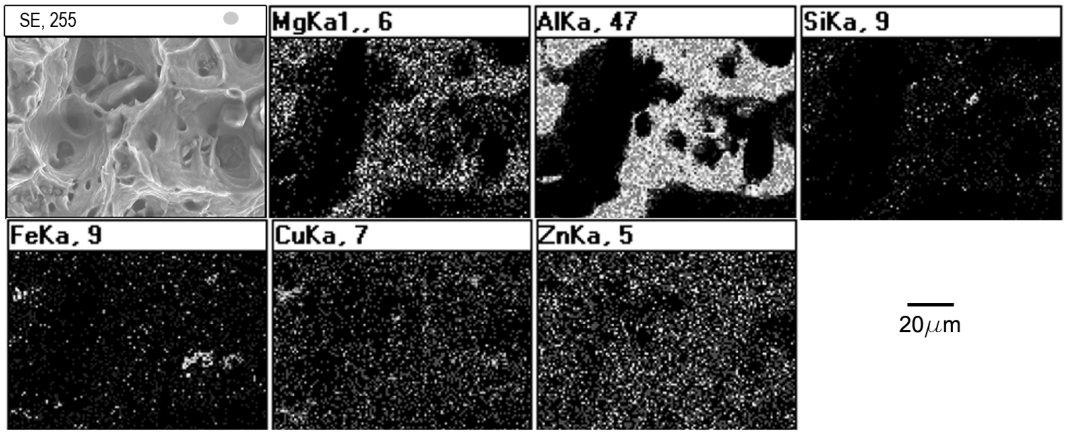

Fig. 4.39 Element mapping of the rupture surface under creep rupture test at stress of 180MPa for the commercial 7075-T651 Al alloy.

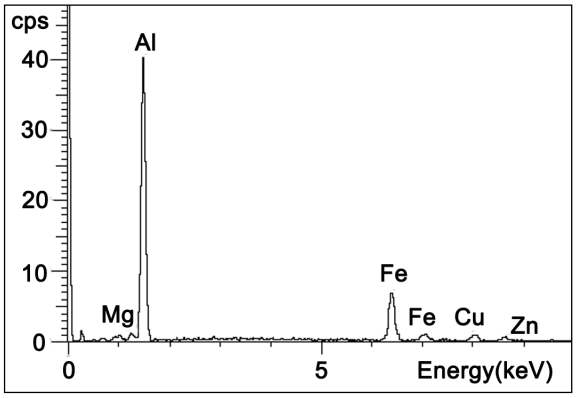

Fig. 4.40 EDS result of a particle within a dimple of the commercial 7075-T651 Al alloy.

CHARPTER 5

CONCLUSIONS

5.1 Conclusions

The study results of this thesis have been reported and discussed in a previous chapter. Details of T6 heat treatment studies were mainly presented into three topics. One investigated the influence of solution heat treatment temperature and times on microstructures and mechanical properties of semi-solid cast 7075 Al alloy produced by GISS technique. Next one studied the effect of aging temperatures and time on microstructure and mechanical properties of the alloy after passing optimum solution heat treatment condition. Another explored the creep rupture behavior of the semi-solid cast 7075-T6 in comparison with the commercial 7075 Al alloy under temperature of 200°C. This chapter will conclude the all result studies which divide into three topics as well.

5.1.1 Influence of solution heat treatment temperature and times on microstructures and mechanical properties of semi-solid cast 7075 Al alloy produced by GISS technique

5.1.1.1. As-cast samples consist of two main phases: a non-dendritic grain structure of α-Al phase and grain boundary eutectic phase (α-Al+ $Mg(Zn,Cu,Al)_2$).

5.1.1.2. The eutectic phases completely dissolved after solution heat treatment for 1 h at 480 °C, and for 4 h at 450 °C.

5.1.1.3. High solution treatment temperature of 480°C and prolonged solution heat treatment time at 450°C resulted in incipient melting which led to the formation of deteriorated overheated Mg_2Si particles.

5.1.1.4. The remaining GB phases of elongated Mg_2Si phase and Cu_2FeAl_7 phase were found in microstructure of the alloy after solution heat treatment at either temperature for various holding times.

5.1.1.5. The optimum solution heat treatment condition derived from this study was thus 4 h at 450 $^{\circ}$C.

5.1.2 Effect of aging temperatures and time on microstructure and mechanical properties of the alloy after passed optimum solution heat treatment condition

5.1.2.1. By using of solution heat treatment condition and by aging the specimen to complete T6 heat treatment, the highest hardness and the highest UTS of about 90 HRB and 486 MPa were obtained from the specimen artificially aged at 120°C for 72 h.

5.1.2.2. At higher aging temperatures, 145°C, 165°C, and 185°C, the peak hardness values decreased while the precipitate size increased with increasing aging temperature as the number density of fine precipitates decreased owing to the lower driving force for nucleation at higher aging temperature. However, the time to achieve the optimum hardness was shorter due to higher diffusion rate at higher aging temperature.

5.1.2.3. The η' phase was mainly responsible for strengthening at all aging temperatures, while the η phase started to form at 145°C, 165°C, and 185°C for the onset of hardness plateau times.

5.1.2.4. The activation energy for forming the precipitates of the alloy at the onset of peak-aged time derived from this research was 95,827 J/mol.

5.1.3 Creep rupture behavior and microstructure characterization of semi-solid cast 7075-T6 Al alloy produced by Gas Induced Semi-Solid (GISS) process in comparison with commercial 7075-T651 Al alloy under temperature of 200°C

5.1.3.1. Creep deformation of both alloys was found to be controlled by dislocation mechanism, with an equal stress exponent n value of 6.3 for both alloys as the basis.

5.1.3.2. Slow precipitate coarsening of the semi-solid cast 7075-T6 Al alloy resulted in lower minimum creep rate and longer creep rupture time than the commercial 7075-T651 Al alloy. Creep rupture time of the semi-solid cast 7075-T6 Al alloy was distinctly longer

than the commercial 7075-T651 Al alloy at stress regimes of 120-140 MPa because of qualitatively lower precipitate coarsening and higher precipitate density.

5.1.3.3. Creep cavity predominantly controlled creep rupture of the semi-solid cast 7075-T6 Al alloy despite the appearance of precipitate coarsening.

5.1.3.4. A combination of rapid precipitate coarsening and creep cavity controlled the creep rupture in the commercial 7075-T651 Al alloy.

5.1.3.5. All cavities in the semi-solid cast 7075-T6 Al alloy, as well as in the commercial 7075-T651 Al alloy, were found to be initiated at the interface of Al-Fe-Cu insoluble particles and the matrix.

5.1.3.6. De-cohesion between insoluble particles and the matrix was found to be accelerated at higher stresses, leading to propagation of cavities and convergence of creep rupture time of the semi-solid cast 7075-T6 Al alloy to be shorter and closer to that of the commercial 7075-T651 Al alloy.

5.1.3.7. Creep cavity control predominate over for λ values of 11 or lower, and a combination of rapid precipitate coarsening and cavity control the creep rupture for λ values higher than 11.

5.1.3.8. Quasi-cleavage brittle manner covered the rupture surface of the semi-solid cast 7075-T6 Al alloy. In contrast, dimple ductile manner was typical for the creep rupture surface in the commercial 7075-T651 Al alloy.

5.2 Suggestions

5.2.1 Improving the ductility of semi-solid cast 7075 Al alloy produced by GISS technique could be done by deceasing the impurity Fe content of lower 0.25%wt and the impurity Si content of lower 0.15%. Another way applies for the combination of heat treatment process and other process such as thermomechanical process.

5.2.2 Interval temperatures of between 450°C and 480°C are interesting for investigating the dissolved eutectic phases. However, the temperature in the chamber furnace should be homogenous.

5.2.3 The morphology of precipitates at peak aged condition of 120°C for 72 h examined by using High Resolution Transmission Electron Microscope (HRTEM) is further interesting study as well.

5.2.4 Additional studies of creep behavior of semi-solid cast 7075-T6 Al alloy produced by GISS technique can be explored under lower and over temperature of 200°C, including the semi-solid cast 7075 Al alloy contained low content of Fe and Si elements .

5.2.5 The precipitate coarsening during creep of the semi-solid cast 7075-T6 Al alloy is interesting topic in comparison with the commercial 7075 Al alloy.

REFERENCES

[1] S. W. Kim et al.,"The study on characteristics of heat treatment of the direct squeeze cast 7075 wrought Al alloy," *Mater. Sci. Eng. A*, vol. 304–306A, pp. 721–726, 2001.

[2] J. Dong et al,"Liquidus semi-continuous casting, reheating and thixoforming of a wrought aluminum alloy 7075," *Mater. Sci. Eng. A*, Vol. 345A, pp. 234 -242, 2003.

[3] D. Liu et al., "Microstructural evolution and tensile mechanical properties of thixoformed high performance aluminium alloys," *Mater. Sci. Eng. A*, Vol. 361A, pp. 213–224, 2003.

[4] S. Chayong et al., "Thixoforming 7075 aluminium alloys," *Mater. Sci. Eng. A*, vol. 390A, pp. 3–12, 2005.

[5] R. Clark Jr et al., "On the correlation of mechanical and physical properties of 7075-T6 Al alloy," *Eng. Fail. Anal.*, vol.12, pp. 520–526, 2005.

[6] O. S. Es-Said et al., "Warpage Behavior of 7075 Aluminum Alloy Extrusions," *J. Mater. Eng. Perform.*, vol. 16 pp. 242–247, 2007.

[7] S. K. Kim et al., "Novel thixoextrusion process for Al wrought alloys, " *J. Mater. Process. Technol.*, vol. 187–188, pp. 354–357, 2007.

[8] H. S. Turkmen et al., "On the mechanical behaviour of AA 7075-T6 during cyclic loading," *Int. J. Fatigue*, vol. 25, pp. 267–281, 2003.

[9] J. Jabra et al., "The effect of thermal exposure on the mechanical properties of 2099-T6 die forgings, 2099-T83 extrusions,7075-T7651 plate, 7085-T7452 die forgings, 7085-T7651 plate, and 2397-T87 plate aluminum alloys," *J. Mater. Eng. Perform*., vol. 15, pp. 601-607, 2006.

[10] S. V. Emani et al., "Double aging and thermomechanical heat treatment of AA7075 aluminum alloy extrusions," *J. Mater. Sci.*, vol. 44, pp. 6384–6391, 2009.

[11] J. F. Li et al., "Mechanical properties, corrosion behaviors and microstructures of 7075 aluminium alloy with various aging treatments," *Trans. Nonferrous Met. Soc. China*, vol. 18, pp. 755-762, 2008.

[12] J. Wannasin et al., "Research and development of gas induced semi-solid process for industrial applications," *Trans. Nonferrous Met. Soc. China*, vol. 20, pp. s1010-s1015, 2010.

[13] S. Thanabumrungkul et al., "Industrial development of gas induced semi-solid process," *Trans. Nonferrous Met. Soc. China*, vol. 20, pp. s1016-s1021, 2010.

[14] D. B. Spencer et al., " Theological Behavior of Sn-15%Pct Pb in the Crystallization Range," *Metall. Trans*., vol. 3, pp. 1925-1932, 1972.

[15] H. V. Atkinson, "Modelling the semisolid processing of metallic alloys," *Prog. Mater. Sci*., vol. 50, pp. 341–412, 2005.

[16] U. A. Curle and G. Govender, "Semi-solid rheocasting of grain refined aluminum alloy 7075," *Trans. Nonferrous Met. Soc. China*, vol. 20, pp. s832-s836, 2010.

[17] X. Z. Li et al., "HREM study and structure modeling of the η' phase, the hardening precipitates in commercial Al–Zn–Mg alloys," *Acta Mater*., vol. 47, no. 9, pp. 2651-2659, 1999.

[18] L. K. Berg et al., "GP-zones in Al–Zn–Mg alloys and their role in artificial aging," *Acta Mater*., vol. 49, no. 12, pp. 3443-345, 2001.

[19] X. J. Jiang et al., "Differential scanning calorimetry and electron diffraction investigation on low-temperature aging in Al-Zn-Mg alloys," *Metall. Mater. Trans. A*, vol. 31, pp. 339-348, 2000.

[20] M. Song and K. Chen, "Effects of the enhanced heat treatment on the mechanical properties and stress corrosion behavior of an Al–Zn–Mg alloy," *J. Mater. Sci*., vol. 43, pp. 5265–5273, 2008.

[21] ASM handbook, vol. 4, ASM Inter., USA, 1991.

[22] A. K. Mukhopadhyay, "Microstructure and properties of high strength aluminium alloys for structural applications," *Trans. Indian Inst. Met.*, vol. 62, pp. 113-122, 2009.

[23] ASM handbook, vol.2, ASM Inter., USA, 1991.

[24] S. Chantaramanee, "A Study on Creep Behavior of Aluminum Alloy Used for Making Plastic-Injection Mold," M.S. Thesis, Dept. Mining Mater. Eng., Prince of Songkla Univ., Hat Yai, Thailand, 2006.

[25] S. A. Jenabali Jahromi, "Creep behavior of spray-cast 7XXX aluminum alloy," *Mater. Design*. vol. 23, pp. 169-172, 2002.

[26] H. Burt and B. Wilshire, "Theoretical and Practical Implications of Creep Curve Shape Analyses for 7010 and 7075," *Metall. Mater. Trans*., vol. 37A, pp. 1005-1015, 2006.

[27] R. W. Evans and B. Wilshire, *Introduction to creep*, London : Bourne Press, 1993.

[28] C. G. McKamey and P.J. Maziasz, "Heat treatment effects for improved creep-rupture resistance of a Fe_3Al-based alloy," *Intermetallics*, vol. 6, pp. 303-314, 1998.

[29] X. D. Du, "Study on ageing and creep of Al–0.1Zr alloy," *Mater. Sci. Eng. A*, vol. 432, pp. 84–89, 2006.

[29] V. Srivastava et al., "Low stress creep behaviour of 7075 high strength aluminium alloy," *Mater. Sci. Eng. A*, vol. 382, pp. 50-56, 2004.

[30] D. Y. Lee et al., "High-temperature properties of dispersion-strengthened 7075-T6 aluminium alloy," *J. Mater. Sci. Letters*., vol. 16, pp. 158-160, 1997.

[31] J. G. Park, D.Y. Lee, J. Choi, "Static creep behaviour of Al-Zn-Mg and Al-Zn-Mg-Cu alloys," *J. Mater.Sci.*, vol. 31, pp. 2719-2723, 1996.

[32] A. Yousefiani et al., "Creep Rupture Mechanisms in Annealed and Overheated 7075 Al under Multiaxial Stress States," *Metall. Mater. Trans*., vol. 31A, pp. 2807-2821, 2008.

[33] I. J. Polmear, *Light Alloy : from traditional alloys to nanocrytals*. United Kingdom. Butterworth-Heinemann, 2006, pp. 29-90.

[34] ASM Specialty Handbook. Vol.2, ASM International, USA, 1993.

[35] N. Q. Chinh et al.,"The effect of Cu on mechanical and precipitation properties of Al–Zn–Mg alloys," *J. Alloy. Compd*., vol. 378, pp. 52–60, 2004.

[36] J. Soto et al., "Distribution and prediction of solute in Al–Zn–Mg alloys," *Mater. Sci. Eng. A*, vol. 408, pp. 303–308, 2005.

[37] X. G. Fan et al., "Evolution of eutectic structures in Al-Zn-Mg-Cu alloys during heat treatment," *Trans. Nonferrous Met. SOC. China*, Vol. 16, pp. 577-581, 2006.

[38] T. S. James and R.S. Ralph, "Aging Process for 7000 series Aluminum Base Alloy," US patent 4 431 467, 1984.

[39] D. Godard et al., "Precipitation sequences during quenching of the AA 7010 alloy," *Acta Mater*., vol. 50, pp. 2319–2329, 2002.

[40] F. Vianaa et at., "Retrogression and re-ageing of 7075 aluminium alloy: microstructural characterization," *J. Mater. Proc. Technol*. vol. 92-93, pp. 54-59, 1999.

[41] L. Xi Wu et al., "Effect of one-step aging on microstructure and properties of a novel Al-Zn-Mg-Cu-Zr alloy," *Sci. China Ser. E*., vol. 1, pp. 67-71, 2009.

[42] T. Engdahl et al., "Investigation of fine scale precipitates in Al–Zn–Mg alloys after various heat treatments," *Mater. Sci. Eng. A*, vol. 327, pp. 59–64, 2002.

[43] L. Zhihui et al., " Investigation of microstructural evolution and mechanical properties during two-step ageing treatment at 115 and 160 °C in an Al–Zn–Mg–Cu alloy pre-stretched thick plate," *Mater. Charact.*, vol. 59, pp. 278-282, 2008.

[44] S. P. Ringer and K. Hono, "Microstructural evolution and age hardening in aluminium alloys: atom probe field-ion microscopy and transmission electron microscopy studies," *Mater. Charact*., vol. 44, pp. 101-131, 2000.

[45] L. B. Ber, "Accelerated artificial ageing regimes of commercial aluminiu alloys. II: Al–Cu, Al–Zn–Mg–(Cu), Al–Mg–Si–(Cu) alloys, " *Mater. Sci. Eng. A,* vol. 280, pp. 91–96, 2000.

[46] M. E. Kassner and M. T. Perez-Prado, *Fundamentals of Creep in Metals and Alloy*, San Diego: Elsevier, 2004.

[47] M. E. Van Dalen et al., "Microstructural evolution and creep properties of precipitation-strengthened Al–0.06Sc–0.02Gd and Al–0.06Sc–0.02Yb (at.%) alloys," *Acta Mater*., vol. 59, pp. 5224–5237, 2011.

[48] J. Lapin, "High temperature creep of precipitation-strengthened Ni_3Al-based alloy," *Intermetallics*, vol. 7, pp. 599-609, 1999.

[49] M. E. Kassner and T. A. Hayes, "Creep cavitation in metals," *Int. J. Plasticity*, vol. 19, pp. 1715–1748, 2003.

[50] T. Rattanochaikul et al., "Development of aluminum rheo-extrusion process using semi-solid slurry at low solid fraction," Trans. Nonferrous Met. Soc. China, vol. 20, pp. 1763-1768, 2010.

[51] *Rockwell hardness and rockwell superficial hardness of metallic materials*, ASTM E18-03, 2004.

[52] *Tension testing wrought and cast aluminum and magnesium alloy products*, ASTM B 557M-02[a], 2003.

[53] Y. Zhou, "Study on creep behavior of semi-solid A356 alloy produced by the GISS process," M.S. Thesis, Dept. Mining Mater. Eng., Prince of Songkla Univ., Hat Yai, Thailand, 2011.

[54] Y. L. Deng et al., "Microstructural evolution of Al–Zn–Mg–Cu alloy during homogenization," *J. Mater. Sci.*, vol. 46, pp. 875-881, 2010.

[55] A. R. Eivani et al., "Evolution of grain boundary phases during the homogenization of AA7020 aluminum alloy," *Metall. Mater. Trans. A*, vol. 40A, pp. 717-728, 2009.

[56] X. Fan et al., "The microstructural evolution of an Al–Zn–Mg–Cu alloy during homogenization," *Mater. Letters*, vol. 60, pp. 1475–1479, 2006.

[57] X. M. Li and M. J. Starink, "The effect of compositional variations on the characteristics of coarse intermetallic particles in overaged 7xxx Al alloys," *Mater. Sci. Technol*., vol. 17, pp. 1324-28, 2001.

[58] Y. L. Deng et al. (2012, August 24). *Microstructural evolution of Al–Zn–Mg–Cu alloy during homogenization* [online]. DOI : 10.1007/s10853-010-4828-2.

[59] Z. H. Li et al., "Microstructural evolution of aluminum alloy 7B04 thick plate by various thermal treatments," *Trans. Nonferrous Met. Soc. China*, vol. 18, pp. 40-45, 2008.

[60] N. M. Doroshenko et al., "Effect of admixtures of iron and silicon on the structure and cracking of near-edge volumes in rolling of large flat ingots from alloy 7075," *Met. Sci. Heat Treat*., vol. 47, no. 1-2, pp. 30-35, 2005.

[61] K. Chen et al., "The improvement of constituent dissolution and mechanical properties of 7055 aluminum alloy by stepped heat treatments," *J. Mater. Process.Technol*., vol. 142, pp. 190-196, 2003.

[62] W. Tao et al., "Effect of homogenization treatment on microstructure and hot workability of high strength 7B04 aluminium alloy," *Trans. Nonferrous Met. Soc. China*, vol. 17, pp. 548-552, 2007.

[63] Y. H. Han, "Effect of intermetallic phases on the mechanical properties of cast A356 alloy wheels," in *The 1st International Forum on Strategic Technology Conf*., 2006, pp. 338-341.

[64] Z. Li et al., "Ageing behavior of an Al-Zn-Mg-Cu alloy pre-stretched thick plate," *J. Uni. Sci. and Technol. Beijing*, vol. 14, pp. 246-250, 2007.

[65] Z. M. El-Baradie and M. El-Sayed, "Effect of double thermomechanical treatments on the properties of 7075 A1 alloy," *J. Mater. Proc. Technol*., vol. 62, pp. 76-80, 1996.

[66] A. Deschamps et al., "Influence of predeformation on ageing in an Al-Zn-Mg alloy – I. microstructure evolution and mechanical properties," *Acta Mater*., vol. 47, pp. 281-292, 1999.

[67] A. K. Mukhopadhyay, "Development of reproducible and increased strength properties in thick extrusions of low-alloy Al-Zn-Mg-Cu based AA 7075," Metall. Mater. Trans. A, vol. 28A, pp. 2429-2433,1997.

[68] Z. W. Du et al., "Quantitative evaluation of precipitates in an Al–Zn–Mg–Cu alloy after isothermal aging," *Mater. Charact*., vol. 56, pp. 121–128, 2006.

[69] Z. Li et al., "Investigation of microstructural evolution and mechanical properties during two-step ageing treatment at 115 and 160 °C in an Al–Zn–Mg–Cu alloy pre-stretched thick plate," *Mater. Charact*., vol. 59, pp. 278-272, 2008.

[70] G. Sha and A. Cerezo, "Early-stage precipitation in Al–Zn–Mg–Cu alloy (7050)," *Acta Mater*. Vol. 52, pp. 4503–4516, 2004.

[71] K. Stiller et al., "Investigation of precipitation in an Al–Zn–Mg alloy after two-step ageing treatment at 100° and 150°C," *Mater. Sci. Eng. A*, vol. 270A, pp. 55–63, 1999.

[72] J. K. Park and A.J.Ardell, "Microstructures of Commercial 7075 Al Alloy in the T651 and T7 Tempers," *Metall. Trans. A*, vol. 14, pp. 1957-1965, 1983.

[73] M. Dumont et al., "Characterisation of the composition and volume fraction of η' and η g precipitates in an Al–Zn–Mg alloy by a combination of atom probe, small-angle X-ray scattering and transmission electron microscopy, " *Acta Mater*., vol. 53, pp. 2881–2892, 2005.

[74] H. Möller et al., "The T6 heat treatment of semi-solid metal processed alloy A356," *The Open Mater. Sci. J.*, vol. 2, pp. 6-10, 2008.

[75] C. Garcia-Cordovilla and E. Louis, "Kinetics of retrogression in Al–Zn–Mg (Cu) Alloys, " *Metall. Trans. A*, vol. 21, pp. 2277–2280, 1990.

[76] B. Wilshire and P. J. Scharning, “Creep and creep fracture of commercial aluminium alloys,” *J. Mater. Sci*., vol. 43, pp. 3992–4000, 2008.

[77] W. D. Nix, “Mechanisms and controlling factors in creep fracture,” Mater. Sci. Eng. A, vol. 103, pp. 103-110, 1988.

[78] L. Zhen and S. B. Kang, “Deformation and Fracture Behavior of Two Al-Mg-Si Alloys, ” *Metall. Mater. Trans. A*, vol. 28, pp. 1489-1497, 1997.

[79] B. Wilshire and H. Burt, “Damage evolution during creep of steels,” *Int. J. Pres. Ves. Pip*., vol. 85, pp. 47–54, 2008.

[80] H. E. Evans, *Mechanism of creep fracture*. New York : Elsevier Science, 1984.

[81] L. Engel and H. Klingele, *An atlas of metal damage*. London : Wolfe,1981.

APPENDIX

APPENDIX A

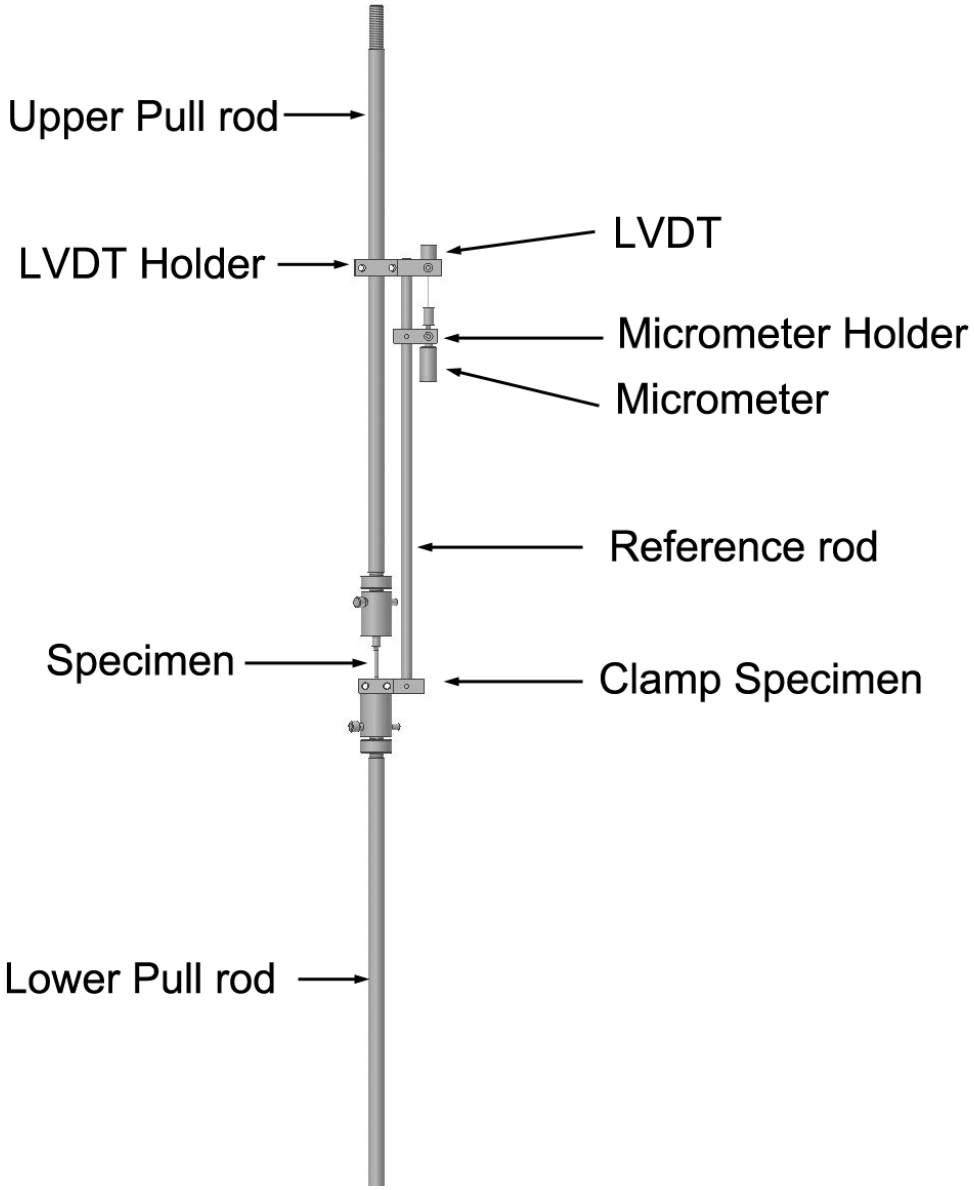

Fig. Appendix A1. Specimen and LVDT connection design.

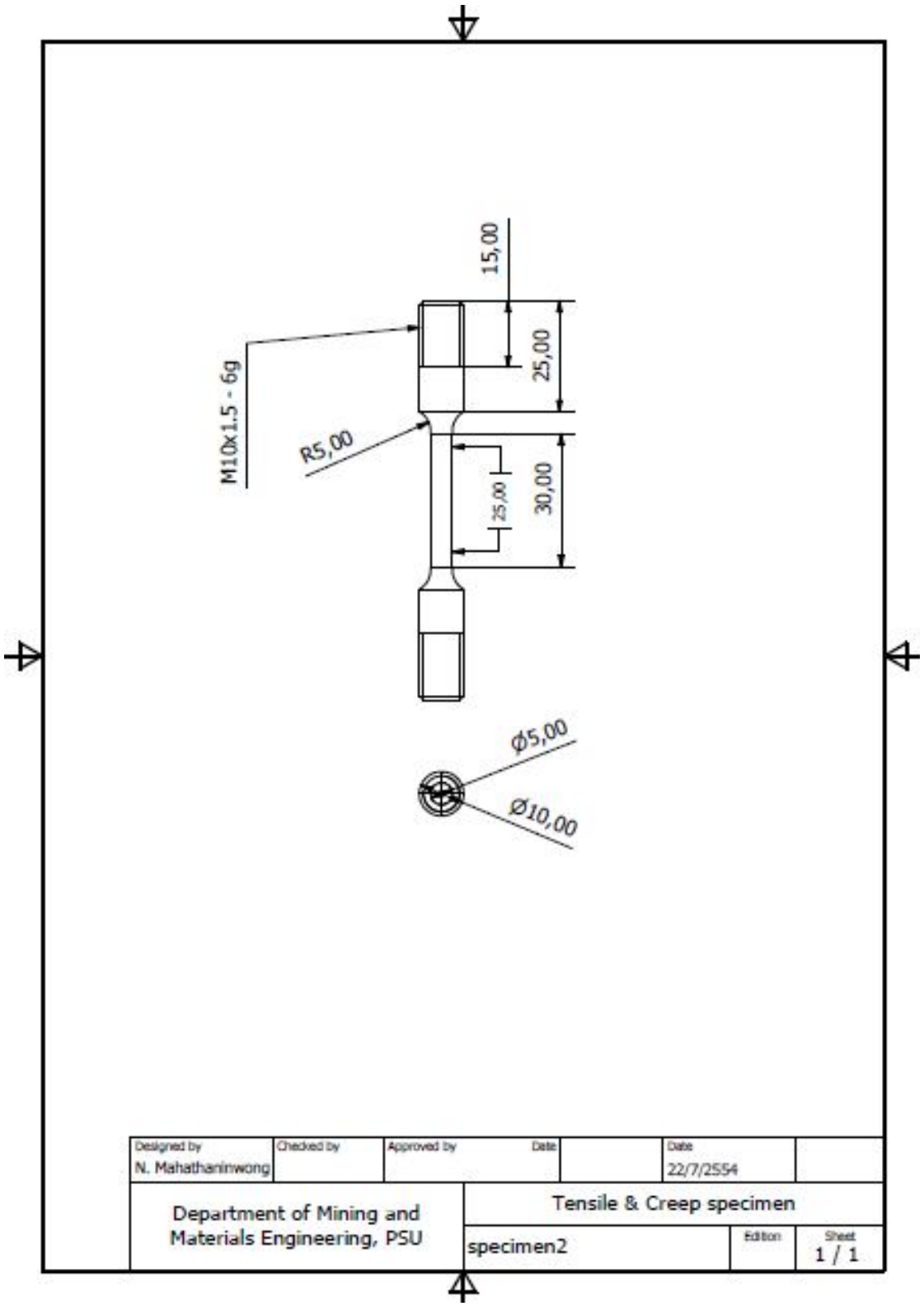
15,00
25,00
M10x1.5 - 6g
R5,00
25,00
30,00
Ø5,00
Ø10,00
Designed by
N. Mahathaninwong
Checked by
Approved by
Date
Date
22/7/2554
Department of Mining and Materials Engineering, PSU
Tensile & Creep specimen
specimen2
Edition
Sheet
1 / 1

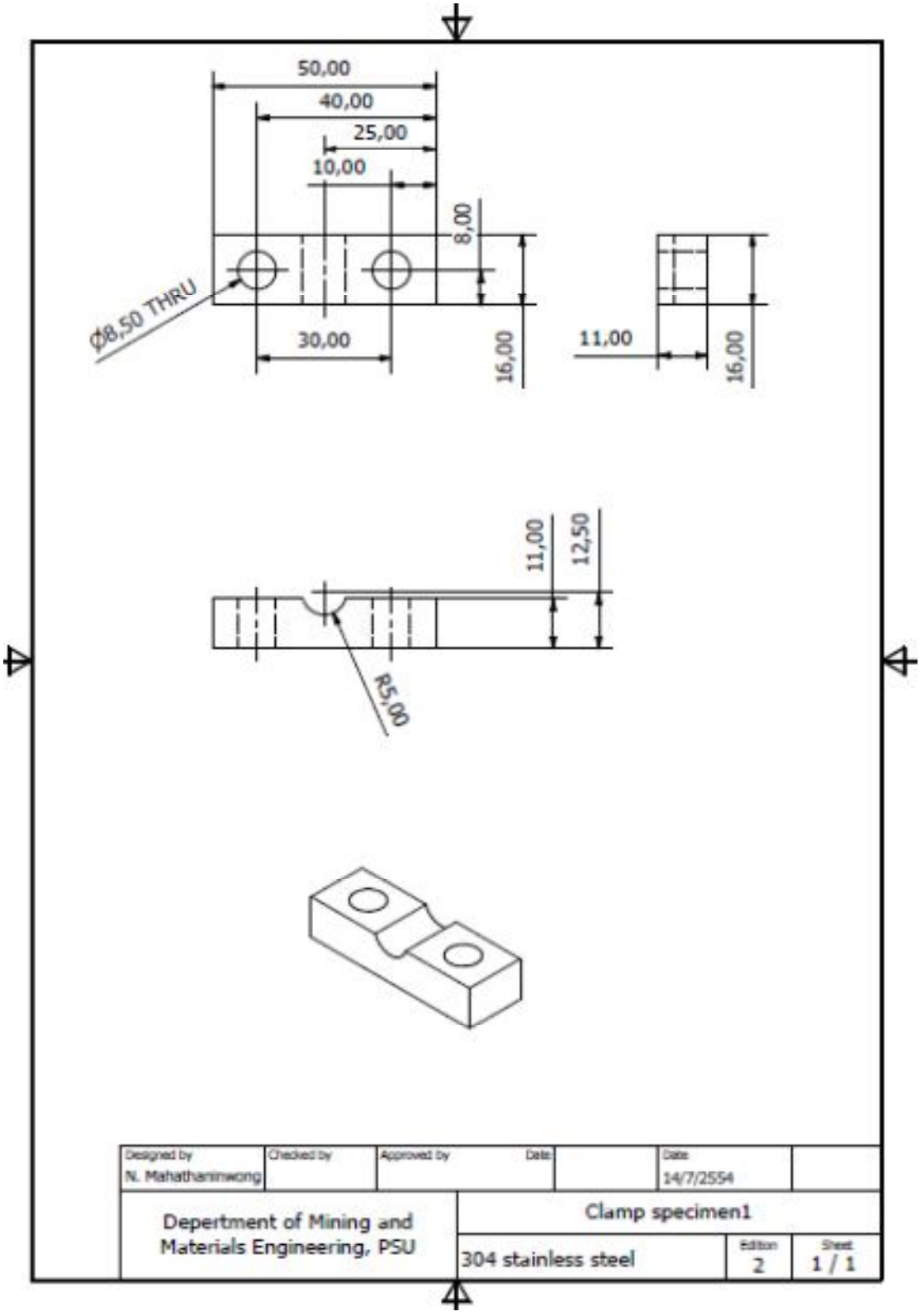
50,00
40,00
25,00
10,00
8,00
Ø8,50 THRU
30,00
16,00
11,00
16,00
11,00
12,50
R5,00
Designed by
N. Mahathaninwong
Checked by
Approved by
Date
Date
14/7/2554
Depertment of Mining and
Materials Engineering, PSU
Clamp specimen1
304 stainless steel
Edition
2
Sheet
1 / 1

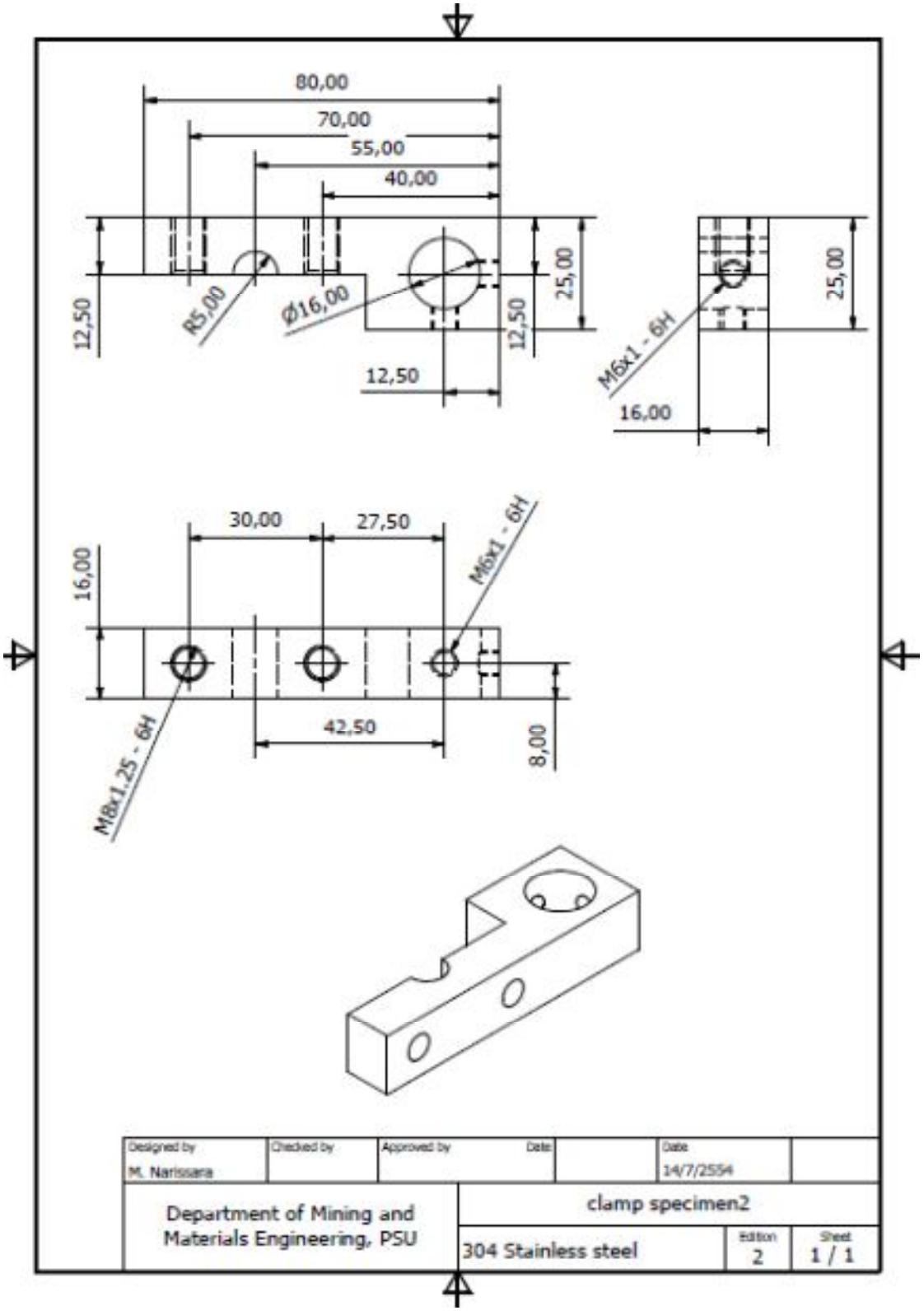
80,00
70,00
55,00
40,00
12,50
R5,00
Ø16,00
25,00
12,50
12,50
M6x1 - 6H
25,00
16,00
30,00
27,50
M6x1 - 6H
16,00
42,50
8,00
M8x1.25 - 6H
Designed by
M. Narissara
Checked by
Approved by
Date
Date
14/7/2554
Department of Mining and Materials Engineering, PSU
clamp specimen2
304 Stainless steel
Edition
2
Sheet
1 / 1

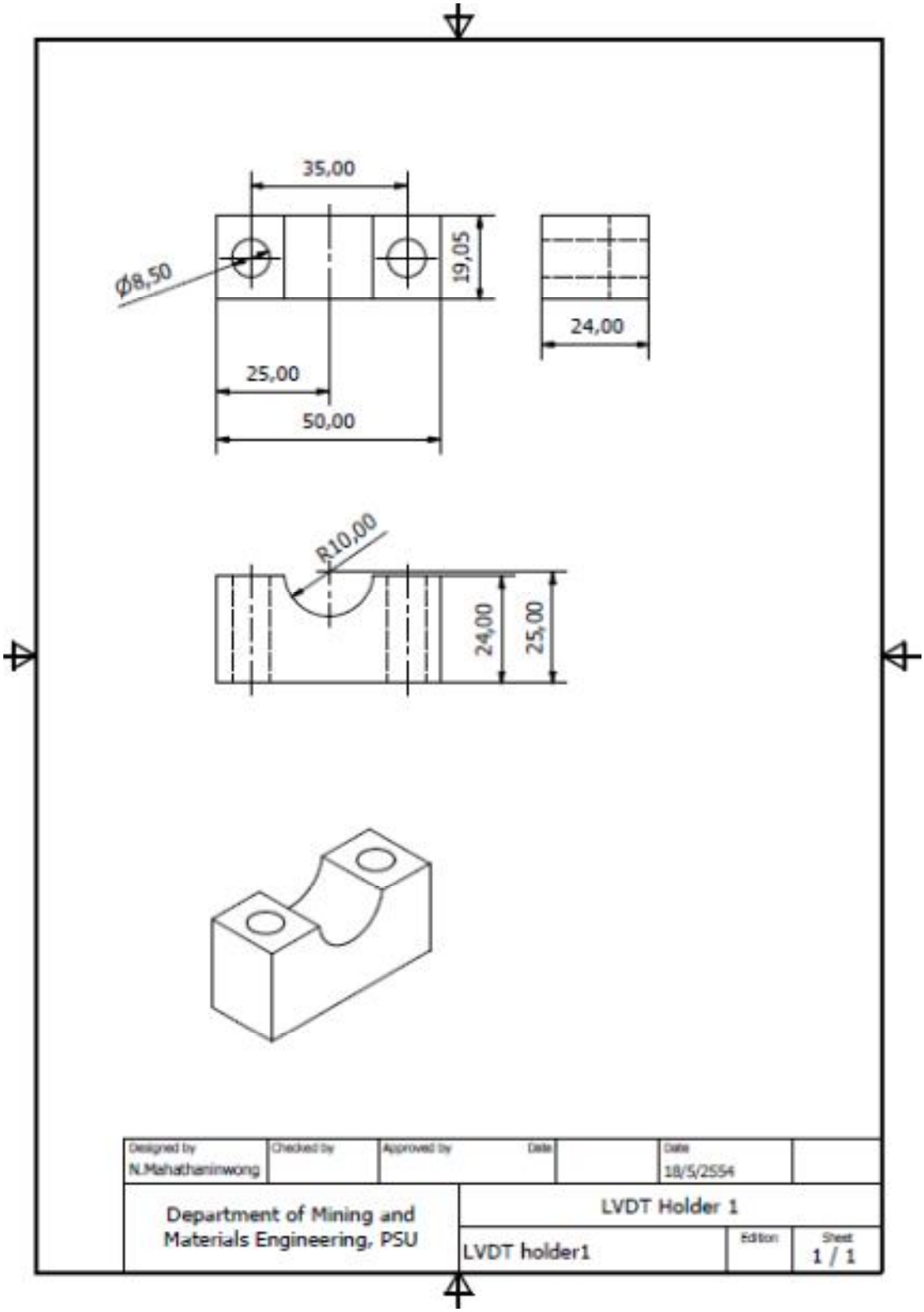
35,00
Ø8,50
19,05
24,00
25,00
50,00
R10,00
24,00
25,00
Designed by
N.Mahathaninwong
Checked by
Approved by
Date
Date
18/5/2554
Department of Mining and Materials Engineering, PSU
LVDT Holder 1
LVDT holder1
Edition
Sheet
1 / 1

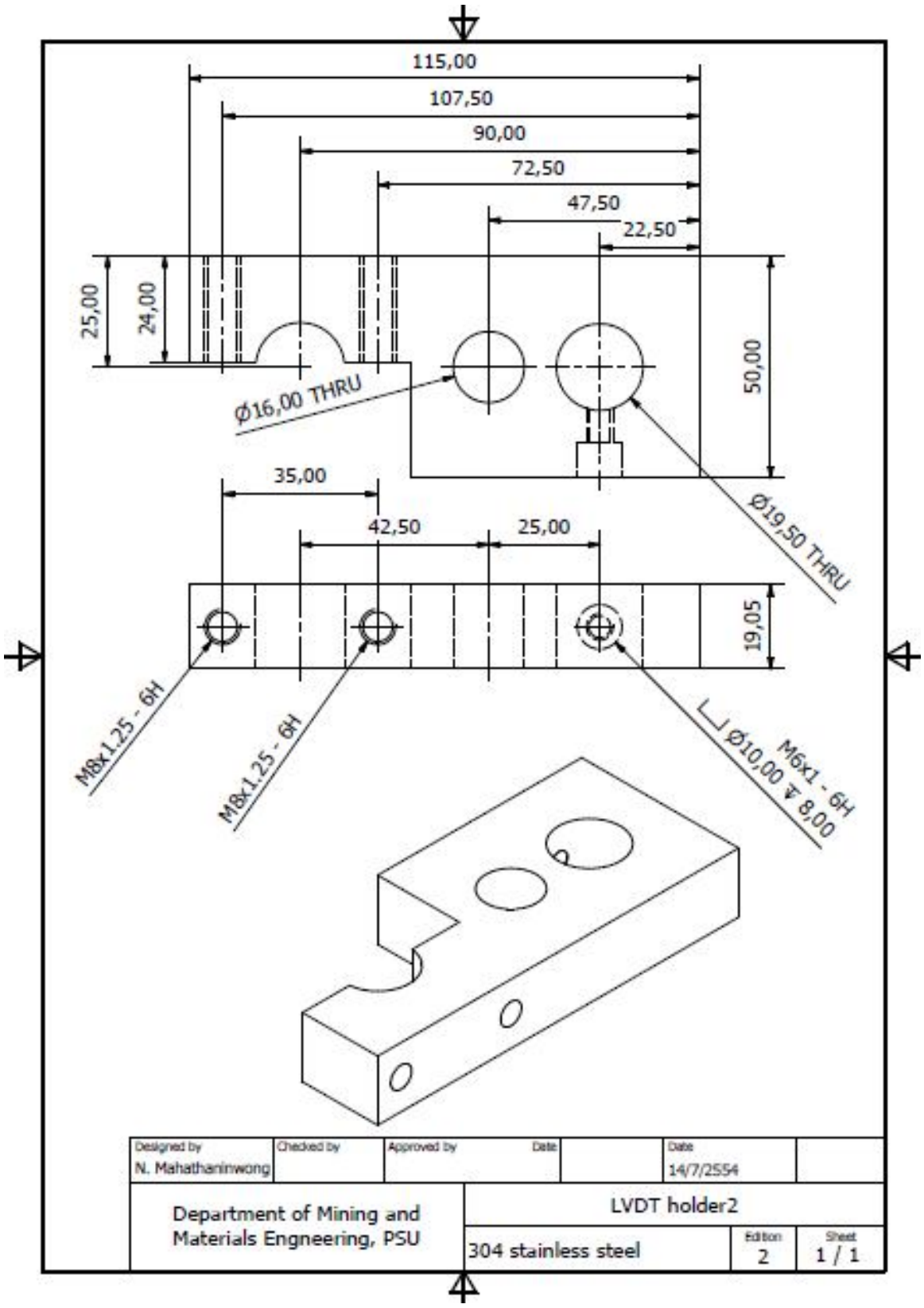
115,00
107,50
90,00
72,50
47,50
22,50
25,00
24,00
50,00
Ø16,00 THRU
Ø19,50 THRU
35,00
42,50
25,00
19,05
M8x1.25 - 6H
M8x1.25 - 6H
⌴ Ø10,00 ↧ 8,00
M6x1 - 6H
Designed by
N. Mahathaninwong
Checked by
Approved by
Date
Date
14/7/2554
Department of Mining and Materials Engneering, PSU
LVDT holder2
304 stainless steel
Edition
2
Sheet
1 / 1

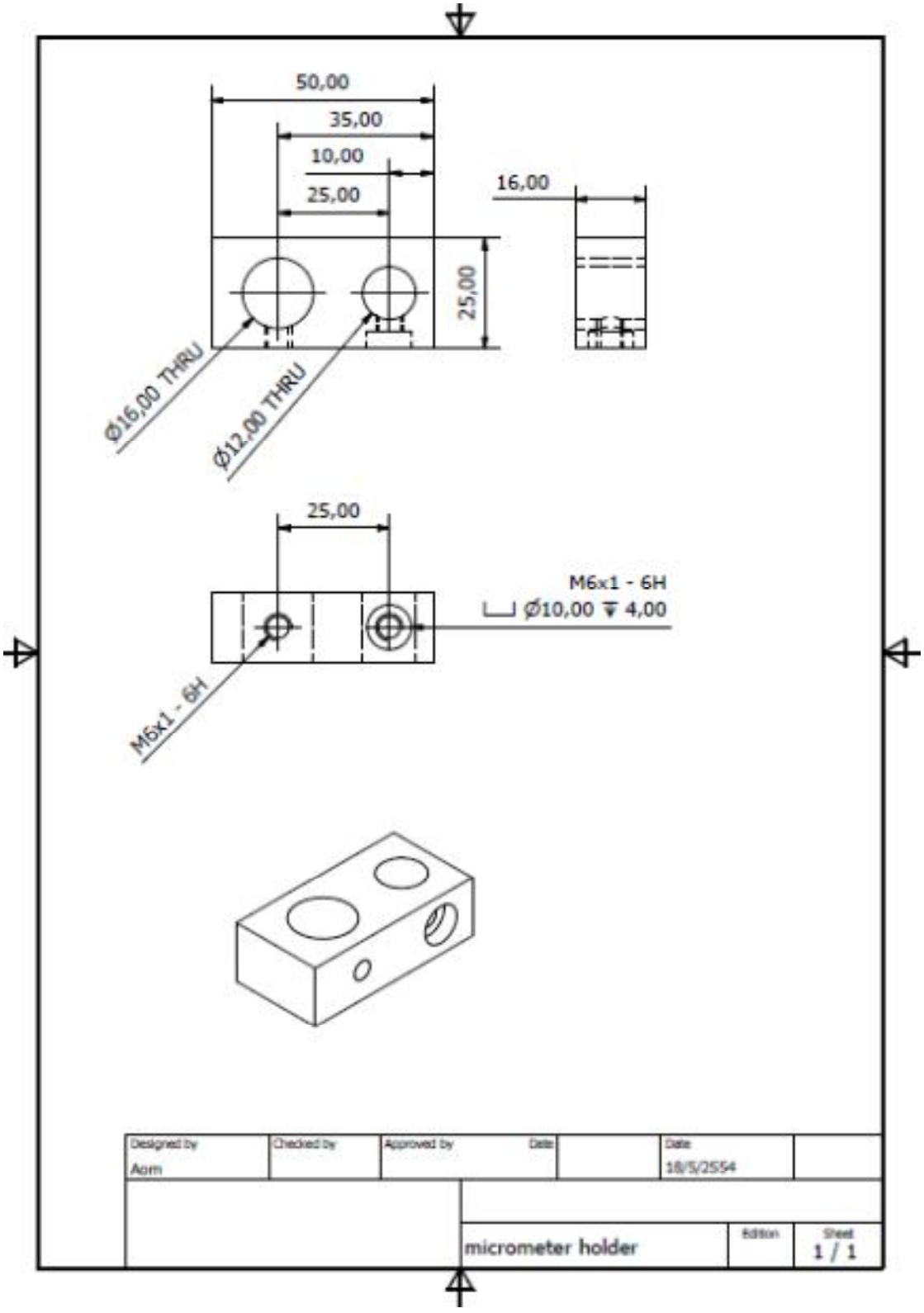
50,00
35,00
10,00
25,00
16,00
25,00
Ø16,00 THRU
Ø12,00 THRU
25,00
M6x1 - 6H
⌴ Ø10,00 ▽ 4,00
M6x1 - 6H
Designed by
Aom
Checked by
Approved by
Date
Date
18/5/2554
micrometer holder
Edition
Sheet
1 / 1

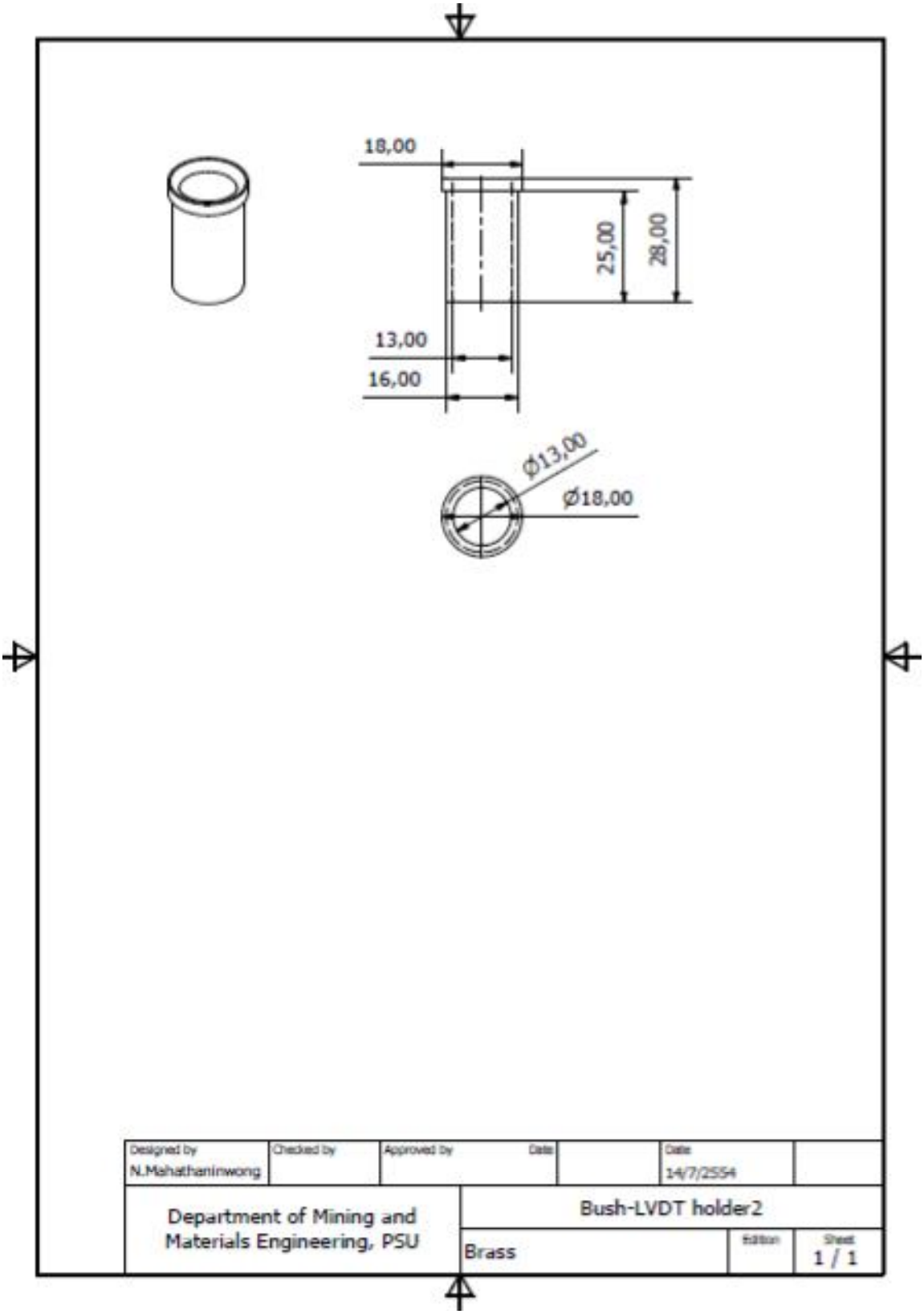
18,00
25,00
28,00
13,00
16,00
Ø13,00
Ø18,00
Designed by
N.Mahathaninwong
Checked by
Approved by
Date
Date
14/7/2554
Department of Mining and
Materials Engineering, PSU
Bush-LVDT holder2
Brass
Edition
Sheet
1 / 1

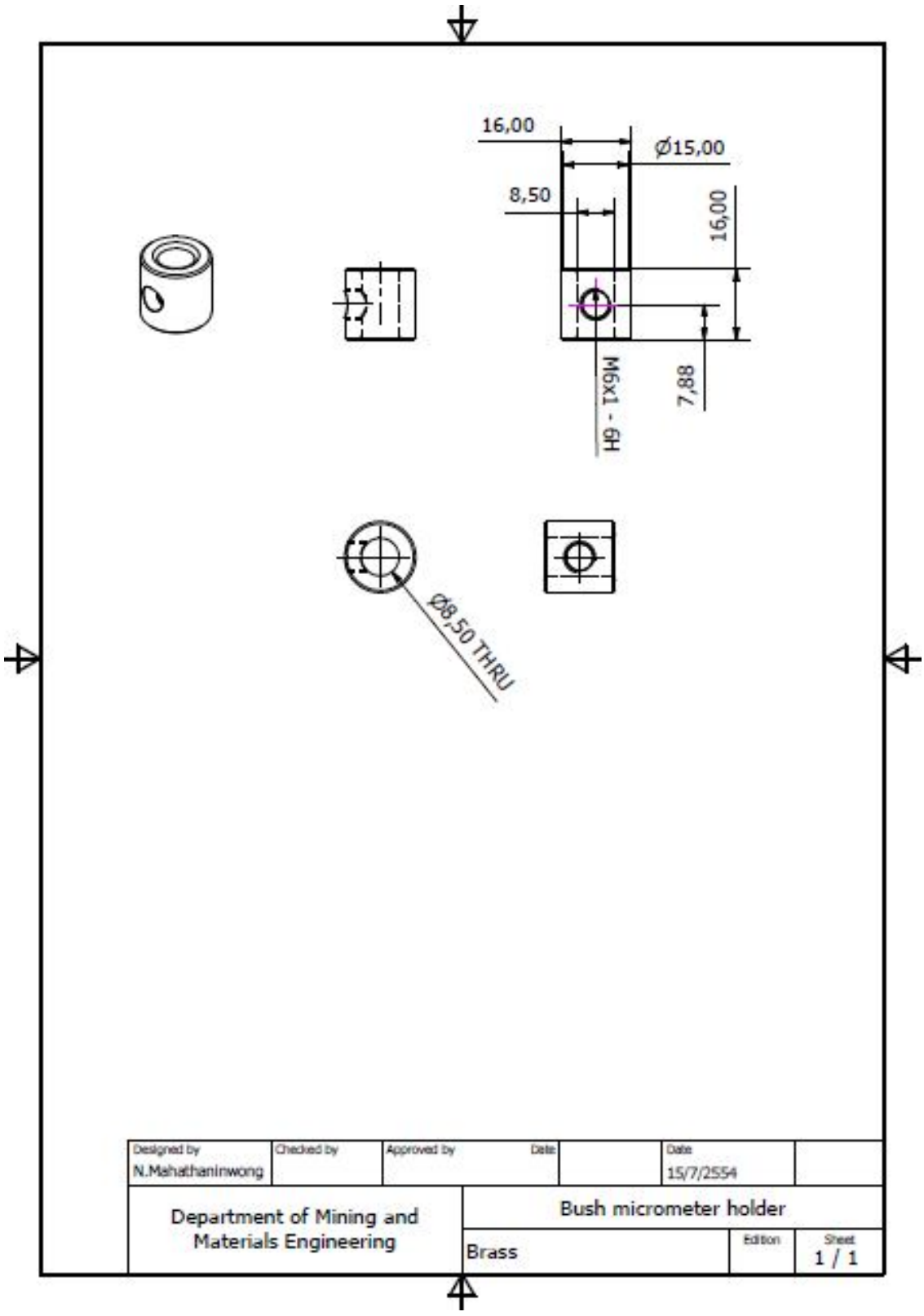

Designed by	Checked by	Approved by	Date		Date	
N.Mahathaninwong					15/7/2554	

Department of Mining and Materials Engineering	Bush micrometer holder		
	Brass	Edition	Sheet 1 / 1

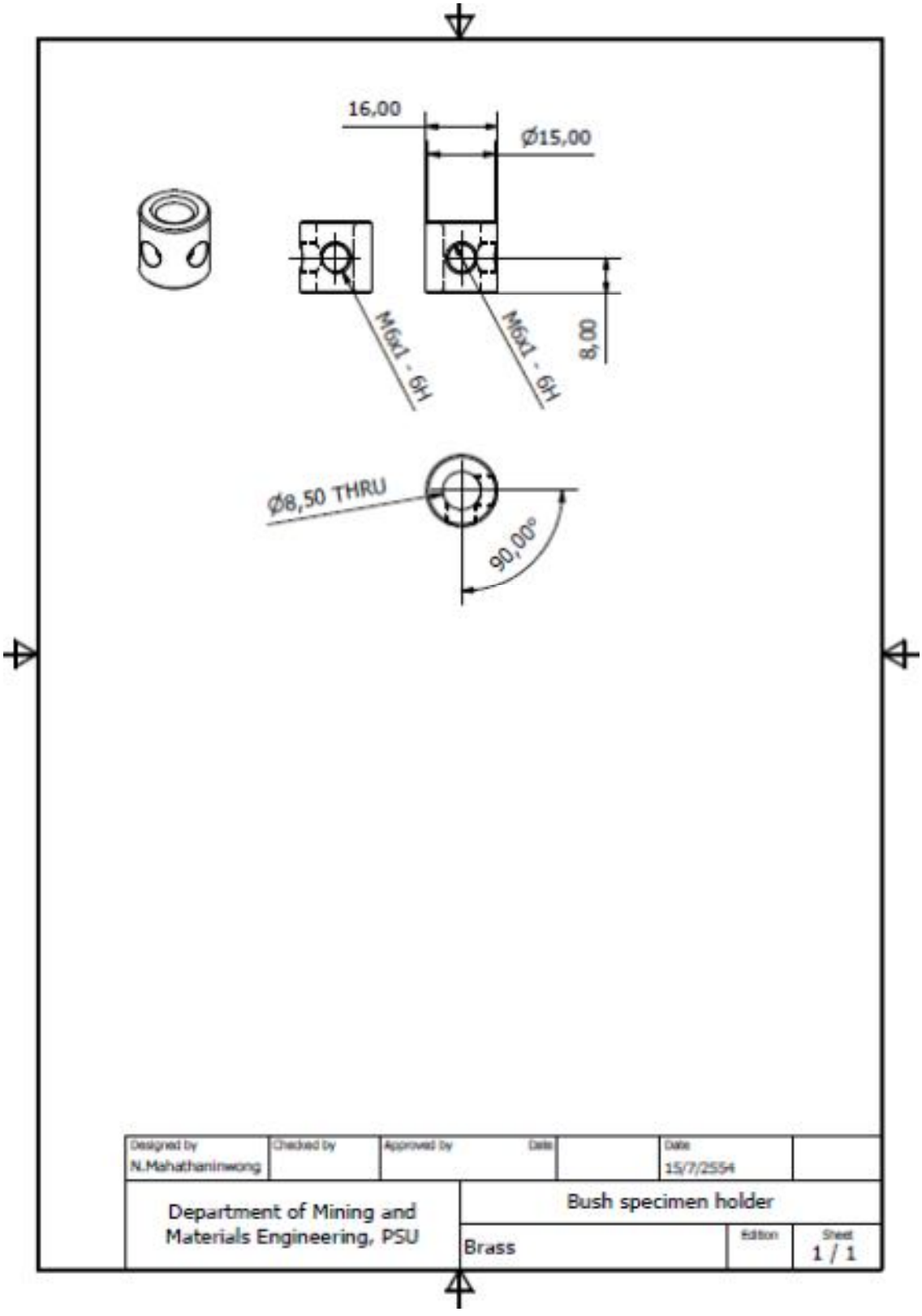
16,00
Ø15,00
M6x1 - 6H
M6x1 - 6H
8,00
Ø8,50 THRU
90,00°
Designed by
N.Mahathaninwong
Checked by
Approved by
Date
Date
15/7/2554
Department of Mining and
Materials Engineering, PSU
Bush specimen holder
Brass
Edition
Sheet
1 / 1

APPENDIX B

Advanced Materials Research Vol. 339 (2011) pp 371-374
Online available since 2011/Sep/02 at www.scientific.net

doi:10.4028/www.scientific.net/AMR.339.371

Influence of Solution Heat Treatment on Microstructures of Semisolid Cast 7075 Aluminium Alloy

Narissara Mahathaninwong [1, a], Sirikul Wisutmethangoon [2, b], Thawatchai Plookphol [1, c], Jessada Wannasin [1, d]

[1] Department of Mining and Materials Engineering, Faculty of Engineering, Prince of Songkla University, Hat Yai, Songkhla, Thailand 90112

[2] Department of Mechanical Engineering, Faculty of Engineering, Prince of Songkla University, Hat Yai, Songkhla, Thailand 90112

[a]narissara.s@psu.ac.th, [b]sirikul@me.psu.ac.th, [c]thawatchai.p@psu.ac.th, [d]jessada.w@psu.ac.th

Keyword: 7075 Al alloy; Gas Induced Semi Solid (GISS) technique; Solution heat treatment

Abstract. Influence of temperature and time of solution heat treatment on the microstructures of rheo-casting 7075 aluminium alloy produced by a novel technique, the Gas Induced Semi Solid (GISS) technique, had been investigated in this study. The microstructure of the as-cast specimens mainly consisted of matrix-α (Al) and grain boundary (GB)-eutectic phase (α-Al + $Mg(Zn,Cu,Al)_2$). After solution heat treatment at 480 °C for 1 h, $MgZn_2$ phase at the grain boundary was observed to have dissolved and coarse black particles of Mg_2Si were observed to form in the matrix. In comparison, when solutionizing temperature of 450 °C was applied, it took 4 h of solution treatment time in order to dissolve the same portion of GB phase and $MgZn_2$ phase, and coarse black particles of Mg_2Si were found to form in the 8 h solution treated sample.

Introduction

7075 aluminium alloy was developed for high strength applications such as in aircraft structures and in artificial limbs. It is a heat treatable Al-Zn-Mg-Cu alloy. T6 heat treatment has been a successful process for producing high strength alloys. It involves three main steps: solution heat treatment, quenching, and artificial aging. The solution heat treatment step aims to dissolve segregated elements and soluble phases into matrix as solid solution. However, solid solubility depends on solution treatment temperature and time. Furthermore, enhancing desirable mechanical properties can be achieved by adopting appropriate optimum condition of solution treatment temperature and time. Solution treatment temperatures of wrought 7075 Al alloy were suggested to be in the range of 465-490 °C [1]. However, Mukhopadhyay [2] advised that the temperature for the dissolving soluble phase of as-cast 7075 Al alloy should not be over 465 °C. Different production procedures thus had been advised to perform solution heat treatment at different temperature due to a variety of as-fabricated microstructures.

Currently, the Innovative Metal Technology (IMT) team at the Prince of Songkla University has developed a new technique of rheo-casting process for forming 7075 Al alloy, which is called the Gas Induced Semi-Solid (GISS) technique [3]. Heat treatment of the alloy processed by this technique has never been studied before. The present work is part of a first heat treatment study of this alloy by this process. It focuses on the influence of solution heat treatment temperature and time on the microstructure of the alloy.

Experiments

The material used in this study is a commercial 7075 aluminium alloy. As-cast specimens with dimension of 100x100x15 mm were prepared through rheo-casting employing the Gas Induced Semi-Solid (GISS) technique by introducing gas bubbles to molten 7075 aluminium alloy at temperature of 643 °C for 7 s and holding for 30 s before squeeze-casting at a pressure of approximately 80 MPa. The chemical compositions of the as-cast 7075 alloy in wt% were Al-6.08Zn-2.5Mg-1.93Cu-0.46Fe-0.4Si.

The as-cast specimens were solution treated at temperatures of 450 °C and 480 °C for 1, 4, 8, and 12 h and subsequently quenched in water at temperature of 25 °C. Microstructure characteristics were studied employing a combination of optical microscopy (OM), JSM-5800LV JEOL scanning electron microscopy (SEM) equipped with energy dispersive X-ray spectrometry (EDS) and X'Pert MPD Philips X-ray diffraction (XRD). For optical and scanning electron examinations, the specimens were ground, polished, then etched with 0.5%HF reagent for up to 5 seconds before rinsing by distilled water.

Results and Discussion

Microstructure of the as-cast specimens

Secondary electron images of as-cast microstructures reveal a non-dendritic grain structure and a white contrast of grain boundary (GB) phases as shown in Fig. 1. A high magnification image of GB phases in Fig.1(b) presents large bright areas and elongated black areas at grain boundaries of matrix-α (Al). The SEM-EDS point analysis of the bright areas at grain boundaries shows high concentrations of Zn, Mg, and Cu elements because of solute segregation during casting, as illustrated in Fig.1(c). One previous investigation [4] referred that if Zn/Mg ratio of Al-Zn-Mg-Cu alloy is more than 2.2, the dominant second phase in the solidification eutectic should be the $MgZn_2$ phase. In this research, Zn/Mg ratio of the alloy is 2.4. In addition, the XRD result of the as-cast specimens mainly consists of α-Al and η-$MgZn_2$ as shown in Fig. 2. Therefore, most of bright GB phases should be quaternary $Mg(Zn,Cu,Al)_2$ phase in that some Al and Cu atoms have dissolved in the η-phase and form the same crystallographic lattice constant as $MgZn_2$, as reported by Deng et.al [4]. The EDS result shown in Fig. 1(d) indicates that the elongated black area at the grain boundary in Fig. 1(b) is Mg_2Si phase. However, the existence of this small amount of Mg_2Si cannot be verified by the XRD test.

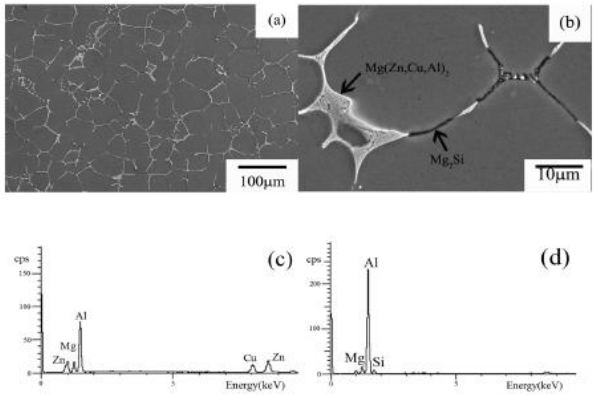

Fig. 1. SEM micrographs of (a)-(b) as-cast semi-solid 7075 Al alloy (c) EDS result of bright area and (d) EDS result of elongated black area.

Microstructure of solution treated specimen

Area fractions of the remaining grain boundary phases in the solution treated samples were quantitatively analyzed and illustrated in Fig. 3. It is observed from Fig. 3 that the remaining GB phases sharply decreased in the first hour of solution treated temperatures at 450 °C and 480 °C. However, the area fraction of the GB phase in the sample solution treatment at 480 °C remained almost constant when the solution treatment time is longer than 1 h; indicating that this phase may be completely or almost dissolved within the first hour of solution treatment at 480 °C. This result was confirmed by the XRD result showing the disappearance of η-$MgZn_2$ phase in Fig. 2. On the other hand, solution treating of the sample at 450 °C for 1 h was not enough to allow diffusion to establish an equilibrium solid solution since the major second phase of $Mg(Zn,Cu,Al)_2$ was not completely dissolved as indicated by XRD, OM and SEM-EDS results shown in Fig. 2, Fig. 4(b),

and Fig. 5(a)-5(b), respectively. Hence, the area fraction of the GB phase in the sample solution treated at 450 °C continued to decrease for further solution treating until complete dissolution was met at the solution treating time of 4 h leading to the disappearance of η-$MgZn_2$ phase in the XRD result as shown in Fig. 2.

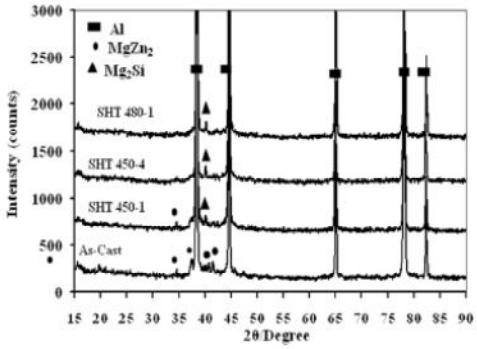

Fig. 2. XRD results of as-cast and solution heat treated (SHT) samples (SHT 450-1: 450 °C/1 h, SHT 450-4: 450 °C/4 h, SHT 480-1: 480 °C/1 h).

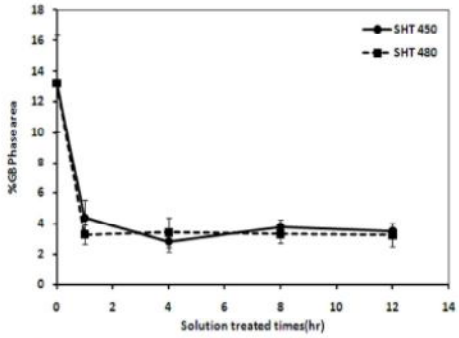

Fig. 3. Area fractions of GB phases after solution heat treatment at 450 °C and 480 °C at various holding times.

The evolution of GB phases after solution heat treatment at various conditions is shown in Fig. 4. The mechanism for evolution of GB phases during heat treatment has been proposed in three stages: thinning, discontinuation, and dissolution [5]. In this research, spatially continuous GB phases of as-cast specimens were subsequently dissolved after solution heat treatment at either temperature. The discontinuation stage could be more notably observed than other stages.

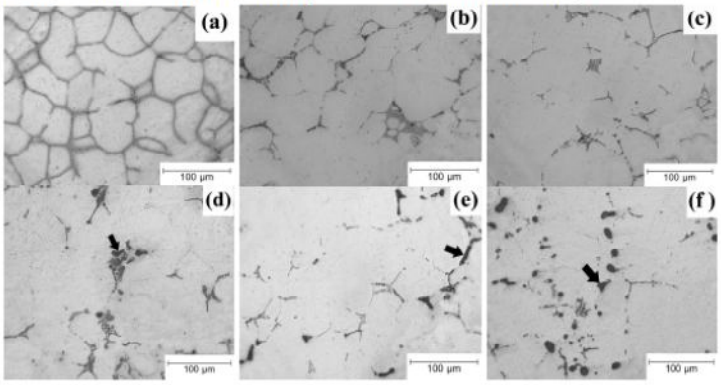

Fig. 4. Optical micrographs of (a) as-cast (b) SHT 450 °C/1h (c) SHT 450 °C/4h (d) SHT 450 °C/8h (e) SHT480 °C/1h, and (f) SHT 480 °C/8h specimens.

In addition, coarse black particles were found to form after solution heat treatment at 450 °C for 8 h and at 480°C for 1 h, as pointed out by the black arrows in Fig. 4(d) and 4(e), respectively. The number of these particles increased with increasing solution treatment time from 1 h to 8 h at 480 °C as shown in Fig. 4(e) and Fig. 4(f). Chena et al [6] identified the coarse black particles to be melted constituents due to homogenization at high temperature. Fig. 6 shows the elemental mapping results of a black constituent particle in the sample solution treated for 1 h at 480 °C; revealing that this particle could be an incipient melting of low melting point $Mg(Zn,Cu,Al)_2$ phase in multinary eutectic area. Owing to high diffusion coefficients of Zn, these atoms would easily diffuse throughout the matrix as solid solution, leaving behind the segregated sluggish silicon atoms to form overheated Mg_2Si particles during quenching. Formation of the Mg_2Si overheated particles was confirmed by the XRD result as shown in Fig. 2 and was found to be undesirable because it

would reduce toughness and aging response due to the lower supersaturated solid solution remaining in the solution treated sample. Other GB phases observed in the 1 h solution treated samples at 450 ^{o}C are depicted in Fig. 5(c) and 5(e), having skeleton shape and elongated black shape, respectively. These two phases were also found in other solution treated samples. The EDS results of a skeleton particle and an elongated black area are given in Fig. 5(d) and Fig. 5(f), respectively, and were identified as Cu_2FeAl_7 phase and Mg_2Si phase, respectively, as reported by Doroshenko et al[7]. The presence of a small amount of the Cu_2FeAl_7 phase could not be verified by the XRD results, but the Mg_2Si phase could be determined by XRD as indicated in Fig. 2.

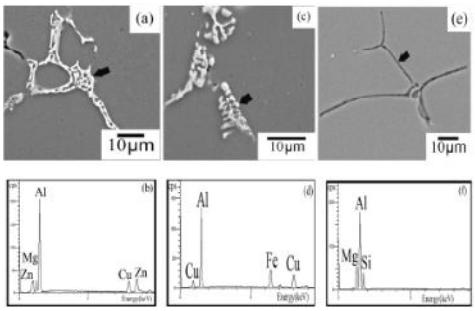

Fig. 5. (a), (c), (e) SEM micrographs and (b), (d), (f) EDS results of remaining GB phases after solution heat treatment at 450 ^{o}C for 1 h.

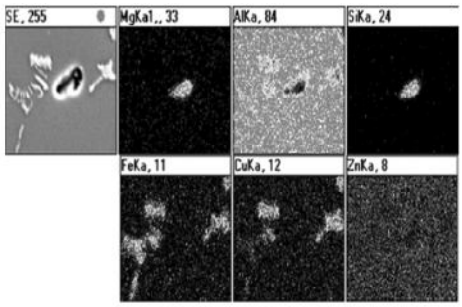

Fig. 6. Elemental mapping of constituent particles in the sample solution heat treated at 480 ^{o}C for 1h.

Conclusions

From the above study and experimental results it can be concluded that as-cast samples consist of two main phases: a non-dendritic grain structure of α-Al phase and grain boundary eutectic phase (α-Al+ $Mg(Zn,Cu,Al)_2$). The eutectic phases dissolved after solution heat treatment for 1 h at 480 ^{o}C, and for 4 h at 450 ^{o}C. Coarse black particles of Mg_2Si initially appeared after being solution heat treated for 1 h at 480 ^{o}C, and for 8 h at 450 ^{o}C. The remaining GB phases of elongated Mg_2Si phase and Cu_2FeAl_7 phase were found in microstructure of the alloy after solution heat treatment at either temperature for various holding times. The optimum solution heat treatment condition derived from this study was thus 4 h at 450 ^{o}C.

Acknowledgements

The authors would like to thank the Prince of Songkla University for the Ph.D 50% scholarship financial support, as well as supports from the National Research University Project of Thailand's Office of the Higher Education Commission (Grant No.ENG540551c), the Thailand Research Fund through the Royal Golden Jubilee Ph.D. Program (Grant No.PHD/0031/2552), and the Office of National Research Council of Thailand through Development of High-Quality and Low-Cost Below Knee Prosthesis project. In addition, we would like to thank the PSU Department of Mining and Materials Engineering for laboratory facilities.

References

[1] C.R. Brooks, Principles of heat treating of nonferrous alloys, in : S.M. Copley, E.L. Langer, ASM handbook: Heat treating ,Vol.4, ASM International, USA, 1991, pp. 1876-1879.
[2] A. K. Mukhopadhyay, Trans. Indian Inst. Met. 62 (2009) 113-122.
[3] J. Wannasin, S. Janudom, T. Rattanochaikul, R. Canyook, R. Burapa, T. Chucheep and S. Thanabumrungkul, Trans. Nonferr. Met. Soc. China. 20 (2010) s1010-s1015.
[4] Y-L.Deng, L.Wan, L.-H.Wu, Y.-Y.Zhang, X.-M.Zhang, J. Mater. Sci. 46 (2010) 875-881.
[5] A. R. Eivani, H. Ahmed, J. Zhou, J. Duszczyk, Metall. Mater. Trans. A. 40A (2009) 717-728.
[6] K.Chena, H.Liu, Z.Zhang, S.Li, R.I.Todd, J. Mater. Process.Technol. 142 (2003) 190-196.
[7] N. M. Doroshenko, B. V. Ovsyannikov, V. M. Zamyatin, V. I. Popov, Met. Sci. Heat Treat. 47 (2005) 30-35.

APPENDIX C

Materials Science and Engineering A 532 (2012) 91–99

Contents lists available at SciVerse ScienceDirect

Materials Science and Engineering A

journal homepage: www.elsevier.com/locate/msea

T6 heat treatment of rheocasting 7075 Al alloy

N. Mahathaninwong[a], T. Plookphol[a], J. Wannasin[a], S. Wisutmethangoon[b,*]

[a] Department of Mining and Materials Engineering, Faculty of Engineering, Prince of Songkla University, Hat Yai, Songkhla 90112, Thailand
[b] Department of Mechanical Engineering, Faculty of Engineering, Prince of Songkla University, Hat Yai, Songkhla 90112, Thailand

ARTICLE INFO

Article history:
Received 15 August 2011
Accepted 13 October 2011
Available online 25 October 2011

Keywords:
7075 Al alloy
Gas Induced Semi-Solid
Rheocasting
T6 heat treatment
Aged hardening
Transmission electron microscopy

ABSTRACT

Effects of solution heat treatment and age hardening on the microstructures and mechanical properties of rheocasting 7075 Al alloy produced by a novel technique, Gas Induced Semi-Solid (GISS) technique, were studied. This work reveals that the optimum solution heat treatment condition for the non-dendritic structured 7075 aluminium alloy was 450 °C for 4 h. Age hardening was performed at temperatures of 120 °C, 145 °C, 165 °C, and 185 °C under various time durations. The peak aging condition was the artificial aging at 120 °C for 72 h, at which a highest tensile strength of 486 MPa with 2% elongation was recorded. This higher strength was caused by higher number density and finer precipitate size of η′ phase than other aging temperatures. The main hardening phase was identified to be the η′ phase while early nucleation of η phase in the higher aging temperature specimens resulted in lower strengths of the alloy. The activation energy for the precipitate hardening process of the alloy derived in this research was 95,827 J/mol.

1. Introduction

7075 Aluminium alloy was developed over 70 years ago. However, many researches still have been performed on it in the past decade [1–11]. High strength and light weight properties of the alloy are attractive properties leading to its prevalent usage in transport applications corresponding to constantly increasing global warming concerns. In addition, 7075 Al alloy is being put into lightweight components of lower limb prostheses [12].

7075 Aluminium alloy was commonly formed by wrought manufacturing process which resulted in high strength. However, the cost of this production route is very high compared to the alternative casting route. Nevertheless, disadvantages of conventional casting are found in the material structure with existence of casting defects such as pores and shrinkage cavities, including lower strength [1,13]. An alternative Semi-Solid Metal (SSM) process was developed in early 1971 [14]. Reduction in casting temperature and solidification shrinkage is its main advantage [15]. This SSM process has since been developed into thixocasting and rheocasting processes.

Rheocasting process has increasingly gained attentions from many researchers because of less investment and lower raw material cost compared to thixocasting process. Hence, rheocasting process will be the alternative process to obtain higher strength alloys than cast alloy requirements. Various techniques for semisolid slurry preparations of 7075 Al alloy had been proposed such as cooling slope [3], induction stirring with simultaneous forced air cooling [16], and a novel technique of rheocasting process developed by the Innovative Metal Technology (IMT) team of the Prince of Songkla University. This technique is called Gas Induced Semi-Solid (GISS) technique [12]. It is a simple, economical and efficient process. Additionally, this technique has succeeded to produce non-dendritic structure of 7075 alloy.

However, in order to obtain high strength 7075 Al alloy, heat treatment is a key process to improve mechanical properties after the forming process. T6 heat treatment is one of the major factors to enhance mechanical properties of the alloy through an optimization of both the solution heat treatment and the artificial aging conditions applied to the alloy [5,17]. T6 heat treatment schedule of wrought 7075 Al alloy were well established at the solution temperature range of 465–490 °C and aging temperature of 120 °C [18]. In contrast, dissolving soluble phases of the as-cast 7075 Al alloy should be done at temperature lower than 465 °C as advised by Mukhopadhyay [19]. Moreover, various aging times at 120 °C for 7075 Al alloy have been proposed to be the peak-aged condition of T6 heat treatment [10,11].

As the difference in as-fabricated microstructures led to the differences in solution heat treatment and artificial aging conditions, this work hence aims to establish T6 heat treatment data of the 7075 Al alloy produced by rheocasting process along with a GISS technique. This is focused into two main sections of T6 heat treatment; solution heat treatment and artificial aging. The influence of solution heat treatment and artificial aging temperature and time on mechanical properties and microstructures was investigated.

* Corresponding author. Tel.: +66 81 6781243; fax: +66 87 4287195.
E-mail address: sirikul@me.psu.ac.th (S. Wisutmethangoon).

0921-5093/$ – see front matter © 2011 Elsevier B.V. All rights reserved.
doi:10.1016/j.msea.2011.10.068

2. Experimental methods

The alloy was prepared through rheocasting using GISS technique by introducing gas bubbles to the molten alloy at a temperature of 643 °C for 7 s and holding it for 30 s before squeeze-casting at a pressure of approximately 80 MPa. The as-cast dimensions were 100 mm × 100 mm × 15 mm. Chemical compositions of the as-cast 7075 alloy in wt% were Al–6.08Zn–2.5Mg–1.93Cu–0.46Fe–0.4Si.

To study the influence of solution heat treatment (SHT) on microstructures of the alloy, the as-cast alloy was solution treated at temperatures of 450 °C and 480 °C for 1, 4, 8, and 12 h and subsequently quenched in water at a temperature of 25 °C. The microstructure was characterized by using combination of an optical microscopy (OM) and a JSM-5800LV JEOL scanning electron microscopy (SEM) equipped with energy dispersive X-ray spectrometry (EDS). For optical and scanning electron examinations, specimens were ground, polished, and then etched with 0.5%HF reagent for up to 5 s before rinsing by distilled water.

To study the influence of T6 aged hardening microstructures of the alloy, the as-cast alloy was solution treated at temperatures of 450 °C for 4 h and subsequently quenched in water at temperature of 25 °C and then aged at 120 °C, 145 °C, 165 °C, and 185 °C for various time conditions.

The microstructure of T6-aged specimen was characterized by a JEM-2010 JEOL transmission electron microscopy (TEM). In order to prepare TEM specimens, a heat treated plate with the size of 15 mm × 15 mm × 50 mm was machined to a 3 mm diameter rod. This rod was then sliced into about 0.8 mm thick discs by using a low speed diamond saw. Both sides of the discs were mechanically polished to about 40–60 μm thickness with the 1200 grit SiC sand paper and 5 μm micro-polishing alumina powder. The specimen was then electropolished on a Tenupol-3 electropolisher with a solution of 20–25 vol% nitric acid and 80–75 vol% methanol at −15 °C to −20 °C and an applied current of 1.2–1.5 A.

Rockwell hardness (scale B) was primary used to evaluate the hardness of the specimens. Tensile specimens were machined into dumbbell shape with a gauge length of 25 mm and a diameter of 5 mm. Tension test was performed under a strain rate of 0.001 s^{-1}.

3. Results and discussion

3.1. Effect of solution heat treatment on microstructure and mechanical properties

As-cast microstructures of rheocast 7075 Al alloy reveals non-dendritic grain structure, as shown by SEM micrograph in Fig. 1(a). Grain boundary (GB) initially presents as a spatially continuous white contrast color, including minor amount of black line structure. The microstructure mainly consisted of matrix-α (Al) and grain boundary (GB)-eutectic phase (α-Al + η-$MgZn_2$) as discussed by Mahathaninwong et al. [20]. Predominantly, the observed phases at GBs of the as-cast Al–Zn–Mg–Cu alloy are η($MgZn_2$), T($Al_2Mg_3Zn_3$) and S(Al_2CuMg) [21–23]. The Fe-rich phases and Mg_2Si also formed in the alloy containing Si and Fe impurities [24]. The evolutions of morphology and content of GBs depended strongly on solution heat treatment temperature and time, as shown in Fig. 1(b)–(e). It evolved into isolated phases and decreased in content after SHT at either temperature of 450 °C or 480 °C. After 450 °C SHT for 1 h, the discontinuous GB phases were observed (Fig. 1(b)), while isolated GB phases were clearly observed in the specimens solution treated at 450 °C longer than 4 h (Fig. 1(c) and (d)) and at 480 °C for 1 h (Fig. 1(e)). Optical micrographs in Fig. 2 revealed isolated phases in two different color contrasts; gray and black. Most of the isolated phases at the first 4 h of 450 °C-SHT showed gray contrast with the shapes of either a skeleton or an irregular shape, as pointed out by black and white arrows in Fig. 2(a), respectively. These microstructures were similar to those presented by Doroshenko et al. [25]. Dark and light gray skeleton phases were identified as (Cu,Fe)Al_6 and Cu_2FeAl_7,

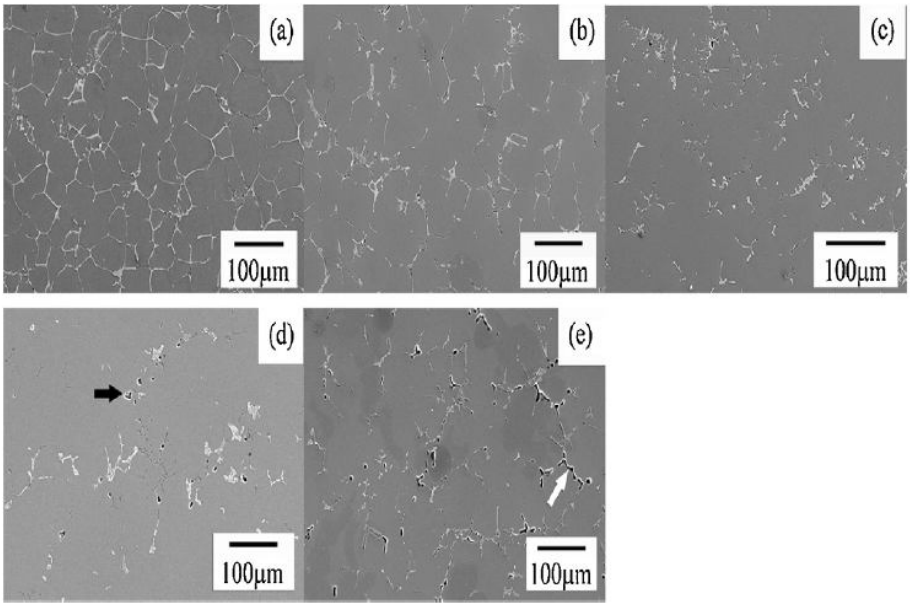

Fig. 1. SEM micrographs of GISS processing rheocast 7075 Al alloy (a) as-cast and as quenched after (b) SHT 450 °C/1 h (c) 450 °C/4 h (d) 450 °C/8 h and (e) 480 °C/1 h specimens.

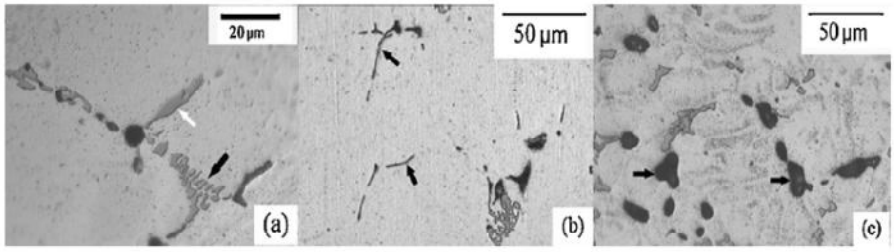

Fig. 2. Optical micrographs showing (a) skeleton and irregular shaped (b) black line shaped and (c) coarse black particles in the SHT specimen, as indicated by arrows.

respectively, while irregular-shaped particles were (Cu,Fe)Al_6. Black line phase observed in Fig. 2(b) was also identified as Mg_2Si. In addition, coarse black particles were clearly observed in the 450 °C for 8 h, and 480 °C for 1 h or prolonged holding time SHT specimens, as indicated by arrows in Figs. 1(d),(e) and 2(c). These particles were specified by Chen et al. [26], as melted constituents due to homogenization at high temperature while Curle and Govender [16] reported that it was the pores caused by incipient melting during solution treatment. However, our previous study [20] indicated these particles to be residual overheated Mg_2Si particles forming after melting of low melting point Mg(Zn,Cu,Al)$_2$ phase in multinary eutectic area.

The influence of SHT temperature and time on the microstructure of the alloy was quantitatively analyzed on the area fraction of Al–Cu–Fe phase, black line Mg_2Si phases, and coarse black particles as shown in Figs. 3–5. The area fraction results in Fig. 3 reveal that the content of Al–Cu–Fe intermetallic phases gradually decreases with increasing solution heat treatment time at both temperatures. In contrast, the amounts of Mg_2Si intermetallic phase in Fig. 4 clearly increase when SHT time was over 8 h at 450 °C while it slightly changes when SHT times were from 1 to 12 h at 480 °C. It can be noticed from Fig. 5 that coarse black particles were not found in the specimen solution treated at 450 °C for the first 4 h, however, these particles started to form for prolonging SHT times. On the other hand, coarse black particles were found to form when the specimens were solution treated only for 1 h at 480 °C. This observation suggests that SHT temperature of 480 °C is high enough to melt Mg(Zn,Cu,Al)$_2$ phase in multinary eutectic area and form coarse Mg_2Si phase afterward leaving no chance of forming black line Mg_2Si as observed in 450 °C solution treated specimens.Effects of SHT on the ultimate tensile strength (UTS) and elongation were

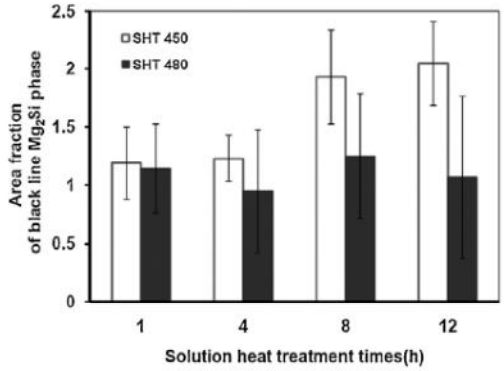

Fig. 4. Area fraction of black line Mg_2Si phase in GISS-processed rheocasting 7075 Al alloy after SHT at 450 °C and 480 °C for various time conditions.

carried out. Tensile test results of solution treated specimens are given in Fig. 6 indicating that UTS and elongation of 450 °C for 4 h specimens were higher than those of 480 °C for 1 h specimens. High density of coarse black particles was a major cause of low strength and elongation in 480 °C for 1 h. These results hence indicate that the higher SHT temperature, 480 °C, at any treated time and the lower SHT temperature, 450 °C, at prolonging SHT time, >4 h, were not proper to be performed on this alloy. Short SHT time of 1 h at 450 °C was also improper for this alloy because the eutectic phase was not completely dissolved [20]. Fig. 7 shows

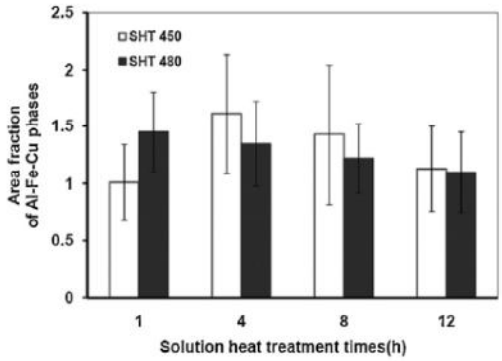

Fig. 3. Area fraction of Al–Fe–Cu phases in GISS processing rheocast 7075 Al alloy after SHT at 450 °C and 480 °C for various time durations.

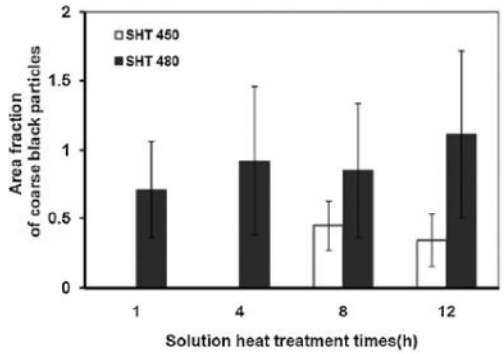

Fig. 5. Area fraction of coarse black area in GISS-processed rheocasting 7075 Al alloy after SHT at 450 °C and 480 °C for various time durations.

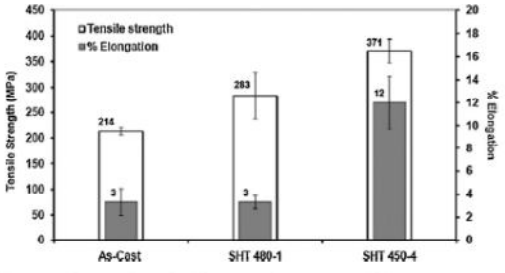

Fig. 6. Tensile strength and % elongation of GISS-processed rheocasting 7075 Al alloy before and after SHT.

the hardness values of 120 °C for 12 h artificially aged specimens under different solution treated conditions. It can be seen from this figure that the optimum SHT condition giving the highest hardness value is 450 °C for 4 h. Therefore, the present study chose to use SHT condition of 450 °C for 4 h to further investigate the aged hardening effect on the specimen.

3.2. Effect of aged hardening on microstructure and mechanical properties

Aging treatment was carried out in order to increase the strength and hardness of the alloy. During a proper solution treatment, the alloy constituents would be dissolved as much as possible without forming brittle and coarse particles. If the alloy is rapidly cooled, e.g., by quenching in water, this rich solid solution will not be stable and excess elements or compounds would precipitate out of the solution resulting in an increase in strength of the alloy. The aging temperatures used in this study were 120 °C, 145 °C, 165 °C, and 185 °C. Fig. 8 shows how the hardness of the specimens varies as a function of time at each aging temperature. The maximum hardness of the aged specimens produced by GISS technique in this work was attained by aging at 120 °C for 72 h. This result was not in agreement with some previous studies in which the peak aged conditions of 7075 Al alloy formed by squeeze casting and by extrusion were obtained by aging at 120 °C for 24 h [1] and 121 °C for 48 h [10], respectively. It is possible that our alloy contained high amount of Fe and Si leading to the formation of the Fe-rich phases and the Mg_2Si phase during casting as mentioned above. These insoluble phases resulted in low supersaturated solid solution in matrix after SHT process. Since aging response depends mainly on

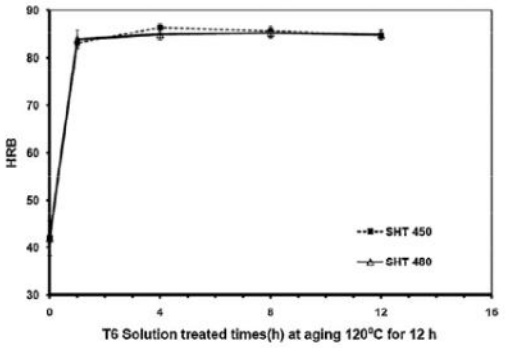

Fig. 7. Effects of solution treatment temperature and time on hardness value of the 120 °C for 12 h artificially aged specimens.

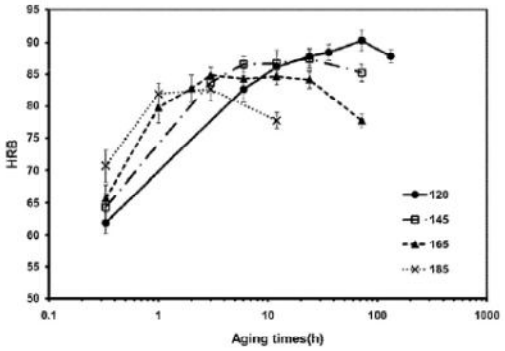

Fig. 8. Hardness vs. time for various aging temperatures.

the supersaturation degree of the matrix [39], the aging response of this alloy is then slower than that of the 7075 Al alloy containing low contents of Fe and Si. It is also noted from Fig. 8 that the outstanding peak aged conditions of the three other aging temperatures; 145 °C, 165 °C, and 185 °C, were not present. Instead, the hardness plateau was maintained and the onset hardness for artificial aging at temperatures 145 °C, 165 °C, and 185 °C were at 6, 3, and 1 h, respectively. As anticipated, the onset of hardness plateau is reached in a shorter time with increasing aging temperatures as diffusion rates are faster at higher temperatures.

The tensile strength and % elongation of the alloy aging to the peak hardness value and the onset hardness plateau values are shown in Fig. 9. The highest average tensile strength of 486 MPa with an average elongation of 2% was measured from specimens aged at temperature of 120 °C for 72 h. This was close to an average tensile strength of 484 MPa derived from specimens aged at 145 °C for 6 h. Although the strength of the alloy in this study did not meet the wrought alloy target [18], the value was close to those of the thixoformed products as reported in Refs. [2,3]. Slight increase in elongation of aged specimens compared to the as-cast specimens and trends of increase in elongation with increasing aging temperatures were observed in the 7075 Al alloy produced by rheocasting with GISS technique. The disappearance of eutectic phases and the existence of insoluble phases resulted in the improvement of average elongation in the SHT specimens to 12%. After aging, however, there was a loss in elongation of about 75% but a gain in strength of about 31% owing to precipitation hardening. Elongation is governed by defects [4] and insoluble phases [25]. High strength casting 7075 Al alloy could be produced through predeformed alloy on aging [40], while thermomechanical process was reported to increase the elongation of cast 7075 Al alloy [41]. However, a combination

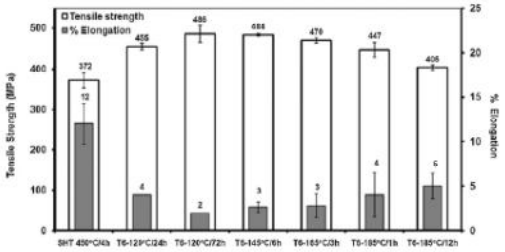

Fig. 9. Tensile strength and % elongation of GISS-processed rheocasting 7075 Al alloy after T6 aging process at various temperatures and time durations.

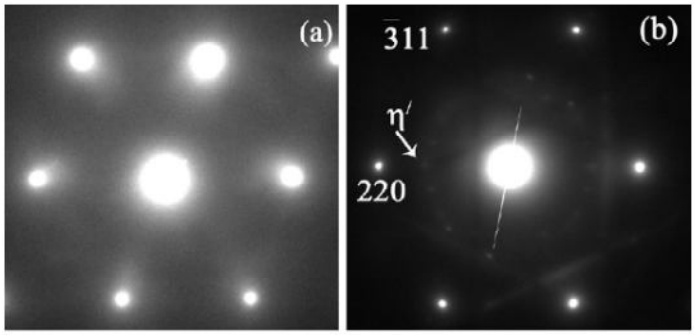

Fig. 10. Diffraction patterns (a) [1 1 0] zone axis after aging at 120 °C for 24 h and (b) [1 1 4] zone axis after aging at 120 °C for 72 h.

of precipitate hardening and strain hardening due to dislocation exerts influence on mechanical properties depending on the predeformed degree [42]. In addition, increase in strength of the alloy with no adverse effect on ductility by two-step artificial aging has been reported [27]. Strength and elongation improvements of the alloy produced by the GISS technique still need to be further investigated.

Precipitations in the aged specimens were determined using bright field (BF) imaging and selected area electron diffraction (SAED) analysis on TEM. Fig. 10(a) shows [1 1 0] zone axis of α-Al matrix in the 120 °C for 24 h aged specimen. There are no extra spots other than those from the α-Al matrix suggesting that fine precipitates in the aged specimen as shown in Fig. 15(a) were GP zone precipitates having the same crystal structure as that of the matrix [27]. This observed precipitate, GP zone, was different from the η′ phase formed in commercial 7075 Al alloy after aging under the same conditions, 120 °C for 24 h [11]. The GP zone precipitates got coarsening and transformed to η′ precipitates after increasing aging time to 72 h as observed in Fig. 15(b). This evidence was confirmed by the appearance of extra weak precipitate spots shown in [1 1 4] zone axis of the 120 °C for 72 h as shown in Fig. 11(b) which corresponded well to the diffraction pattern of precipitates reported in Du et al. [28]. Electron diffraction patterns of specimens aged at 145 °C, 165 °C, and 185 °C to the onset of hardness plateau also showed the existence of η′ phase as observed in Figs. 11(b), 12(b) and 13(a), respectively. It was indexed by diffraction spots at 2/3{2 2 0} position, while early nucleation η phase was also indexed by diffuse diffraction around 2/3{2 2 0} position at aging conditions of 145 °C, 165 °C, and 185 °C for 6, 3, and 1 h, respectively. Emani et al. [10] suggested that diffraction contrast would increase as the precipitates became coarsened and completely transformed to the transition phases. Clear precipitate spots with no diffusion shown in Fig. 14(b) indicated that η phase dominantly formed after aging at 185 °C for 12 h corresponding to larger size precipitates as illustrated in Fig. 15(f). In the analysis of the diffraction pattern in [1 1 2] zone axis using schematic diffraction pattern of Refs. [29,30] η′ phase was also found to transform to η phase after aging at 145 °C for 6 h, which were indexed by weak diffuse spots at 2/3{2 2 0} and 2/3{3 1 1} positions, as shown in Fig. 11(a). After aging at 165 °C for 3 h, precipitate spots, identified to be dominantly η′, clearly appeared at 1/3{4 2 2} position as shown in the electron diffraction pattern of [1 1 1] zone axis in Fig. 12(a). In addition, weak η phase spots were also observed near 2/3{2 2 0} position, identical to that reported in Refs. [31–33]. However, extremely weak diffuse spots at 1/3{4 4 2} position and low intensity around 2/3{2 2 0} position in diffraction pattern [1 1 1] zone axis in Fig. 13(a) implied that η phase had just started to form in the specimen after aging at 185 °C for 1 h. Additionally, η phase spots also appeared on electron diffraction pattern in [0 0 1] zone axis, as shown in Fig. 13(b). This is in accordance with the schematic diffraction patterns of Refs. [34,35]. Li et al. [40] reported that GP zone and η′ phase are formed predominantly in the microstructure of the 7075 al alloy at peak aged conditions after a T6 temper coupled with prestretching. In contrast, the present results indicate that fine dispersion of η′ phase is mainly responsible for the peak hardness in the alloy, which is in good agreement with the report by Park and Ardell [43]. Moreover, η′ phase also predominated and η phase started early to form in the microstructure of the alloy after artificial aging at the three aging temperatures of 145 °C, 165 °C, and 185 °C for onset hardness plateau times.

Fig. 15 shows the difference in precipitate size and number density of specimens aged at various conditions. High density of very

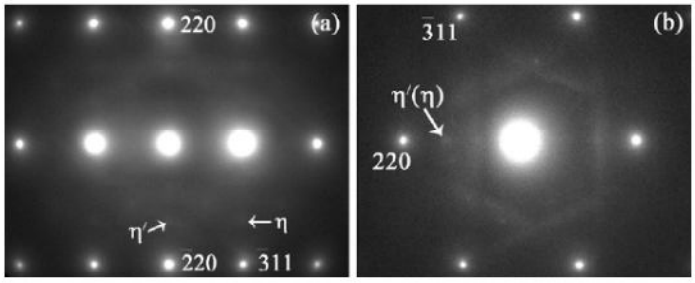

Fig. 11. Diffraction patterns after aging at 145 °C for 6 h (a) [1 1 2] zone axis and (b) [1 1 4] zone axis.

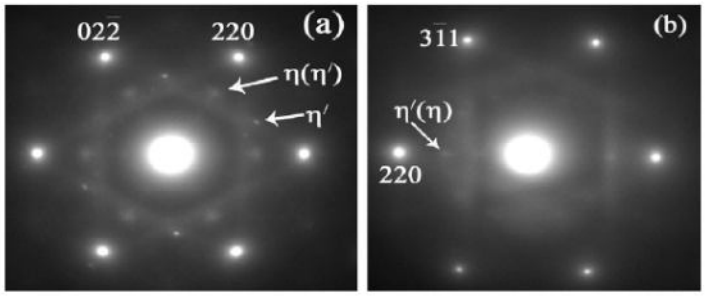

Fig. 12. Diffraction patterns after aging at 165 °C for 3 h (a) [1 1 1] zone axis and (b) [1 1 4] zone axis.

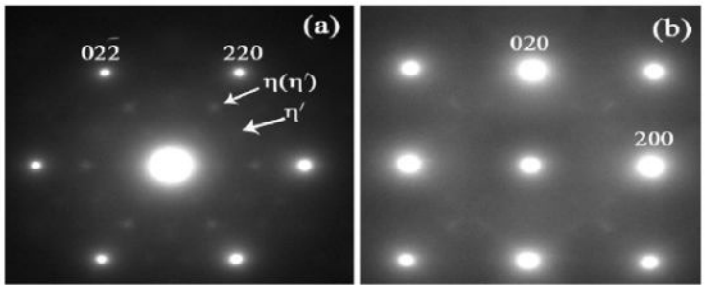

Fig. 13. Diffraction patterns after aging at 185 °C for 1 h (a) [1 1 1] zone axis and (b) [0 0 1] zone axis.

fine GP zone was observed in the specimen aged at an underaged condition of 120 °C for 24 h as shown in Fig. 15(a). With increasing aging time to 72 h or at optimum aging condition, the growth of those fine precipitates can be clearly seen (Fig. 15(b)). The same trend was observed when comparing specimens aged at 185 °C for 1 h to that aged at 185 °C for 12 h, an overaged condition, as illustrated in Fig. 15(e) and (f), respectively. Fig. 15(c)–(e) illustrates precipitate morphology in the specimens aged to the onset of hardness plateau at 145 °C, 165 °C, and 185 °C, respectively. From these figures, precipitates seemed to get bigger in size but lower in density at higher aging temperature. Higher magnification of TEM images in Fig. 16 clearly reveals precipitates in the specimens with aging temperatures of 120 °C, 145 °C, 165 °C, and 185 °C for 72, 6, 3, and 1 h, respectively. Despite high magnification, it is quite difficult to quantitatively measure the accurate precipitate size and number density from the 120 °C for 72 h aged specimen. Therefore, the average precipitate size and the precipitate density were only semi-quantitatively measured from the other three aging conditions and the results were presented in Fig. 17. By qualitative comparison from Fig. 16, the average precipitate size and the number density of precipitates in 120 °C for 72 h aged specimen appeared to be smaller and higher than those in other three specimens. Fine precipitates in the three different aged specimens appeared in shape to be both spherical and plate-like. Diameter of precipitates was approximated from the average measurements on the long and short axes of the precipitates [36]. From Fig. 17(a), fine precipitates of a 145 °C for 3 h aged specimen were in the size range of 2–7 nm in diameter, an average diameter (D_p) of 4.09 nm and volume fraction (V_p) of 1.59%. For a 165 °C-3 h and a 185 °C-1 h aged specimens, precipitates size increased to be in the range of

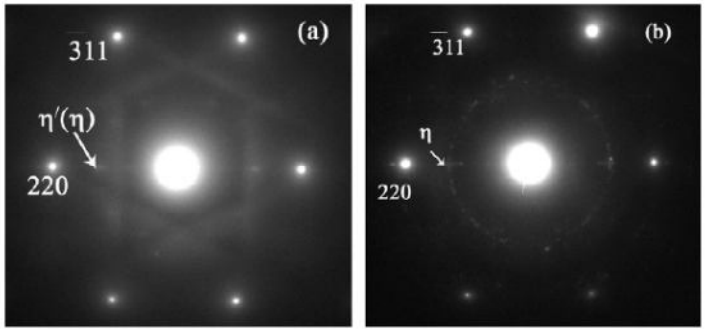

Fig. 14. Diffraction patterns of [1 1 4] zone axis in specimens aged at (a) 185 °C for 1 h and (b) 185 °C for 12 h.

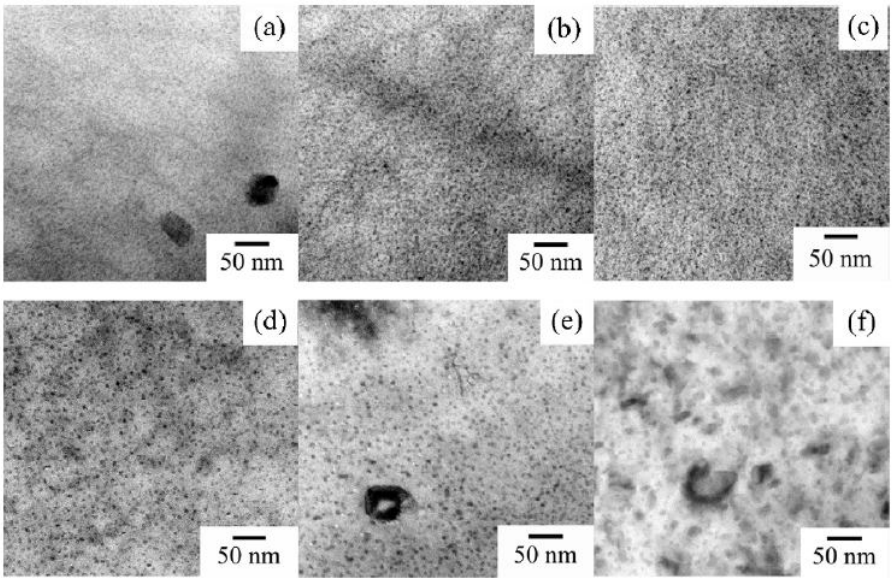

Fig. 15. TEM bright field imaging in [0 1 1] zone axis of specimen aged at (a) 120 °C for 24 h; and in [1 1 4] zone axis of specimens aged at (b) 120 °C for 72 h (c) 145 °C for 6 h (d) 165 °C for 3 h (e) 185 °C for 1 h and (f) 185 °C for 12 h.

3–8 nm and 3–10 nm in diameter with an average size of 5.37 nm and 6.71 nm, respectively. On the other hand, volume fraction in both aging conditions decreased to 1.39% and 1.14%, respectively. Therefore, it can be concluded that by aging specimen at a higher temperature to the optimum condition, η' phase nucleated under the influence of a smaller driving force than at a lower temperature. Thus, precipitate dispersion would be coarser and the volume fraction would be reduced, causing the hardness and the tensile

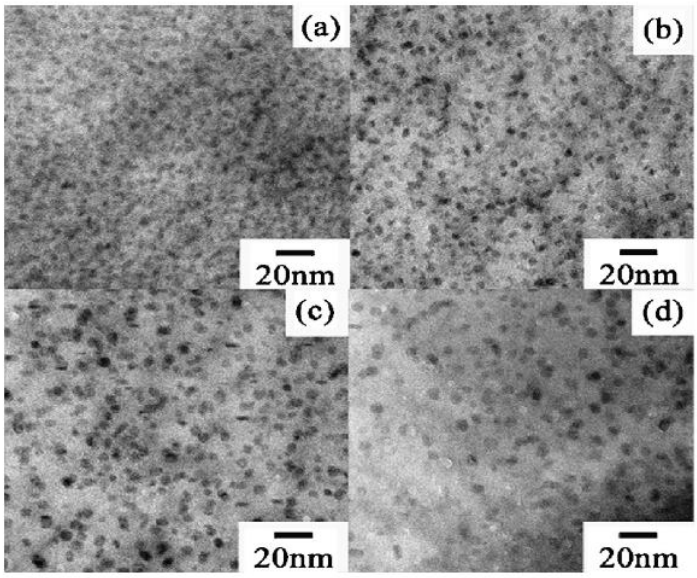

Fig. 16. TEM bright field imaging at higher magnification taken in [1 1 4] zone axis showing relative precipitate size and number density in four different aged conditions at (a) 120 °C for 72 h (b) 145 °C for 6 h (c) 165 °C for 3 h and (d) 185 °C for 1 h.

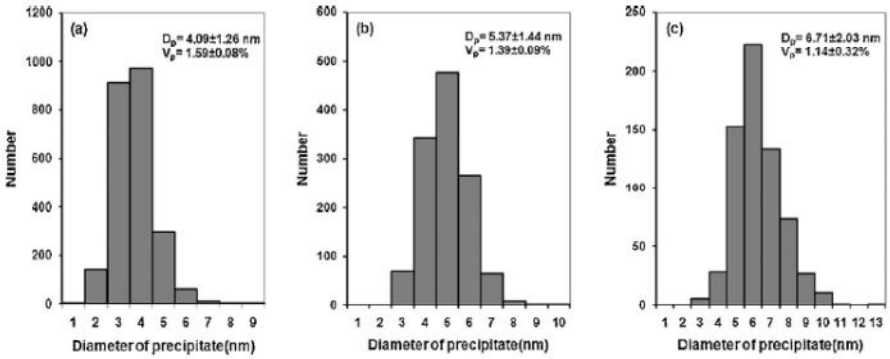

Fig. 17. Average precipitate size distributions of aged specimen at (a) 145 °C for 6 h (b) 165 °C for 3 h and (c) 185 °C for 1 h.

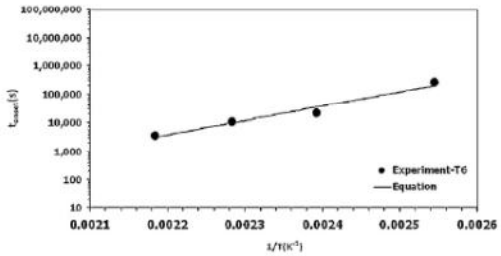

Fig. 18. Arrhenius-type plot between aging temperature and onset of hardness plateau time of the alloy.

strength to decrease. The precipitate size distribution in this study was consistent with a prior study by Park and Ardell [43] that the diameter of η' phase was in the range of 3–10 nm.

Apparent activation energy for precipitate hardening process of the alloy can be determined following the notation in Ref. [37]. Artificial aging times (in s) at the onset of hardness plateau as a function of artificial aging temperatures (in K) were plotted following an Arrhenius-type response in the equation $t_{T6} = C\exp(Q/RT)$ with C the pre-exponential factor, Q the apparent activation energy in J/mol and R the universal gas constant = 8.314 J/mol K, as shown in Fig. 18. The Arrhenius-type response for the obtained 7075 Al alloy produced by GISS technique is given in Eq. (1)

$$t_{T6} = 4 \times 10^{-8} \exp\left(\frac{95,827}{RT}\right) \quad (1)$$

The apparent activation energy for precipitate process in the alloy was calculated to be 95,827 J/mol. It had been reported by Garcia-Cordovilla and Louis [38] that the apparent activation energies of η' precipitation and η' dissolution in 7075-T6 alloy were 69,200 J/mol and 97,400 J/mol, respectively. It is noted that the activation energy determined from our study is close to the value of the η' dissolution activation energy, indicating that at the onset of hardness plateau the η' phase started to coarsen and transform to η phase. By using Eq. (1), one could predict the time to reach maximum hardness (t_{T6}) of the 7075 Al alloy in this study.

4. Conclusions

It can be concluded from this study that high solution treatment temperature of 480 °C and prolonged solution heat treatment time at 450 °C resulted in incipient melting which led to the formation of deteriorated overheated Mg_2Si particles. The optimum solution treatment condition, in which the eutectic phase almost completely dissolved and no overheated Mg_2Si particles were formed, was at 450 °C for 4 h. By using this SHT condition and by aging the specimen to complete T6 heat treatment, the highest average hardness and the highest average UTS of about 90 HRB and 486 MPa were obtained from the specimen artificially aged at 120 °C for 72 h. At higher aging temperatures, 145 °C, 165 °C, and 185 °C, the peak hardness values decreased while the precipitate size increased with increasing aging temperature as the number density of fine precipitates decreased owing to the lower driving force for nucleation at higher aging temperature. However, the time to achieve the optimum hardness was shorter due to higher diffusion rate at higher aging temperature. The η' phase was mainly responsible for strengthening at all aging temperatures, while the η phase started to form at 145 °C, 165 °C, and 185 °C for the onset of hardness plateau times. The activation energy for forming the precipitates of the alloy at the onset of peak-aged time derived from this research was 95,827 J/mol.

Acknowledgments

The authors would like to thank thePrince of Songkla University for the 50% Ph.D. scholarship financial support, as well as supports from the Higher Education Research Promotion and National Research University Project of Thailand, Office of the Higher Education Commission (Grant No. ENG540551c), the Thailand Research Fund through the Royal Golden Jubilee Ph.D. Program (Grant No. PHD/0031/2552), and the Office of National Research Council of Thailand through the Development of High-Quality and Low-Cost Below Knee Prosthesis Project. In addition, we would like to thank the PSU Department of Mining and Materials Engineering and the Department of Industrial Engineering for laboratory facilities.

References

[1] S.W. Kim, D.Y. Kim, W.G. Kim, K.D. Woo, Mater. Sci. Eng. A 304–306 (2001) 721–726.
[2] J. Dong, J.Z. Cui, Q.C. Le, G.M. Lu, Mater. Sci. Eng. A 345 (2003) 234–242.
[3] D. Liu, H.V. Atkinson, P. Kapranos, W. Jirattiticharoean, H. Jones, Mater. Sci. Eng. A 361 (2003) 213–224.
[4] S. Chayong1, H.V. Atkinson, P. Kapranos, Mater. Sci. Eng. A 390 (2005) 3–12.
[5] R. Clark Jr., B. Coughran, I. Traina, A. Hernandez, T. Scheck, C. Etuk, J. Peters, E.W. Lee, J. Ogren, O.S. Es-Said, Eng. Fail. Anal. 12 (2005) 520–526.
[6] O.S. Es-Said, T.M. Ruperto, S.L. Vasquez, A.Y. Yue, D.J. Manriquez, J.C. Quilla, S.H. Harris, S. Hannan, J. Foyos, E.W. Lee, B. Pregger, N. Abourialy, J. Ogren, J. Mater. Eng. Perform. 16 (2007) 242–247.
[7] S.K. Kim, Y.Y. Yoon, H.H. Jo, J. Mater. Process. Technol. 187–188 (2007) 354–357.
[8] H.S. Turkmen, R.E. Loge, P.R. Dawson, M.P. Miller, Int. J. Fatigue 25 (2003) 267–281.

[9] J. Jabra, M. Romios, J. Lai, E. Lee, M. Setiawan, E.W. Lee, J. Witters, N. Abourialy, J.R. Ogren, R. Clark, T. Oppenheim, W.E. Frazier, O.S. Es-Said, J. Mater. Eng. Perform. 15 (2006) 601–607.
[10] S.V. Emani, J. Benedyk, P. Nash, D. Chen, J. Mater. Sci. 44 (2009) 6384–6391.
[11] J.F. Li, Z.W. Peng, C.X. Li, Z.Q. Jia, W.J. Chen, Z.Q. Zheng, Trans. Nonferrous Met. Soc. China 18 (2008) 755–762.
[12] J. Wannasin, S. Janudom, T. Rattanochaikul, R. Canyook, R. Burapa, T. Chucheep, S. Thanabumrungkul, Trans. Nonferrous Met. Soc. China 20 (2010) s1010–s1015.
[13] S. Thanabumrungkul, S. Janudom, R. Burapa, P. Dulyapraphant, J. Wannasin, Trans. Nonferrous Met. Soc. China 20 (2010) s1016–s1021.
[14] D.B. Spencer, R. Mehrabian, M.C. Flemings, Metall. Trans. 3 (1972) 1925–1932.
[15] H.V. Atkinson, Prog. Mater. Sci. 50 (2005) 341–412.
[16] U.A. Curle, G. Govender, Trans. Nonferrous Met. Soc. China 20 (2010) s832–s836.
[17] M. Song, K. Chen, J. Mater. Sci. 43 (2008) 5265–5273.
[18] ASM Metals Handbook: Heat Treating, vol. 4, ASM International, USA, 1991.
[19] A.K. Mukhopadhyay, Trans. Indian Inst. Met. 62 (2009) 113–122.
[20] N. Mahathaninwong, S. Wisutmethangoon, T. Plookphol, J. Wannasin, Adv. Mater. Res. 339 (2011) 371–374.
[21] X. Fan, D. Jiang, Q. Meng, L. Zhong, Mater. Lett. 60 (2006) 1475–1479.
[22] X.M. Li, M.J. Starink, Mater. Sci. Technol. 17 (2001) 1324–1328.
[23] Y.L. Deng, L. Wan, L.H. Wu, Y.Y. Zhang, X.M. Zhang, J. Mater. Sci. (August 2010).
[24] Z.H. Li, B.Q. Xiong, Y.A. Zhang, B.H. Zhu, F. Wang, H.W. Liu, Trans. Nonferrous Met. Soc. China 18 (2008) 40–45.
[25] N.M. Doroshenko, B.V. Ovsyannikov, V.M. Zamyatin, V.I. Popov, Met. Sci. Heat Treat. 47 (1–2) (2005) 30–35.
[26] K. Chen, H. Liu, Z. Zhang, S. Li, R.I. Todd, J. Mater. Process. Technol. 142 (2003) 190–196.
[27] A.K. Mukhopadhyay, Metall. Mater. Trans. 28 (1997) 2429–2433.
[28] Z.W. Du, Z.M. Sun, B.L. Shao, T.T. Zhou, C.Q. Chen, Mater. Charact. 56 (2006) 121–128.
[29] F. Vianaa, A.M.P. Pintob, H.M.C. Santosa, A.B. Lopes, J. Mater. Process. Technol. 92–93 (1999) 54–59.
[30] X.Z. Li, V. Hansen, J. Gjønnes, L.R. Wallenberg, Acta Mater. 47 (9) (1999) 2651–2659.
[31] Z. Li, B. Xiong, Y. Zhang, B. Zhu, F. Wang, H. Liu, Mater. Charact. 59 (2008) 278–282.
[32] X.J. Jiang, B. Noble, B. Holme, G. Waterloo, J. Tafto, Metall. Mater. Trans. A 31 (2000) 339–348.
[33] G. Sha, A. Cerezo, Acta Mater. 52 (2004) 4503–4516.
[34] T. Engdahl, V. Hansen, P.J. Warren, K. Stiller, Mater. Sci. Eng. A 327 (2002) 59–64.
[35] K. Stiller, P.J. Warren, V. Hansen, J. Angenete, J. Gjønnes, Mater. Sci. Eng. A 270 (1999) 55–63.
[36] M. Dumont, W. Lefebvre, B. Doisneau-Cottignies, A. Deschamps, Acta Mater. 53 (2005) 2881–2892.
[37] H. Möller, G. Govender, W.E. Stumpf, Open Mater. Sci. J. 2 (2008) 6–10.
[38] C. Garcia-Cordovilla, E. Louis, Metall. Trans. 21 (1990) 2277–2280.
[39] W. Tao, Y. Zhi-min, S. Kai, L. Jie, H. Ji-wu, Trans. Nonferrous Met. Soc. China 17 (2007) 548–552.
[40] Z. Li, B. Xiong, Y. Zhang, B. Zhu, F. Wang, H. Liu, J. Univ. Sci. Technol. Beijing 14 (2007) 246–250.
[41] Z.M. Barad, M. Sayed, J. Mater. Proc. Technol. 62 (1996) 76–80.
[42] A. Deschamps, F. Livet, Y. Breachet, Acta Mater. 47 (1999) 281–292.
[43] J.K. Park, A.J. Ardell, Metall. Trans. 14 (1983) 1957–1965.

APPENDIX D

Materials Science and Engineering A 532 (2012) 610–615

Contents lists available at SciVerse ScienceDirect

Materials Science and Engineering A

journal homepage: www.elsevier.com/locate/msea

Precipitation hardening of A356 Al alloy produced by gas induced semi-solid process

S. Wisutmethangoon[a,*], S. Thongjan[b], N. Mahathaninwong[b], T. Plookphol[b], J. Wannasin[b]

[a] Department of Mechanical Engineering, Faculty of Engineering, Prince of Songkla University, Hat Yai, Songkhla 90112, Thailand
[b] Department of Mining and Materials Engineering, Faculty of Engineering, Prince of Songkla University, Hat Yai, Songkhla 90112, Thailand

ARTICLE INFO

Article history:
Received 29 October 2011
Received in revised form 4 November 2011
Accepted 5 November 2011
Available online 17 November 2011

Keywords:
A356 Al alloy
Gas induced semi-solid
Aged hardening
Transmission electron microscopy

ABSTRACT

Aged hardening of semisolid cast A356 Al alloy produced by gas induced semi-solid (GISS) process was studied. It was found that maximum hardness and tensile strength could be achieved from specimens aged at 165 °C for 18 h of which the average maximum hardness, the average ultimate tensile strength and the average percent elongation were 96.4 HRE, 312 MPa and 7.6%, respectively. The higher aging temperature of 195 °C for 3 h led to a slightly lower average tensile strength of 305 MPa together with a higher average elongation of 9.8%. The strain hardening exponent of specimens aged at both sets of conditions was lower than that of the as-cast specimen as well as the as-cast specimen aged at 225 °C for 15 min. The mechanical properties of the alloys in this study were comparable to those of typical thixo-formed products. β″ phase was mainly responsible to the strengthening of the peak aged alloy. Elongated precipitates were formed in the specimen after prolonged aging at 195 °C for 16 h. The activation energy for the precipitation hardening process of the alloy derived in this research was 128,717 J/mol.

1. Introduction

Light weight casting aluminium alloy has been extensively adopted for a variety of usage as automotive components in view of the need to lower the weight of vehicles. Nevertheless, preserving performance of the alloy and cost investment still have been the objectives for the industries. It was pointed out by Thanaburungkul et al. [1] that conventional A356 Al cast products normally contain more porosities than semisolid A356 Al products. The presence of porosities was believed to be harmful to ductility of A356.2 Al alloy [2] and also to the tensile strength of A356 Al alloy according to Lee [3]. Therefore, semisolid casting is a promising process for providing higher quality aluminium alloy castings [4]. An alternative rheocasting process has been steadily of interest because of low material cost and single step forming process. The study of slurry semisolid alloy was published as early as 1972 [5]. Various techniques were later proposed such as cooling slope [6], and electromagnetic stirrer [7].

A novel approach, gas induced semi-solid (GISS) technique, has been proposed by the Innovative Metal Technology (IMT) team at the Prince of Songkla University. This technique involves the flow of very fine inert gas bubbles out of porous graphite to the liquid aluminium. It has since been proven a simple, economical and efficient process. Additionally, this technique has succeeded to produce globular structure in A356 alloy [8].

Though selections of the right alloy and suitable casting process are important, proper tempering condition for the alloy is also crucial in achieving the required properties. Responses to heat treatment of A356 Al alloy and other Al alloys had been reported in many earlier studies [9,10].

The aim of this work is to investigate the effect of artificial aging temperature and time on the mechanical properties and microstructure of the rheocast A356 Al alloy produced by the GISS process. This study focuses on the determination of the optimum aging condition of the alloy.

2. Experimental method

The material used in this study was semisolid A356 Al alloy produced by the GISS process. Schematic of the GISS process is shown in Fig. 1.

In this process, the alloy ingots were melted in a graphite crucible using an electric resistance furnace. The melt was fluxed at 700 °C before casting. About 500 g of the molten alloy was taken out from the furnace using a ladle cup. A graphite diffuser was immersed in the liquid alloy at the rheocasting temperature of 620 °C for 20 s to produce a semi-solid slurry. The slurry was then poured into a die cavity, which was preheated to 280–300 °C. A squeeze cast was subsequently applied at a pressure of approximately 20 MPa. The as-cast circular plate shape had a dimension of

* Corresponding author. Tel.: +66 81 6781243; fax: +66 87 4287195.
E-mail address: sirikul@me.psu.ac.th (S. Wisutmethangoon).

0921-5093/$ – see front matter © 2011 Elsevier B.V. All rights reserved.
doi:10.1016/j.msea.2011.11.026

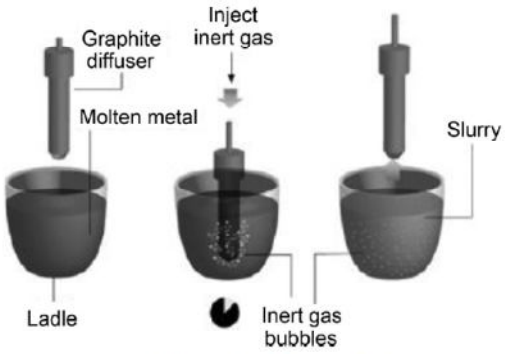

Fig. 1. Schematic of the GISS process [11].

200 mm in diameter and 15 mm in thickness. The chemical composition of the as-cast A356 Al alloy is shown in Table 1.

T6 heat treatment process was used in this study at the solution treated temperature of 540 °C for 4 h. After quenching in room temperature water, the as-quenched specimens were aged at 165 °C, 195 °C and 225 °C under varying time durations. The microstructure of the as-cast and the solution heat treated specimens were examined using optical microscopy. Hardness was measured using Rockwell hardness (scale E) test from three specimens under each aging condition and from 10 different points on each specimen. Tensile specimens were machined into a dumbbell shape with a gauge length of 30 mm and a diameter of 6 mm. Tension test was performed under a strain rate of 0.001 s^{-1}.

The aged specimen with a dimension of 15 mm × 15 mm × 50 mm was machined into a rod with a diameter of 3 mm for the TEM specimens. This rod was sliced into many disk-shaped specimens by using the Brillant 220 cutting machine. The disk-shaped specimen was polished down to a thickness of 40–80 μm thin foil using 1200 grit SiC sand paper and 5 μm micro-polishing alumina powder. TEM thin foils were then prepared by twin-jet electro polishing in a mixture of 20 vol.% nitric acid and 80 vol.% methanol at a cooling temperature range of −15 °C to −30 °C employing liquid nitrogen, an applied current of 150–250 mA, a flow rate of 4.4–5.5 and a sensitivity of 3–5. The electro-polishing parameters were varied depending on the heat treatment condition and the thickness of each thin foil. The thin foils were examined on a JEOL JEM-2010 transmission electron microscope, operating at 200 kV.

3. Results and discussions

3.1. As-cast and solution heat treated specimens

The non-dendritic microstructure of the as-cast A356 0Al alloy was obtained from the GISS process under 10% solid fraction in melt coupled with low pressure squeeze cast. Canyook et al. [12] believed that dendritic α-Al phase was fragmented through the GISS process by a remelting mechanism leading to form the rheocast structure. The microstructure of the as-cast alloy mainly consists of primary α-Al phase (white contrast) surrounded by lamella eutectic phase of acicular-like Si particles (grey phase) and α-Al phase (white phase), as clearly revealed in Fig. 2(b). After solution heat treatment at 540 °C for 4 h, the acicular-like silicon particles exhibit disintegration and roundness, as depicted in Fig. 2(c) and (d). It was believed that the morphology of silicon particles has an influence on the fracture elongation of the alloy [13]. In another view, the properties of A356 Al alloy were controlled by either the Si morphology or the alloying elements, or a combination of both factors depending on the heat treatment conditions [14].

3.2. Aged hardening specimens

The variations of hardness when exposed to different aging temperatures at different aging durations are shown in Fig. 3. The figure shows that the hardness of each specimen increases with increasing aging time until a peak hardness is obtained. Then the hardness tends to decrease upon further aging time. This result could be explained by precipitation hardening process of the aged specimen which depends greatly on the aging time and aging temperature. A peak hardness value of 96.4 HRE was obtained from the specimen aged at the temperature of 165 °C for 18 h. This is in agreement with the peak hardness time of SSM-High-Pressure Die Casting (HPDC) A356 Al alloy [15]. In their study, the peak hardness of about 97 HRE was obtained after T6 aging at 160 °C for 24 h (Fig. 3) shows that peak hardness of 94.5 and 94.1 HRE was obtained from the specimen aged at higher temperature of 195 °C and 225 °C, respectively. This value was slightly lower than that of the specimen aged at 165 °C as mentioned before. The lower in the hardness at higher aging temperature was the result of the absence of GP zone formation in the early stage of aging leading to a lower precipitate density at the peak condition, and hence the lower hardness and lower strength of the alloy. However, the required aging time to the peak condition was shorter at higher aging temperatures; 3 h and 15 min for 195 °C and 225 °C, respectively. It can be explained that the shorter aging time at higher aging temperature was due to a higher diffusion rate for precipitate formation at higher temperature.

The average yield strength, tensile strength, and percent elongation of the alloy after aging to the peak hardness at different aging temperatures of 165 °C, 195 °C, and 225 °C are tabulated in Table 2. The highest average ultimate tensile strength (312 MPa) and yield strength (277 MPa) with an average elongation of 7.6% were obtained from the specimens aged at the optimum condition of 165 °C–18 h. It can be noticed from Table 2 that the specimen aged at the condition of 195 °C–3 h had a slightly lower average tensile strength and yield strength of 305 MPa and 272 MPa, respectively. These strength values were lower than those of the optimum aged (165 °C–18 h) specimen, however, its elongation increased to 9.8%. With further increasing aging temperature to 225 °C at aging time of 15 min, the elongation of this aged specimen increased further to 14.9% at the expense of tensile strength and yield strength down to the values of 226 MPa and 125 MPa, respectively. For comparison, the typical tensile properties of A356 alloy in selected literatures are also listed alongside in Table 2 [13,16,17]. Although the average tensile strength and the yield strength of the as-cast GISS-processed alloy were lower than those of the as-thixoformed products [16]. these strength values of the GISS-processed specimen were improved and were apparently higher than those of the thixoformed products [16] after passing T6 heat treatment. The strength of the T6-thixoformed products as reported in Ref. [13]

Table 1
Chemical composition of the as-cast A356 Al alloy.

Elements	Si	Mg	Fe	Cu	Mn	Zn	Ti	Al
Composition (wt%)	7.00	0.35	0.2	0.2	0.1	0.1	0.23	Bal.

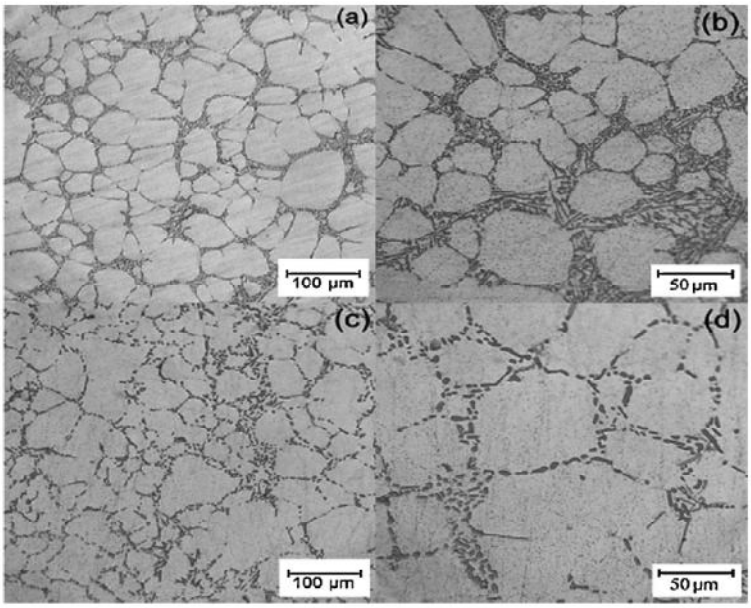

Fig. 2. Optical micrographs showing the microstructure of (a) and (b) as-cast specimen and (c) and (d) solution heat-treated specimen.

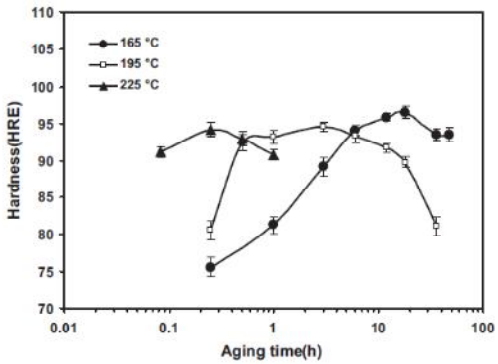

Fig. 3. Hardness vs. aging time at three different aging temperatures, 165, 195 and 225 °C.

was comparable to that of the T6-GISS-processed specimens. However, the elongation of the alloy in this study was still lower than that of the other products. It should be noted that the T6 heat treatment condition used in Refs. [13,16,17] was somewhat different from that employed in the present study. For the simplified age-hardening model as referred to by Rometsch and Schaffer [18], the overall yield strength of the A356 alloys was reported to be the sum of the intrinsic strength from pure aluminium and eutectic Si particles, and the large contribution strength from Mg–Si precipitate formed during aging; while the strength of the as-cast alloy was mainly contributed from pure aluminium and eutectic Si particles only. In this experiment, an appropriate aging time of 18 h at 165 °C could be used to increase the yield strength of the specimen to be approximately quadruple of that of the as-cast specimen. Therefore, precipitation strengthening of the alloy in this study has more pronounced effect than that of the products referred in Ref. [16].

It is well accepted that precipitates are mainly responsible for strengthening of the alloys after artificial aging. Precipitates in the aged specimens were visualized using bright field (BF) TEM imaging and selected area electron diffraction (SAED) patterns along the [0 0 1] and [1 1 0] directions of the matrix. In the as-quenched specimen, no precipitate can be observed in the microstructure of the alloy, as evidenced in Fig. 4a. High number density of edge-on

Table 2
Tensile properties of the as-cast and the aged A356 Al alloy produced by GISS process in comparison to other forming processes.

Material conditions	YS (MPa)	UTS (MPa)	Elongation (%)	Ref.
As-cast GISS process	77	172	6.6	
GISS-T6 aging (165 °C–18 h)	277	312	7.6	
GISS-T6 aging (195 °C–3 h)	272	305	9.8	
GISS-T6 aging (225 °C–15 min)	125	226	14.9	
Cast-T6 aging (182 °C–8 h)	200	298	12	[17]
As-thixoformed	104	241	12	[16]
Thixoformed-T6 aging (160 °C–24 h)	150	264	16	[16]
Thixoformed-T6 aging (160 °C–4 h)	229	317	16.7	[13]

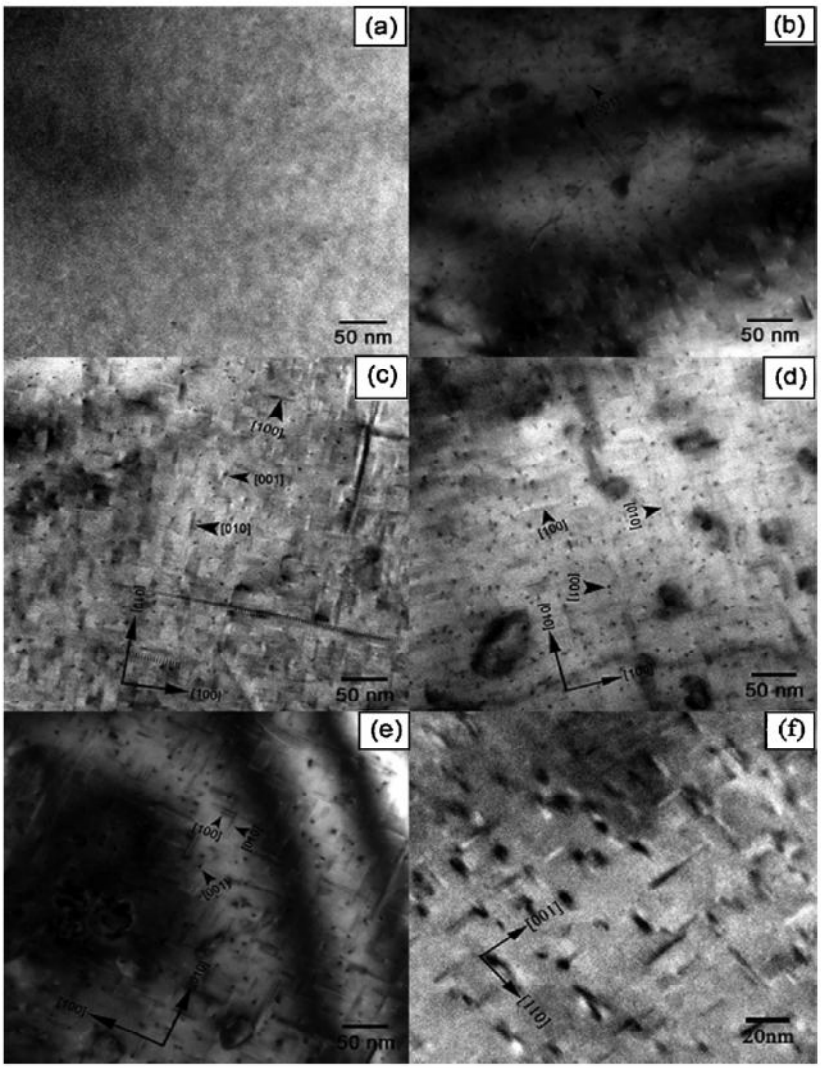

Fig. 4. TEM bright field micrographs of specimen aged at (a) as-quenched (unaged), (b) 165 °C–12 h, (c) 165 °C–18 h, (d) 195 °C–3 h, (e) 195 °C–16 h and (f) 225 °C–15 min {(a)–(e) [1 0 0] zone axis and (f) [1 1 0] zone axis}.

precipitates appeared after aging at 165 °C for 12 h, while side-on needle precipitates were not clearly noticeable, as shown in Fig. 4b. It is possible that the precipitate size was too small to be observed from its strain field contrast. Furthermore, these very fine precipitates at the underaging condition were mostly GP zones which would form coherent interface with the matrix and hence contribute to low misfit strain. The images in Fig. 4(c) and (d) reveal both edge-on and side-on precipitates lying in the Al matrix along three variants of $\langle 0\,0\,1\rangle_{Al}$ as pointed out with black arrowheads. The microstructure is quite similar to that reported in Al–Mg–Si alloy with excess Si [19]. The side-on needle-shape precipitates can be seen in the microstructure of the peak aged specimen at 165 °C for 18 h, as illustrated in Fig. 4(c). These are likely to be the β″ phase, as reported by Chomseang et al. [20]. The needles were typically about 10–20 nm in length, which is in agreement with 10–15 nm precipitate length of β″ phase in peak aged 6061 Al alloy at 175 °C for 4 h [21]. Precipitates with the length of 10 nm in semisolid cast A356 Al alloy aged at 160 °C for 18 h was reported by Chomseang et al. [20]. The needle-shape precipitates with a length of 10–20 nm also appeared in the microstructure of the GISS-processed alloy after aging at the higher temperature of 195 °C for shorter aging time of 3 h as depicted in Fig. 4(d). However, the precipitate density in this

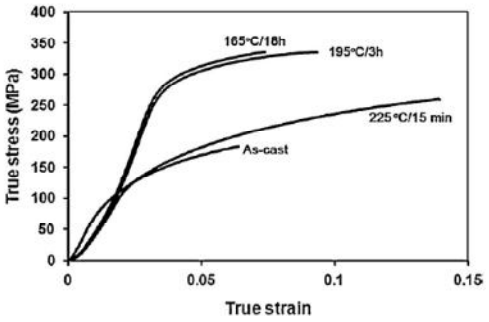

Fig. 5. True stress vs. true strain curve of the GISS-processed A356 Al alloy for the as-cast condition, and the three peak hardness time conditions at different aging temperatures.

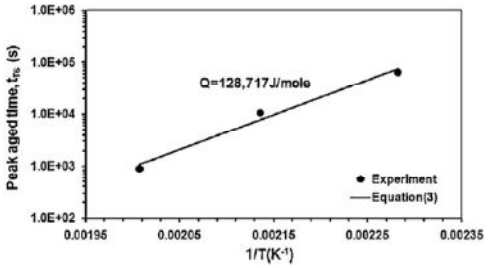

Fig. 6. Arrhenius-type plot between the peak hardness time (t_{T6}) and the aging temperature (T) of A356 Al alloy produced by GISS process.

specimen was qualitatively lower than that of the specimen aged at optimum condition of 165 °C for 18 h. This resulted in the slightly lower average hardness and lower tensile strength. Specimens with longer aging time of 16 h at 195 °C and higher aging temperature of 225 °C for 15 min showed longer and coarser needle precipitates, which were clearly delineated by strain-field contrast as illustrated in Fig. 4(e) and (f), respectively. It is found from Fig. 4(e) that needle-shape precipitates elongated to about 30–50 nm in length after prolonging the aging time to 16 h at 195 °C. Fig. 4(f) shows a BF image of the specimen aged at 225 °C for 15 min observed along the [1 1 0] direction of the matrix. Only needle-shape precipitates and their cross-sections were observed as referred to by Matsuda et al. [22]. The length of precipitates at this aging condition was not different from that observed in the 165 °C–18 h and 195 °C–3 h aged specimens, instead, they became thicker.

From Table 2, it could be derived that dislocations in the matrix of the as-cast specimen started to take effect when the applied stress reached a yield stress of 77 MPa. This applied stress increased to 125 MPa, 272 MPa and 277 MPa after aging the specimens at 225 °C–15 min, 195 °C–3 h, and 165 °C–18 h, respectively. After yielding, plastic deformation could be described by the strain hardening exponent. Fig. 5 shows typical true stress–true strain curve obtained at a strain rate of 0.001 s^{-1}. It is not surprising to see that the work hardening behavior of the as-cast specimen was very different from the T6-aging specimens. Eq. (1) was used to approximately describe the flow curve in the uniform deformation stage after yielding up to the point corresponding to the UTS, where σ is the true stress, ε is the true strain, K is the strength coefficient and n is the strain hardening exponent [23]:

$$\sigma = K\varepsilon^n \tag{1}$$

The strain hardening exponent (n value) of the specimen at different aging conditions was calculated. Based in Eq. (1) the evaluated strain hardening exponent for the as-cast and the T6 specimens aged at 165 °C–18 h, 195 °C–3 h, and 225 °C–15 min was 0.331 ± 0.035, 0.156 ± 0.048, 0.106 ± 0.050 and 0.300 ± 0.053, respectively.

Zhen and Kang [24] pointed out that lower n value at the peak aged condition of Al–Mg–Si alloy with low Si content was caused by easy gliding of dislocations through the fine coherent β″ particles. Higher n value at peak aged condition of Al–Mg–Si alloy with excess Si content corresponded to cross-slipping and climbing of dislocations over large-size precipitates. In the case of our present work, it is likely that dislocations in the matrix of the as-cast specimen did not shear through the large-size eutectic Si particle. Instead, they were expected to accumulate and loop around each Si particle during plastic deformation. This resulted in the highest n value in the as-cast specimen. Regarding the aged specimen at 225 °C for 15 min, large-size precipitates possibly posed an obstacle to the movement of dislocations. The lower n value of the specimen aged at 165 °C for 18 h and at 195 °C for 3 h implied that coherent and smaller-size precipitates imposed an obstacle to dislocation gliding. By comparing between these two aging conditions, it is possible that the lower n value of the specimen aged at 195 °C for 3 h resulted from the lower precipitate density than that in the specimen aged at 165 °C for 18 h. The n value of 0.156 at the T6-peak-aged condition of this alloy was close to the n value of 0.166 at the T6-peak-aged of the cast A356 Al alloy reported in Ref. [17].

Regarding the precipitate kinetics of this alloy, the peak hardness time (t_{T6} in seconds) is related to the aging temperature (T in Kelvin) through an Arrhenius-type relationship, following the notation in Ref. [15]:

$$t_{T6} = C\exp\left(\frac{Q}{RT}\right) \tag{2}$$

where C is the pre-exponential factor, R is the universal gas constant = 8.314 J/mol K, and Q is the apparent activation energy in J/mol which is associated with the developed precipitates. Fig. 6 shows the Arrhenius-type plots for the alloy in this study and the experiment data points can be fitted with a straight line equation as follows:

$$t_{T6} = 3\times 10^{-11}\exp\left(\frac{128,717}{RT}\right) \tag{3}$$

The apparent activation energy Q for the precipitation process in the alloy calculated from the slope of the straight line is 128,717 J/mol. This value is very close to the activation energy of 130,000 J/mol in the aging of sand cast processed strontium-modified A356 Al alloy as determined by Rometsch and Schaffer [18]. Moreover, the high apparent activation energy of 163,000 J/mol had been reported for precipitation process in SSM-HPDC A356 Al alloy [15]. Lower activation energy of this alloy implied lower driving force for precipitation process resulting from the differences in the as-fabricated microstructure, alloying element contents, as well as the heat treatment condition. The activation energy of individual β″ precipitation in Al–0.8%Mg–1%Si alloy was only 94,400 J/mol as reported by Woo et al. [25] while higher activation energy for individual β′ precipitation in Al–1.12%Mg_2Si–0.35Si alloy was in the range of 116,600–126,600 J/mol as reported by Gaber et al. [26]. It can be noted that the activation energy for precipitation process in this study was evaluated from the peak aged time at the aging temperatures of 165 °C, 195 °C, and 225 °C. This value would then be represented as a combination of activation energies from different precipitation processes rather than individual precipitation process, and was close to the diffusion energy of Mg and Si in Al.

Therefore, the precipitation process in this alloy was controlled by the diffusion of Mg and Si in the Al matrix, which is in agreement with that reported by Gaber et al. [26]. By using Eq. (3), one could be able to predict the time to reach maximum hardness (t_{T6}) of the A356 Al alloy in this study.

4. Conclusions

The effects of artificial aging temperatures and times on the microstructures and the mechanical properties of semi-solid cast A356 Al alloy were studied. It can be concluded from this study that:

1. The optimum aging condition of the alloy after solution heat treatment at 540 °C for 4 h was 165 °C for 18 h at which the highest hardness of 96 HRE and the average tensile strength of 312 MPa with elongation of 7.6% were obtained at this condition. The tensile strength of the alloy in this study after aging at the optimum condition is comparable to that of some thixoformed products.
2. The peak aged specimen exhibited higher yield strength and ultimate tensile strength but slightly lower ductility than the aged specimens at 195 °C for 3 h and 225 °C for 15 min.
3. The strain hardening exponents of the specimen aged at 165 °C for 18 h and 195 °C for 3 h were lower than that of the as-cast specimen and specimen aged at 225 °C for 15 min.
4. Fine β″ needle-like precipitate was mainly responsible to peak aged strengthening of the alloy. The length of the needle-like precipitate elongated after aging at 195 °C for prolonged times. Thicker precipitate was found in the microstructure of the alloy aged at the higher temperature of 225 °C for 15 min.
5. The activation energy for the precipitation process of the alloy at the peak hardness time derived from this research was 128,717 J/mol.

Acknowledgments

The authors would like to thank the Prince of Songkla University for the 50% Ph.D. scholarship financial support, as well as the support from the Higher Education Research Promotion and National Research University Project of Thailand, Office of the Higher Education Commission and the Thailand Research Fund through the Royal Golden Jubilee Ph.D. Program (Grant No. PHD/0031/2552). In addition, we would like to thank the PSU Department of Mining and Materials Engineering for laboratory facilities.

References

[1] S. Thanabumrungkul, S. Janudom, R. Burapa, P. Dulyapraphant, J. Wannasin, Trans. Nonferrous Met. Soc. China 20 (2010) s1016–s1021.
[2] Z. Ma, A.M. Samuel, F.H. Samuel, H.W. Doty, S. Valtierra, Mater. Sci. Eng. A 490 (2008) 36–51.
[3] L.D. Lee, Mater. Sci. Eng. A 464 (2007) 249–254.
[4] A. Fadaviboostani, S. Tahamtan, Trans. Nonferrous Met. Soc. China 20 (2010) 1608–1614.
[5] D.B. Spencer, R. Mehrabian, M.C. Flemings, Met. Trans. 3 (1972) 1925–1932.
[6] D. Liu, H.V. Atkinson, P. Kapranos, W. Jirattiticharoean, H. Jones, Mater. Sci. Eng. A 361 (2003) 213–224.
[7] Z. Xiao-Li, L. Ting-Jua, X. Shui-Sheng, T. Hai-Tao, J. Jun-Ze, J. Mater. Process. Technol. 209 (2009) 2092–2098.
[8] R. Burapa, S. Janudom, T. Chucheep, R. Canyook, J. Wannasin, Trans. Nonferrous Met. Soc. China 20 (2010) s857–s861.
[9] H. Möller, G. Govender, W.E. Stumpf, Trans. Nonferrous Met. Soc. China 20 (2010) 1780–1785.
[10] Y. Birol, J. Alloys Compd. 484 (2009) 164–167.
[11] T. Rattanochaikul, S. Janudom, N. Memongkol, J. Wannasin, Trans. Nonferrous Met. Soc. China 20 (2010) 1763–1768.
[12] R. Canyook, S. Petsut, S. Wisutmethangoon, M.C. Flemings, J. Wannasin, Trans. Nonferrous Met. Soc. China 20 (2010) 1649–16551.
[13] E. Ogris, A. Wahlen, H. Luchinger, P.J. Uggowitzer, J. Light Met. 2 (2002) 263–269.
[14] H. Möller, G. Govender, W.E. Stumpf, R.D. Knutsen, Int. J. Cast Met. Res. 22 (6) (2009) 417–421.
[15] H. Möller, G. Govender, W.E. Stumpf, Open Mater. Sci. J. 2 (2008) 6–10.
[16] P. Cavaliere, E. Cerri, P. Leo, Mater. Charact. 55 (2005) 35–42.
[17] A.R. Emamia, S. Beguma, D.L. Chena, T. Skszek, X.P. Niu, Y. Zhang, F. Gabbianelli, Mater. Sci. Eng. A 516 (2009) 31–41.
[18] P.A. Rometsch, G.B. Schaffer, Mater. Sci. Eng. A 325 (2002) 424–434.
[19] A.K. Gupta, D.J. Lloyd, S.A. Court, Mater. Sci. Eng. A 316 (2001) 11–17.
[20] N. Chomsaeng, M. Haruta, T. Chairuangsri, H. Kurata, S. Isoda, M. Shiojiri, J. Alloys Compd. 496 (2010) 478–487.
[21] G.A. Edwards, K. Stiller, G.L. Dunlop, M.J. Couper, Acta Mater. 46 (11) (1998) 3893–3904.
[22] K. Matsuda, T. Naoi, K. Fujii, Y. Uetani, T. Sato, A. Kamio, S. Ikeno, Mater. Sci. Eng. A 262 (1999) 232–237.
[23] T.H. Courtney, Mechanical Behavior of Materials, MacGraw-Hill, New York, 1990, p. 14.
[24] L. Zhen, S.B. Kang, Metall. Mater. Trans. 28A (1997) 1489–1497.
[25] K.D. Woo, J.S. Lee, S.W. Kim, Met. Mater. 5 (4) (1999) 363–368.
[26] A. Gaber, M.A. Gaffar, M.S. Mostafa, E.F. Abo Zeid, J. Alloys Compd. 429 (2007) 167–175.

VITAE

Name Mrs.Narissara Mahathaninwong

Student ID 5110130021

Educational Attainment

Degree	Name of Institute	Year of Graduation
B.Sc. (Physics)	Prince of Songkla University	1999
M.Sc. (Nuclear Technology)	Chulalongkorn University	2002

Scholarship Awards during Enrolment

- 50% Ph. D. scholarship from Price of Songkla University
- The Thailand Research Fund through the Royal Golden Jubilee Ph.D. Program (Grant No. PHD/0031/2552).

Work – Position and Address

Lecturer at Faculty of Science and Industrial technology, Prince of Songkla University, Suratthani Campus, Maung, Suratthani 84000 THAILAND.

List of Publication and Proceedings

1. Narissara Mahathaninwong, Sirikul Wisutmethangoon,Thawatchai Plookphol, Jessada Wannasin, "Influence of Solution Heat Treatment on Microstructures of Semisolid Cast 7075 Aluminium Alloy", *Adv. Mater. Res.*, vol. 339, pp. 371-374, 2011.
2. N. Mahathaninwong, T. Plookphol, J. Wannasin, S. Wisutmethangoon, "T6 heat treatment of rheocasting 7075 Al alloy", *Mater. Sci. Eng. A*, vol. 532, pp. 91-99, 2012.

3. S. Wisutmethangoon, S. Thongjan, N. Mahathaninwong, T. Plookphol, J. Wannasin. “Precipitation Hardening of A356 Al Alloy produced by Gas Induced Semi-Solid Process”, *Mater. Sci. Eng. A*, vol. 532, pp. 610-615, 2012.
4. N. Mahathaninwong, Y. Zhou, S.E. Babcock, T. Plookphol, J. Wannasin, S. Wisutmethangoon, “Creep rupture behavior of semi-solid cast 7075-T6 Al alloy,” *Mater. Sci. Eng. A*,(be submitted, under revised process).